Temporal and spatial evolution of explosive silicic peralkaline eruptions at the Olkaria Volcanic Complex and Longonot volcano in the Southern Kenya Rift

P.A. Wallace, V. Otieno, P. Godec, R.W. Njoroge, M.S. Tubula, L. Cappelli, P.M. Kamau, S. Nomade, N.O. Mariita, K. Fontijn

Journal of Volcanology and Geothermal Research 460 (2025) 108275

Contents lists available at ScienceDirect

Journal of Volcanology and Geothermal Research

journal homepage: www.journals.elsevier.com/journal-of-volcanology-and-geothermal-research

Temporal and spatial evolution of explosive silicic peralkaline eruptions at the Olkaria Volcanic Complex and Longonot volcano in the Southern Kenya Rift

P.A. Wallace [a,b,*], V. Otieno [c], P. Godec [a], R.W. Njoroge [d], M.S. Tubula [c], L. Cappelli [a], P.M. Kamau [d], S. Nomade [e], N.O. Mariita [d], K. Fontijn [a]

[a] Université libre de Bruxelles (ULB), Department of Geosciences, Environment and Society, Avenue Franklin Roosevelt 50, 1050 Brussels, Belgium
[b] Ludwig-Maximilians-Universität München (LMU), Department of Earth and Environmental Sciences, Theresienstr. 41, Munich 80333, Germany
[c] Kenya Electricity Generating Company PLC (KenGen), Olkaria, Naivasha, Kenya
[d] Dedan Kimathi University of Technology (DeKUT), Geothermal Training and Research Institute, Nyeri, Kenya
[e] LSCE, UMR 8212, CEA, CNRS et Université de Versailles St-Quentin et Paris-Saclay, 91198 Gif-sur-Yvette Cedex, France

ARTICLE INFO

Keywords:
Explosive eruptions
Kenya Rift
Olkaria
Longonot
Tephrostratigraphy
Peralkaline

ABSTRACT

The Olkaria Volcanic Complex and adjacent Longonot volcano in the Southern Kenya Rift host major geothermal resources yet also pose volcanic hazards owing to their long histories of explosive eruptions. Olkaria is a multicentred dome complex consisting of lava domes, craters and fissures produced following the eruption of peralkaline comenditic rhyolites. Longonot is a trachytic caldera hosting a central summit crater, situated <10 km east of Olkaria, with pumice and ash eruptions being a dominant feature. This study reconstructs their evolution through detailed field, geochemical and geochronological investigations of widespread pyroclastic deposits. Logging sequences of pumice and ash fallout and pyroclastic density current deposits enables establishing a regional stratigraphic framework spanning the past 42 ka. Ten key eruptive units record explosive phases at Olkaria and Longonot, with eight $^{40}Ar/^{39}Ar$ ages and a radiocarbon date providing the first accurate age constraints of both volcanoes. The oldest explosive deposits identified in our field area are associated with the large-magnitude Maiella Pumice (MP) eruptions (338–333 ka), representing one of the first explosive silicic peralkaline eruptions in the Southern Kenya Rift. Within Olkaria, the earliest preserved deposits in our tephrostratigraphic framework are 42–37 ka pyroclastic density currents (OP) and pumice fallouts (OFB) representing early rhyolitic dome eruptions. Overlapping deposits reveal Longonot concurrently experienced repetitive large explosive eruptions emplacing pumice fall deposits from 37 ka to 17 ka (LAP). After 17 ka, LAP eruptions were punctuated by a single eruption of mixed basaltic trachyandesite, trachyandesite and trachyte pumice (LMx), followed by persistent trachyte ash venting at Longonot (LA1). Simultaneously, Olkaria transitioned to localised lava dome construction and collapse generating block-and-ash flows from 17 ka to 14 ka (OD1–2). Younger Longonot ash eruptions (LA2) and recent 191 ± 23 cal yr BP effusive–explosive activity at Olkaria's Ololbutot centre (OD3) reveals both volcanoes have remained active throughout the Holocene. Minimum estimated magnitudes for widespread fall units at both systems range between 4 and 5 (DRE deposit volumes of 0.04–0.35 km^3), representing substantial regional hazards, with eruption frequencies averaging up to one moderate–large eruption (magnitude 4–5) every ~2000 years for Longonot and one small–moderate explosive eruption (magnitude ~3) every ~200 years for Olkaria until ca. 10 ka, after which eruptions are significantly smaller and more localised. Statistical analysis of pumice glass geochemistry enables the fingerprinting of Olkaria deposits to likely source vents, tracking spatial-temporal variability across the complex. The larger explosive eruptions at both Olkaria and Longonot dispersed voluminous pyroclastic material (pumice and/or ash), which generated up to 1-m-thick deposits located ~20 km from its source vent in the case of Longonot, suggesting up to 200,000 people could be impacted from future similar magnitude eruptions, emphasising the necessity to combine eruptive history reconstructions with hazard analysis to advance preparedness and mitigation strategies.

* Corresponding author at: Ludwig-Maximilians-Universität München (LMU), Department of Earth and Environmental Sciences, Theresienstr. 41, Munich 80333, Germany
E-mail address: p.wallace@lmu.de (P.A. Wallace).

https://doi.org/10.1016/j.jvolgeores.2025.108275
Received 27 April 2024; Received in revised form 14 January 2025; Accepted 15 January 2025
Available online 20 January 2025

1. Introduction

The East African Rift System (EARS) is an active continental rift zone undergoing extension and volcanism due to the progressive break-up of the African plate (Ebinger, 2005; Ebinger et al., 2017; Fig. 1a). Peralkaline (molar $(Na_2O + K_2O)/Al_2O_3 > 1$) rhyolitic and trachytic explosive eruptions generating widespread tephra are a characteristic feature of rift evolution, recorded along the ~2000 km Eastern Branch (e.g., Hutchison et al., 2016; Wadge et al., 2016; Fontijn et al., 2018; Tadesse et al., 2022). Reconstructing the eruptive history of these highly explosive volcanoes is crucial for understanding rift development and assessing volcanic hazards. Tephrostratigraphy enables reconstructing eruption timing, magnitudes and dynamics by characterising and correlating pyroclastic deposits across a region (e.g., Fontijn et al., 2010, 2018; Martin-Jones et al., 2017). The EARS hosts ~78 Holocene active volcanoes, yet owing to the relatively longer repose intervals compared to subduction-related calc-alkaline systems (months–years vs. centuries–millennia), together with underreporting and lack of monitoring of volcanic activity at these systems, only 25% of these have a confirmed historical eruption (Wadge et al., 2016). Thus, our current records on EARS eruption characteristics and impacts are poor. As a result, assessing the wide range of potential eruptive styles and associated hazards at these volcanoes relies heavily on the geological record and characterising past eruption deposits. This is challenging as preservation

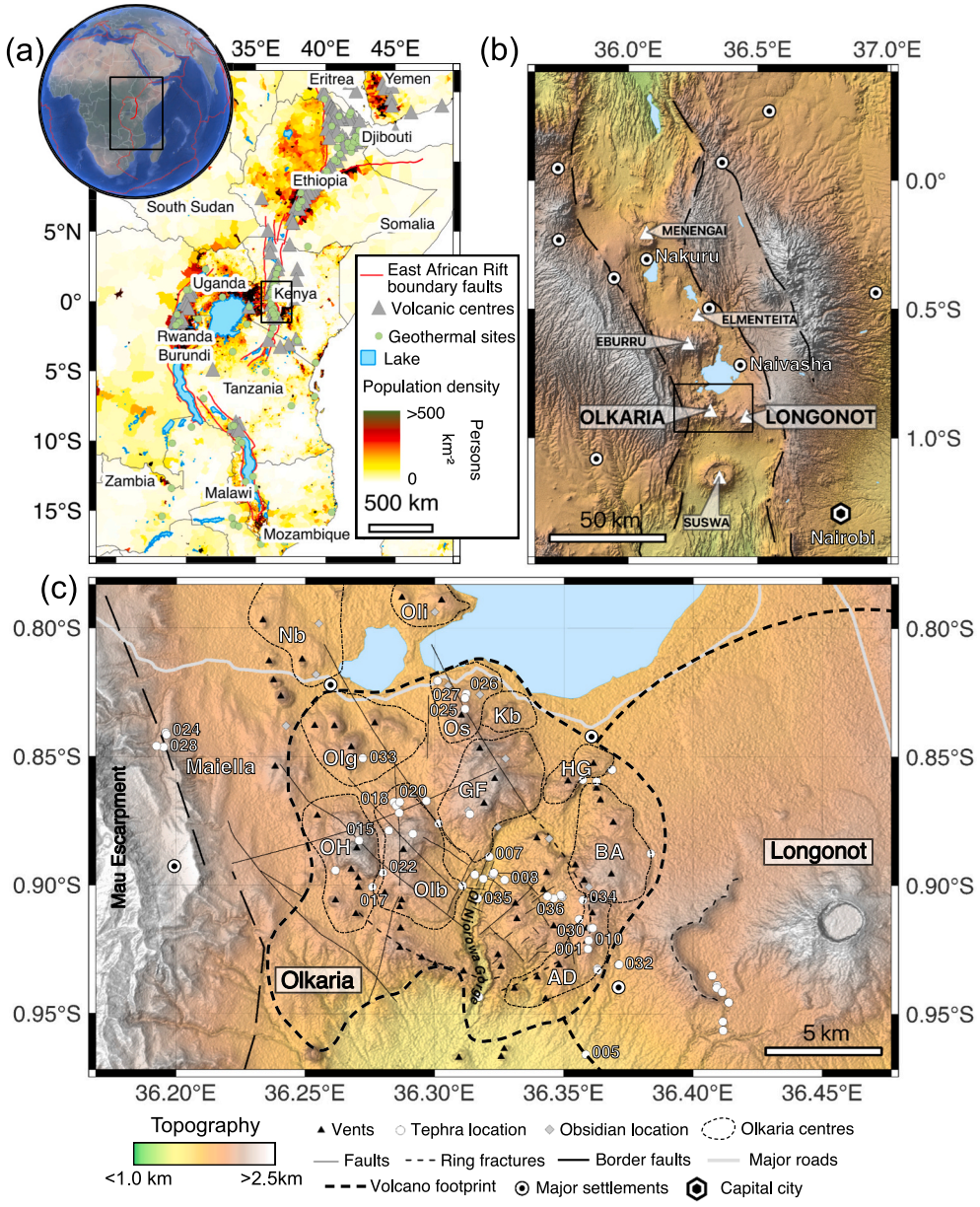

Fig. 1. Overview of the East African Rift System (EARS) and the Olkaria-Longonot region. (a) Map of East Africa displaying the extent of the EAR, major faulting, volcanoes, lakes, and geothermal potential sites. The overlaid heat map represents the 2020 population density data provided by the Socioeconomic Data and Applications Centre (SEDAC). (b) Topographic map of the Central-Southern Kenya Rift highlighting active volcanic centres and the study area encompassing Olkaria and Longonot. (c) Combined topographic and digital elevation model map of the Olkaria Volcanic Complex and Longonot region, revealing the distribution of mapped faults, individual vents at Olkaria, and sample locations for tephra and lavas. Thin dashed lines in (c) delineate previously identified eruptive centres within Olkaria (Marshall et al., 2009): Olkaria Hill (OH), Ololbutot (Olb), Oserian (Os), Broad Acres (BA), Arcuate Domes (AD), Kibikoni (Kb), Hell's Gate (HG), Gorge Farm (GF), Olenguruoni (Olg), Ndabibi (Nb), and Ololerai (Oli). Volcano footprints in (c) represent the extent of lava flows from the Olkaria and Longonot centres (modified from Heumann and Davies, 2002).

of tephra sequences is often limited, but critical as these systems can remain dormant for hundreds to thousands of years between eruptions (Fontijn et al., 2010, 2018; McNamara et al., 2018; Tadesse et al., 2022), hampering disaster preparedness (Biggs et al., 2009, 2021; Clarke et al., 2020; Tierz et al., 2020).

Large explosive silicic eruptions pose high risk to rift valley settlements and infrastructure, evidenced by their capacity to dramatically shape landscapes across East Africa (Mohr et al., 1980; Leat, 1984). Signs of renewed unrest at several Quaternary volcanoes based on satellite remote sensing and seismic data underscore the active nature of the volcanic systems (Biggs et al., 2009, 2011; Albino and Biggs, 2021; Albino et al., 2022). The lower viscosity of peralkaline magmas relative to calc-alkaline counterparts, along with the high volatile contents of EARS magmas impart an exceptional mobility and outgassing potential contributing to a range of eruption styles (Di Genova et al., 2013; Iddon and Edmonds, 2020). At Nyiragongo, 1977 and 2002 lava flows reached speeds up to 100 km/h during flank eruptions, directly threatening Goma city (Tazieff, 1977; Komorowski and Karume, 2015), with lava flows during the 2021 crisis continuing to pose significant hazards (e.g., Boudoire et al., 2022). The largest historical eruption in the EARS was Dubbi in 1861, generating over 3 km^3 of trachyandesite lava flows and dispersing ash across 400 km, resulting in over 100 fatalities in this remote region (Wiart and Oppenheimer, 2000). More recently in 2011, Nabro volcano produced an eruption plume reaching the lower stratosphere, emitting ~4.5 Tg SO_2 and blanketing the region in tephra (Theys et al., 2013; Goitom et al., 2015). These events provide examples of the hazards posed by EARS volcanism, but a wide spectrum of eruption styles exist along the rift. Large explosive peralkaline rhyolite–trachyte eruptions can also occur, as evidenced by widespread pumice deposits (e.g., Blegen et al., 2016). However, such explosive pumice eruptions has never been observed leaving many uncertainties over the potential future hazards they may pose (Sparks et al., 2011).

The Southern Kenya Rift (SKR) records extensive Quaternary silicic volcanism focused along the rift axis, termed the Central Kenya Peralkaline Province (Fig. 1b; Macdonald and Scaillet, 2006). Peralkaline trachyte and rhyolite central vent complexes like Menengai, Longonot and Suswa host calderas up to 10 km across formed during major eruptions in the Late Pleistocene (Leat, 1984; Clarke et al., 1990; Macdonald et al., 2008). It has been hypothesized that regional tectonic stress changes may be a factor in controlling such eruptive activity owing to rift floor tension fractures and normal faults acting as lateral magma pathways and conduits, respectively (e.g., synchronous caldera-forming eruptions at Longonot and Suswa; Scott and Skilling, 1999). Post-caldera volcanism is evidenced by youthful lava domes and cones formed within the collapse craters during the Holocene (Scott, 1980; Clarke et al., 1990; Macdonald et al., 2008). Despite this long eruptive history, detailed studies characterising the timing, products and processes of explosive volcanism in the SKR significantly lag behind those focused in the Main Ethiopian Rift (MER) over the past decade (Hutchison et al., 2016; Fontijn et al., 2018; Tadesse et al., 2022). Furthermore, despite several SKR volcanoes recording signs of deformation (Biggs et al., 2009; Albino and Biggs, 2021) and CO_2 degassing (Robertson et al., 2016; Cappelli et al., 2023) indicative of active magmatic processes, the eruptive behaviours and associated hazards remain poorly characterised. There is substantial need to improve understanding of their past eruptive histories as well as subsurface architecture influencing renewals of activity. In particular, two neighbouring peralkaline volcanic systems in the SKR, the Olkaria Volcanic Complex (hereaf termed Olkaria) and Longonot, are examples of systems likely to display renewed activity in the near future (Fig. 1c; Scott, 1980; Clarke et al., 1990; Biggs et al., 2009; Macdonald et al., 2022). The thick successions of tephra deposits surrounding both centres indicate that explosive eruptions played a significant role in their past activity and may feature prominently in potential future eruptions (Clarke et al., 1990; Macdonald et al., 2008). This, coupled with ongoing geothermal exploration in the area, underscores the critical importance of comprehending their past eruptive patterns. While both Olkaria's and Longonot's eruptive products have been investigated (Scott, 1980; Clarke et al., 1990; Macdonald et al., 2008; Marshall et al., 2009), these studies have primarily focused on the lavas, and details on the style, timing, magnitude and evolution of explosive phases are limited and thus poorly constrained (Scott, 1980; Clarke et al., 1990).

This study aims to develop a detailed eruptive history of explosive volcanism at Olkaria and adjacent Longonot volcano through tephrostratigraphic reconstructions. Characterising pyroclastic deposits using field observations, deposit descriptions, pumice compositions and geochronology provide better constraints on eruption timing, magnitudes and vent locations (e.g., Fontijn et al., 2010, 2018; Tadesse et al., 2022). A particular emphasis is placed on logging sequences of pumice fall, ash and pyroclastic density current (PDC) units across multiple sites to establish a stratigraphic framework. New $^{40}Ar/^{39}Ar$ dating of key units improves age estimates on volcanic activity at Olkaria and Longonot, which previously had large uncertainties. Furthermore, identifying unique chemical fingerprints of different pumice deposits enables correlations to specific source vents across the volcanic complex. The results provide an important baseline on explosive eruptive behaviour at Olkaria to inform hazard analysis and volcanic monitoring efforts in light of possible future activity amidst rising unrest signals (e.g., Tierz et al., 2020).

2. Geological setting

2.1. Kenya Rift

The Kenya Rift is an active volcano-tectonic segment of the EARS, extending nearly 1000 km from northern Tanzania to the Turkana basin (Fig. 1b; Smith and Mosley, 1993; Macdonald et al., 1994; Smith, 1994; Heumann and Davies, 2002). It has been active since the Oligocene, with the focus of magmatism and extension migrating southward over time (Macdonald et al., 2001). The rift narrows from a ~150-km-wide extensional zone in the north (south of the Broadly Rifted Zone) to only ~50 km wide at its southern terminus. Here, it transitions into a widely distributed zone of faulting and diffuse extension on the north-eastern edge of the Tanzanian Craton known as the North Tanzanian Divergence Zone (Ebinger et al., 2000). The Kenya Rift is bounded by NE–SW border faults separating the rift floor from the adjacent Eastern and Western Plateaux (Keranen et al., 2004; Muirhead et al., 2016; Ebinger et al., 2017), and cuts across major lithospheric boundaries, transitioning from the late Proterozoic Mozambique mobile belt in the north to the Archaean Tanzanian craton and its remobilised margins in the south (Smith and Mosley, 1993; Rogers et al., 2006). These blocks were juxtaposed and modified by continental-scale shear zones (i.e., Aswa shear zone) subsequently reactivated by rifting, influencing strain accommodation and exerting control on the location of graben structures and magma accumulation in the Miocene (Smith and Mosley, 1993; Macdonald et al., 2001). A common mantle plume source, likely the deeply rooted African Superplume originating at the core-mantle boundary, is believed to influence magmatism throughout the entire EARS (Halldórsson et al., 2014). However, in southern Kenya, noble gas isotopes reveal a strong subcontinental lithospheric mantle signal and less plume involvement, albeit there is wide variability in isotopic signatures for these magmas (Rooney, 2020 and references therein).

The focus of Quaternary–Recent volcanism has localised along axial magmatic zones, where volcanic productivity peaked in the Late Pleistocene–Holocene from major central silicic complexes like Menengai, Longonot, Suswa and Olkaria (Clarke et al., 1990; Scott and Skilling, 1999; Macdonald, 2002; Mibei et al., 2021). The silicic complexes of Olkaria, Eburru and Longonot lie at the apex of an area of lithospheric doming, termed the Kenya Dome (Macdonald et al., 1994; Smith, 1994). Their mildly peralkaline rhyolites (comendites and pantellerites) and phonolites overlie mafic rift basalts and thus likely originate via crustal anatexis of buried Precambrian rocks or differentiation of mantle melts

(Scott and Skilling, 1999).

2.2. Olkaria Volcanic Complex

The Olkaria Volcanic Complex, previously termed Naivasha complex (Macdonald et al., 1987), is a predominantly comenditic (rhyolite) volcanic system that lies near the centre of the Kenya Dome in the axis of the SKR (Davies and Macdonald, 1987; Macdonald et al., 1987; Clarke et al., 1990). The complex sits immediately south and southeast of Lake Naivasha, <10 km from the western rift escarpment (Mau Escarpment), and at the intersection where the rift changes orientation from NNW–SSE to NNE–SSW likely accommodating a pre-rift structure (Muirhead and Kattenhorn, 2018). It is surrounded by three other, compositionally distinguishable major volcanic centres, the pantelleritic-trachytic Eburru complex ~40 km to the north, the phonolitic-trachytic Suswa caldera ~40 km to the south, and the trachytic caldera of Longonot <10 km to the east (Fig. 1b-c; Macdonald et al., 1987; Clarke et al., 1990).

Olkaria comprises a volcanic dome and lava field spanning ~240 km^2 with over 80 vents identified (Fig. 1c), mostly as small eruptive centres in the form of lava domes, pumice cones, fissures and craters. The centres occur predominantly as steep-sided domes with extensive pyroclastic deposits or short, laterally restricted thick lava flows (Clarke et al., 1990). The domes represent distinct topographic features of the complex, ranging in size from ~500 m wide and ~50 m high to ~2 km wide and 340 m high, and together with the flows are used to define different centres that make up the complex as shown in Fig. 1c (e.g., Gorge Farm, Olkaria Hill, Olenguruoni Hills; Davies and Macdonald, 1987; Macdonald et al., 1987; Clarke et al., 1990; Wilding et al., 1993; Black et al., 1997). Extensive N–S normal regional faulting characterise this section of the rift, in addition to more local structures within Olkaria displaying E–W and NE–SW trending normal faults evidenced by possible dome alignment (Omenda, 1998; Simiyu and Keller, 2000; Axelsson et al., 2017; Omollo et al., 2022). One notable example of dome alignment is the arcuate ring structure at the southern and eastern margin of the complex (first described by Naylor, 1972), which has subsequently been related to a caldera collapse (Clarke et al., 1990).

The regional lithostratigraphic succession has been defined based on cores obtained from geothermal wells and includes a Proterozoic basement, Pre-Mau Volcanics, Mau Tuffs, Plateau Trachytes, Olkaria Basalt and Olkaria volcanics composed of comenditic lavas and pyroclastics (Clarke et al., 1990; Omenda, 1998). The initiation of volcanism within the Olkaria region is very poorly constrained, but eruptive activity is thought to extend back to ~450 ka based on an unpublished date obtained from one of these boreholes (BC King, pers. comm. in Clarke et al., 1990). At the surface, the eruptive products are overwhelmingly mildly peralkaline rhyolites (comendites), along with volumetrically minor hawaiites, mugearites, benmoreites, trachytes and basalts observed at the margins of the complex and occasionally co-mingled with the comendites, highlighting the diversity of rock types and complexity of the magmatic plumbing system.

Olkaria comendites are silica-oversaturated with a moderate peralkalinity molar index ($(Na_2O + K_2O)/Al_2O_3$) of 1.0–1.5 (Macdonald et al., 1987; Marshall et al., 2009). Based on detailed trace element and isotopic compositions of the comenditic lavas (Macdonald et al., 1987; Davies and Macdonald, 1987), combined with the lava's proximity to an eruptive vent and any nearby topographic features, Marshall et al. (2009) subdivided Olkaria into 13 spatially defined centres (Fig. 1c; Marshall et al., 2009). The comendites are interpreted to be formed by both advanced fractional crystallisation of the trachytes (formed by separate fractional crystallisation of a basaltic parent) and by small degrees of partial melting of syenitic rocks, subsequently residing within several small, shallow, independent, volatile-rich (<3.4 wt% H_2O, <0.95 wt% F and < 0.47 wt% Cl; Macdonald et al., 1987; Wilding et al., 1993) reservoirs (Davies and Macdonald, 1987; Macdonald et al., 1987, 2008). Each of the 13 centres record a different evolutionary history with changes in chemistry and degree of evolution, and the longevity of the system is suggested to be maintained by heat and material input from underlying mafic magmas (Marshall et al., 2009).

Based on an early field-based volcanological survey involving mapping of the different surface lithologies (Clarke et al., 1990), a general model was proposed for the eruptive history of Olkaria. This model suggested, although with large uncertainty, the earliest rhyolitic eruptions of Olkaria took place at ~20 ka, and were marked by the formation of a welded pantelleritic ignimbrite only observed at the base of the Ol Njorowa gorge (O1); the formation of a 11 km by 7.5 km caldera was interpreted based on the curved alignment of ring fracture domes in the south and east of the complex. However, the presence of a caldera structure is still debated (e.g., Heumann and Davies, 2002). Concurrently, widespread pumice deposits exposed outside the complex to the NW and SW were observed along with minor volumes of basalt (Lolonito basalt) and trachyte (Olkaria trachyte, Ot). These widespread pumice deposits, termed Maiella Pumice (Mp), are poorly explored with their source unknown, but were believed to come from a vent within Olkaria (Clarke et al., 1990). Post-caldera activity is represented by a predominant dome-building phase and the first appearance of the comendites, divided into the Lower (O2), Middle (O3) and Upper (O4) Comendite Members. The Lower Comendites (~20 ka) are characterised by the formation of lava domes and pyroclastic deposits, the Middle Comendites (~8 ka) are associated with domes forming along the ring fracture and extensive PDC deposits, and the Upper Comendites (~6 ka) represent thick, short lava flows located at the entrance to Hell's Gate in the NE of the complex attributed to caldera resurgence. Until this study, no dates have been obtained directly for Olkaria deposits, and these current age constraints come indirectly from ^{14}C dates of palaeosol horizons from Longonot to provide an approximate age bracket for the Olkaria comendites (Table 2). The most recent eruptive activity (O5) has been associated with a high-silica comendite obsidian flow emerging from the southern tip of a N–S trending fissure within the Ololbutot centre (Macdonald et al., 1987; Clarke et al., 1990; Marshall et al., 1998), dated at ~180 ± 50 years BP using charcoal found within an associated pumice flow deposit (Clarke et al., 1990). Despite the poor age constraints, it has been generally accepted that most peralkaline rhyolitic activity took place within the last 20 kyrs. Subsequent work on isotope disequilibria (Rb–Sr and U–Th) have provided constraints on the timescales of magmatic processes, suggesting that isochron ages are consistently older than the estimated eruption age (e.g., 22.4 ka for a ~ 8 ka Gorge Farm eruption) leading to the interpretation that the magmas were stored for a long duration with limited mixing prior to eruption (Heumann and Davies, 2002). Additionally, besides the preliminary mapping of Olkaria's pyroclastic deposits (Clarke et al., 1990), subsequent work on Olkaria has focused exclusively on the lava flows (Macdonald et al., 2008; Marshall et al., 2009).

Olkaria has been recognised as a potential site for geothermal exploration since the 1950s, with first extraction taking place in 1981. Today, it stands as the largest geothermal energy producer in Africa with an estimated production capacity of ~952 MWe from six conventional power plants and 15 wellhead generators. The geothermal system (~204 km^2) is classified as a high-temperature, liquid-dominated system, with temperatures ranging from 260°C to over 350°C at depths of up to 3 km. The high productivity of the system is attributed to the traversing fault lineaments through the complex that make ideal pathways for both meteoric and magmatic fluids, particularly with the increased permeability at fault intersections (Omenda, 1998; Lagat, 2003; Otieno, 2016; Omollo et al., 2022). Soil CO_2 emission surveys across the complex support the structural control on circulating hydrothermal fluids and isotopically confirm its deep-seated magmatic origin (Cappelli et al., 2023). Magnetotelluric (Omollo et al., 2022) and gravitational (Omollo and Nishijima, 2023) surveys, along with microseismicity hypocenter locations (Shi et al., 2021), have revealed at least three separate magmatic intrusions beneath Olkaria at ~5.5–8 km depth, likely fed by a deeper magma reservoir, acting as the heat source

for the circulating hydrothermal fluids (Omenda, 1998). Observations from satellite remote sensing data (InSAR) have revealed that the central portion of Olkaria has been in a state of deflation between 2015 and 2020 at 2.5 ± 0.5 cm/yr (Albino and Biggs, 2021). Despite exploitation-induced depletion of hydrothermal fluids and subsequent pore-pressure changes being inferred as the cause of this deformation (Albino and Biggs, 2021), changes in the deeper magmatic reservoir cannot be ruled out.

2.3. Longonot volcano

Longonot volcano is a predominantly peralkaline trachyte system located <10 km east of Olkaria (Fig. 1c) and ~10 km from the eastern rift margin (Kinangop Escarpment). In contrast to Olkaria's surface morphology, Longonot consists of a single summit crater sitting within a well-defined caldera depression (~7.5 km in diameter) that formed after the collapse of large shield volcano (Scott, 1980; Clarke et al., 1990; Robertson et al., 2016). Today, the caldera margins can be seen as a steep-sided arcuate ridge up to 300 m high on the northern, western and southern edges of the central edifice (Fig. 1c).

Field-based mapping and descriptions of eruptive products by Scott (1980) revealed Longonot is predominantly composed of peralkaline (comenditic–pantelleritic) trachytic pyroclastic deposits and lava flows (Scott, 1980; Clarke et al., 1990), along with minor volumes of mixed hawaiite–trachyte lavas (Scott, 1980). Initiation of volcanism at Longonot is estimated at ~400 ka based on a date obtained for the termination of major plateau faulting (Baker and Mitchell, 1976; Scott, 1980; Clarke et al., 1990). Two major collapse events have been identified, the first formed an embayed, 7.5 km caldera at the summit of an early composite volcano, while the second formed a circular pit crater 1.8 km across at the summit of a later lava pile. The eruptive history of Longonot spans from (1) the growth of the early trachytic composite volcano (Lt1), (2) caldera collapse represented by the Kedong Valley Tuff (Lp1 and Lp3), (3) eruption of thick pumice beds that formed a central pyroclastic cone (Akira Pumice Formation, Lp2, Lp4, Lp5 and Lp7; <9.1 ± 0.1 ka) with later stages involving bedded ashfalls (Lp6) and extrusion of trachyte (Lt2) and mixed hawaiite–trachyte lavas (Lmx; Scott and Bailey, 1984), (4) pit crater collapse associated with deposition of thick ash sequences (Longonot Ash Formation, Lp8; <3.5 ± 0.1 ka), and (5) final small flank and crater eruptions (Scott, 1980; Clarke et al., 1990). The most recent activity at Longonot is a trachytic lava flow (Lt3) from a northern flank fissure, dated at 1863 ± 5 CE based on Maasai tradition descriptions (date also reported in Robertson et al., 2016). Similarly to Olkaria, the age constraints on the timing of the different eruptive stages at Longonot are poor and limited to ^{14}C dates of palaeosol horizons. The style of caldera collapse is often compared to other nearby caldera volcanoes such as Menengai and Suswa, revealing some similarities in their eruptive histories. In particular, synchronous initiation of caldera formation at Longonot and Suswa has been proposed based on tephrochronology and geochemical fingerprinting, emphasising the importance of regional tectonic controls on magma migration and volcanism (Scott and Skilling, 1999). Attempts to improve constraints on the rates and timescales of magmatism at Longonot have come from U–Th–Ra disequilibria which provide rates of fractionation, indicating a storage time between 1–2 kyrs before eruption, as well as eruption of magmas simultaneously undergoing fractionation (Rogers et al., 2004).

Longonot has been a prospective geothermal site since 1998, hosting a geothermal reservoir with a potential production capacity of >200 MWe (Simiyu, 2008; Omenda, 2010; Alexander and Ussher, 2011). Magnetotelluric surveys by Alexander and Ussher (2011) indicate geothermal reservoir temperatures exceeding 200°C may occur at 550–800 m depth across the area owing to the cooling of multiple intrusive magma bodies, resulting in a hydrological conceptual model that suggests the presence of a high temperature (250–300°C) hydrothermal reservoir sufficient for geothermal power generation. An episode of uplift of 9.2 cm was detected between 2004 and 2006, coinciding with perturbations in hydrothermal activity, attributed to the recharge of the magma reservoir at ~4 km depth (Biggs et al., 2009). These intrusions, inferred to reside beneath the caldera, are interpreted as the heat source driving hydrothermal fluid convection in the system. CO_2 degassing surveys across Longonot also highlight a magmatic signature and the volcano-tectonic control on fluid pathways, with surface manifestations aligning with the NNW–SSE structural trend of the region (Robertson et al., 2016). Despite the identified geothermal potential, the development of the geothermal resource at Longonot has been slow, but ongoing exploration is expected to continue as Kenya continues to develop its renewable energy resources (Alexander and Ussher, 2011).

3. Methods

Two field campaigns were carried out in November 2020 and July 2021 to characterise and sample pyroclastic deposits around Olkaria, south of Lake Naivasha (Fig. 1c). A total of 36 outcrops were systematically logged, and a total of 298 samples were collected from different stratigraphic units (see supplementary material (SM-1) for all sample locations). Pyroclastic units were correlated across the volcanic complex using a combination of field observations, physical characteristics of the tephra (e.g., componentry) and pumice glass compositions. Some deposits were easily distinguishable from each other based on macroscopic field observations (e.g., pumice colour, lithic content). Deposits that displayed similar characteristics and were stratigraphically correlatable were grouped into broad units.

Component analysis (componentry) was performed on 142 samples to quantify the proportions of different particle types within the tephra deposits. Samples up to 2 kg were dry-sieved at 1φ intervals between -4φ (16 mm) and 4φ (0.063 mm). For each sample, the 0.5–1 mm grain size fraction was selected for componentry as it represented a comparable size fraction for all deposits. At least 200 grains were qualitatively assigned to one of ten classes and counted: (1) light-grey pumice, (2) dark-grey pumice, (3) tube pumice, (4) vesicular obsidian, (5) dense obsidian, (6) felsic crystals, (7) mafic crystals, (8) lithic lavas, (9) hydrothermally altered, and (10) holocrystalline. See supplementary material (SM-2) for full dataset.

A total of 82 samples, including nine from the Maiella Pumice, were selected for glass major element analysis. Three to four pumice lapilli from each sample were manually crushed using an agate pestle and mortar. The crushed samples were wet-sieved at 80 μm, dried at 50°C, and cold-mounted in pre-drilled EpoFix resin discs. The recovered fresh shards were polished with SiC paper (P1200 and P2400 grit) and diamond paste (3 μm and 1 μm). Major element concentrations were determined by electron probe microanalysis (EPMA) using a CAMECA SX-100 at the Laboratoire Magmas et Volcans, Clermont-Ferrand (France). Analyses were conducted with a 15 kV accelerating voltage, using a 10 μm defocused beam and a 4 nA current. For samples with smaller glass areas, a 5 μm beam diameter and 2 nA current were used. Peak count times were 30 s (Fe, Mg, Cl), 20 s (Al, Ti) and 10 s (Si, Mn, Ca, Na, K, P), with background count times set to half the peak times. To limit alkali migration during measurements, Na and K were always analysed first. It should be noted that if pumice glasses have a high water content it can facilitate alkali migration further during EPMA, consequently causing a slight underestimation in alkalis and overestimation in silica. The presence of high water content in pumice glasses is inferred from the low analytical EPMA totals (typically <97 wt%), a common indicator of dissolved water in volcanic glasses, and the presence of abundant vesicles in the pumice texture. The spectrometers were calibrated with appropriate mineral standards. Secondary glass standards (ATHO-G, StHs6/80-G, and MLB-3-G; Jochum et al., 2006) were analysed regularly to verify calibration accuracy, which was typically <2% for most major elements, except Mn (± 30%) and P (± 6%). At least 20 points were analysed per sample, and only analyses with totals above 92 wt% were considered reliable, which were subsequently normalised to

100% (volatile-free basis) before interpreting and plotting (e.g., Froggatt, 1983; Lowe, 2011). The quality control of 92 wt% total cut-off was used in order to take into account the potentially high magmatic water contents of the natural pumice glasses, any post-depositional hydration and/or alteration, and to remain consistent with the cut-off values for previous studies on pyroclastic materials to enable valid comparisons (e.g., Tadesse et al., 2022). For more details on the EPMA data, analytical conditions and the secondary standards, see the supplementary material (SM-3).

Eight pumice samples were selected for $^{40}Ar/^{39}Ar$ dating at the Laboratoire des Sciences du Climat et de l'Environnement (CEA, UMR 8212 CNRS-LSCE; Gif Sur Yvette, France). The samples were crushed, sieved, and the 0.5–1 mm fraction was chosen for analysis due to its high abundance of inclusion-free K-feldspar crystals. The crystals were hand-picked, leached in HF acid to remove groundmass and rinsed in an ultrasonic bath. At least 30 crystals per sample were irradiated in the Oregon State University TRIGA reactor. After irradiation, the crystals were fused using a CO_2 laser and the extracted gases were purified using SAES GP-50 getters. Argon isotopes were measured on a ISOTOPX NGX 600 mass spectrometer. Data reduction was performed using ArArCALC V2.4 (Koppers, 2002), and the neutron fluence J factor was calculated using co-irradiated Alder Creek sanidine standard ACs-2 (Niespolo et al., 2017) according to the K total decay constant of Renne et al. (2011). To ensure detector linearity, mass discrimination was monitored daily by analysing air shots of various beam sizes (Lee et al., 2006). Procedural blank measurements were performed after every three unknowns. Full methodology description and analytical data are provided in the supplementary material (SM-5). The results of all $^{40}Ar/^{39}Ar$ dating of individual pumice deposits are presented as probability diagrams (Fig. S1 in SM-5). Weighted mean age uncertainties are all reported at 2σ, including J uncertainty and were calculated using Isoplot 4.1 (Ludwig, 2003). Xenocrystic crystal populations were detected using the inverse isochron method, which allowed the assessment of any non-radiogenic ^{40}Ar (excess argon) being incorporated into the feldspar crystal resulting in an older age. Any crystals, within uncertainty, with an $^{40}Ar/^{36}Ar$ initial intercept higher than atmospheric (i.e., 298.56) were considered xenocrystic and removed from the dataset in order to achieve an age only for the juvenile crystal population (i.e., the age of the eruption).

Three samples of charcoal embedded at the base of a tephra deposit located east of the most recent Ololbutot flow within the Ol Njorowa gorge were sampled for accelerator mass spectrometry (AMS) radiocarbon dating. Sample preparation and analysis was performed at the Koninklijk Instituut voor het Kunstpatrimonium - Institut Royal du Patrimoine Artistique (KIK-IRPA) in Belgium. The charcoal sample was first cleaned and dried to remove any impurities or contaminants that could affect the ^{14}C dating results. The sample was crushed into a fine powder and homogenised to ensure that it is representative of the entire sample. The carbon in the charcoal sample was converted to carbon dioxide gas using a combustion reaction. The carbon dioxide gas was then purified using a series of chemical and physical processes to remove any impurities or contaminants. The purified carbon dioxide gas was compressed and stored in a sample container for further analysis. The ^{14}C content of the purified carbon dioxide gas was measured using an AMS. The AMS measures the ratio of ^{14}C to ^{12}C in the sample, which is proportional to the age of the sample. The conventional age obtained from the AMS measurement was calibrated using the program Oxcal 4.4 (Bronk Ramsey, 2009) using the SHCal20 calibration curve (Hogg et al., 2020) providing a calibrated age with a 95.4% probability interval.

As Olkaria consists of multiple single vents, a principal component analysis (PCA) and k-means clustering was performed to identify the vent sourced for each tephra deposit. The major element compositions of pumice glass from tephra deposits analysed by EPMA were first compiled with existing geochemical data on obsidian lava flows from known vents in the study area. Prior to statistical analysis, the major element oxide data were normalised to 100%. PCA was performed using the JMP Pro© Statistical Discovery software in order to identify the key elemental variables controlling compositional variations. The scores for the first three principal components (PCs) explaining the majority of the total variance were retained for analysis. K-means clustering was applied to cluster the geochemical data into distinct groups. In order to determine the optimal number of clusters for the data input, we applied the cubic cluster criterion (CCC) method which provides a quantitative metric to assess different numbers of clusters (k). For each k value chosen, it measures the within cluster homogeneity versus between cluster separation to evaluate cluster quality. The optimal k value (i.e., number of clusters) is indicated by a peak in the CCC plot, where increasing k no longer yields substantial improvement in clustering quality. Once k was determined, cluster assignments were visualised using PC1–3. The glass compositions of tephra samples were compared to lava flow compositions assigned to each cluster. This allowed correlating the geochemical signature of the tephra deposits to known vents that have matching compositions. The clustering results constrained potential source vents for each of the studied tephra deposits. All details on PCA and k-means clustering can be found in the supplementary material (SM-4).

Tephra deposit volumes were calculated for three major eruptions using the exponential thinning technique of Pyle (1989). Isopach maps were constructed by plotting between 5 and 8 data points and contouring the logged thicknesses from each outcrop. Thickness measurements were interpolated between data points to create isopachs at regular intervals. The resulting isopach map was digitised and each contour was assigned an area. The thickness at each isopach was multiplied by its enclosed area to calculate a volume. Minimum volumes for the deposits were calculated by integrating thickness decay as an exponential function for an elliptical isopach geometry:

$$V = 13.08 T_0 b_t^2 / a.$$

where T is the maximum thickness at distance 0, b_t is the thickness half-distance and a is the eccentricity of the elliptical isopach. b_t was defined as the distance along the minor axis of the isopach ellipse over which the deposit thickness decreased by half its value. The minimum magnitude for each eruption was calculated using the empirical relationship with eruptive mass from Pyle (2015):

$$M = log10\,[\text{eruptive mass, kg}] - 7.$$

where M is magnitude and eruptive mass calculated on a dense rock equivalent (DRE) basis using an appropriate melt density.

4. Results

4.1. Tephrostratigraphy and geochronology

We identify 10 individual volcanic units that are interpreted as the products of separate explosive phases from different vents across Olkaria and Longonot. The deposits are distinguished based on lithological characteristics such as componentry, clast textures and glass geochemistry, as well as depositional features (e.g., sorting, pumice sizes). Intercalated Olkaria (rhyolitic) and Longonot (trachytic) deposits were easily distinguishable from each other in the field based on pumice colour, Olkaria pumice being white–light grey and Longonot being dark grey. The units are correlated at a local to sub-regional scale based on field and laboratory data. In the following descriptions, the deposits are categorised into the 10 units that could be correlated across the field area and are described from oldest to youngest. Based on deposit field characteristics, units are defined as being deposited at very proximal (<5 km), proximal (5–10 km) or medial (10–30 km) distances from a source vent.

The tephrostratigraphic framework for Olkaria and Longonot deposits is shown in Fig. 2a-d, with representative field photos in Fig. 3, Fig. 4, Fig. 5 and Fig. 6. A synoptic overview of the stratigraphic units is given in Table 1, and $^{40}Ar/^{39}Ar$ and ^{14}C ages for each unit are shown in

Table 2, all summarised below in chronological order (Fig. 2d). The Maiella Pumice (MP) is a series of regional pumice fall beds marking one of the earliest explosive phases of volcanic activity in the SKR. The oldest deposits found within Olkaria are the Olkaria PDCs (OP), a massive series of PDC deposits exposed within a side river valley of the main Ol Njorowa gorge. Overlying this are a series of Olkaria pumice fall breccia deposits (OFB) distinguished by variations in thickness, grading and lithic content. The later deposits of this unit intercalate and are superimposed by the Longonot-sourced Akira pumice falls (LAP), recognised by the presence of well-sorted, dark grey, unwelded pumice clasts. A chemically mixed pumice unit (LMx) from Longonot marks the transition back to Olkaria eruptive activity (OD1) with repetitive medial fall deposits, followed by a series of alternating ash and lapilli beds from Longonot (LA1). A thick sequence of block-and-ash flow deposits (OD2) displaying crude bedding and lithic-rich horizons represent localised dome activity within Olkaria. The uppermost units include further Longonot ash deposits (LA2) with renewed block-and-ash flow and PDC activity (OD3) associated with the active Ololbutot centre.

4.1.1. Maiella Pumice (MP – ca. 338–333 ka)

The Maiella Pumice is the oldest pyroclastic deposit recorded in our study of the SKR region, consisting of a series of widespread pyroclastic fall deposits only exposed to the west of Olkaria towards the rift shoulder of the Mau Escarpment (Fig. 2b). These deposits were previously mapped across a significant portion of southern Kenya (Clarke et al., 1990), extending as far north as Eburru, however more detailed mapping work is required to fully constrain their geographic extent. Key exposures are located near the village of Maiella ~3 km east of the western Mau Escarpment (location 024 and 028 in Fig. 1c).

At location 024 (Fig. 2b and Fig. 3a), a 15-m-high section comprises at least 13 distinct pumice fall beds with subtle normal grading. Only rarely are these beds separated by a thin early-stage (orange stained) palaeosol horizon (<5 cm thick). The fall units themselves consist of light grey pumice lapilli that are highly angular and very well sorted with little to no fine ash matrix (Fig. 3b). The pumice lapilli are slightly porphyritic with sanidine phenocrysts visible in hand specimens. Abundant angular obsidian fragments occur evenly distributed throughout the beds. Within several of these beds, subtle stratifications are observed resulting from slight changes in the sorting from very well sorted with a maximum pumice size of 32 mm, to well sorted with a higher abundance of ~10 mm sized lapilli that are typically less angular (Fig. 3c). Their sorting combined with the lack of nearby vent suggests at these locations the MP represent medial distance fall deposits.

Componentry of the 0.5 mm size fraction (Fig. 7) indicates the Maiella Pumice is dominated by light grey pumice clasts (65–90%) that have a pantellerite glass composition (Fig. 8a-b), with minor amounts of tube pumice (5%). Obsidian is a notable component in some beds, accounting for up to 24%. Consistent with the slightly porphyritic nature of the pumice, single sanidine crystals represent 10%. Rare lava lithic fragments (<2%) and hydrothermally altered clasts (<3%) are also present. Based on the pantelleritic rhyolite glass composition and componentry, the Maiella Pumice could not be correlated to any other sampled deposit within the region, likely because it is overlain by younger Olkaria and Longonot deposits that infill the central portion of the rift. At location 024, six thin ash beds varying from 2 to 10 cm thick are interspersed between the MP beds (Fig. 3c). These ash beds extend across the entire outcrop and can be traced to a second outcrop exposing the same MP fall beds (028) ~600 m to the south. Glass composition of the ash fragments from one of these ash beds (024R) reveal they fall at the comenditic trachyte–phonolite boundary and are distinct from any of the trachyte pumice measured in this study (Fig. 8a).

$^{40}Ar/^{39}Ar$ dating of samples from the lowermost (024A) and uppermost (024Y) fall units constrains the age of the complete Maiella Pumice sequence to between 338.3 ± 2.1 ka and 332.8 ± 2.0 ka, respectively. Critically, these ages demonstrate that the Maiella Pumice predates all other exposed tephra deposits at both Olkaria and Longonot and represents a major phase of large, widespread explosive eruptions in the region related to early pantelleritic magmatism.

4.1.2. Olkaria PDCs (OP – ca. 42 ka)

The Olkaria PDCs unit (OP) is a 22-m-thick PDC sequence located at the entrance to a side valley of the main Ol Njorowa gorge in the centre of Olkaria (008; Fig. 1c, Fig. 2a and Fig. 4a). It is poorly sorted with an ash-dominated matrix with intercalated pumice lapilli up to 25 mm. Although the base was not observed, a 2-m-thick lithic-rich breccia exposed one kilometre to the west at the base of the Gorge Farm centre may represent a basal facies of the OP unit. This breccia contains lithic lava blocks up to 40 cm in diameter. It sits above several metres thick of alternating coarse–fine ash beds (not sampled) that are also exposed beneath the OP unit in the Ol Njorowa gorge. The upper 3–4 m of the OP unit transitions into a series of more granular fluid-based PDCs, where the deposit is clast-supported hosting a high concentration of sub-rounded pumice, obsidian and lithic fragments (up to 70 mm diameter), with each PDC having a large thickness variability (ranging from 1 m to ~10 cm over a 3 m distance) and often containing isolated pumice lenses, which was accessible further up the side gorge (036Y). The core of this unit is massive, ungraded and consists of meter-scale low-angle cross bedding with foresets that dip to the southeast, and laterally tapers out.

Pumice glass compositions are comenditic rhyolite with exceptionally high Cl contents (0.53 wt%; Fig. 8b, Fig. 9a and Fig. 10). Componentry shows that although OP is mostly composed of light grey pumice (37%), proportions of lithic lava (20%) and hydrothermally altered clasts (14%) are high (Fig. 7). Sanidine crystals (25%) also represent a significant proportion of the deposit, while obsidian is only a minor component (<1%). The high glass Cl contents could be correlated with the Olkaria Fall Breccia unit (see section 4.1.3) that sits stratigraphically above, but the depositional characteristics and componentry differ (PDC vs. fallout), suggesting both these units were derived from the same vent either as two different phases within the same eruption or two separate eruptions.

The stratigraphic relationships of the OP unit sitting beneath all other units within Olkaria demonstrate it erupted prior to most of the main dome-building events (Fig. 2a). $^{40}Ar/^{39}Ar$ dating from sanidines collected from the base (008C) and top (036Y) yields a consistent age between 42.4 ± 0.6 ka and 42.5 ± 0.6 ka, respectively. The deposit provides evidence for multiple explosive eruptions in Olkaria's early eruptive history. The massive, poorly-sorted nature and m-scale cross beds suggest deposition from a series of turbulent PDCs associated with repetitive eruption column collapse that is proximal to one of the nearby centres, likely Gorge Farm, which is supported by directions obtained by the orientation of the cross beds. The consistent age of the entire unit suggests deposition within a relatively short period. The lag breccia possibly marks an early high-energy collapse phase of one of these vents, consistent with the high lithics contents of the tephra, while the upper transitional deposits record waning current conditions.

4.1.3. Olkaria Fall Breccias (OFB – ca. 41–37 ka)

The Olkaria Fall Breccia (OFB) deposits are a series (at least 3 identified) of pyroclastic fall deposits stratigraphically overlying the OP unit and found in multiple locations in the centre (007), north (025–27), west (033) and south (005) of Olkaria (Fig. 1c and Fig. 2a). At one location near the centre of Olkaria (007; Fig. 4b; south-eastern margin of Gorge Farm), a 4–5 m thick pumice lapilli breccia represents the largest fallout deposit. It contains pumice blocks up to 30 cm diameter. The lower third is very poorly sorted with pumice blocks up to 20 cm set in a matrix of light grey fine ash. The upper two-thirds are well sorted and composed of pumice 5–30 cm in diameter. Underlying the pumice breccia is a ~2-m-thick, well-sorted light grey pumice lapilli fall deposit with subtle stratification; the bottom half shows reverse grading with maximum lapilli size ranging from 20 mm at the base to 35 mm in the middle, and the top half exhibits normal grading with lapilli up to 20

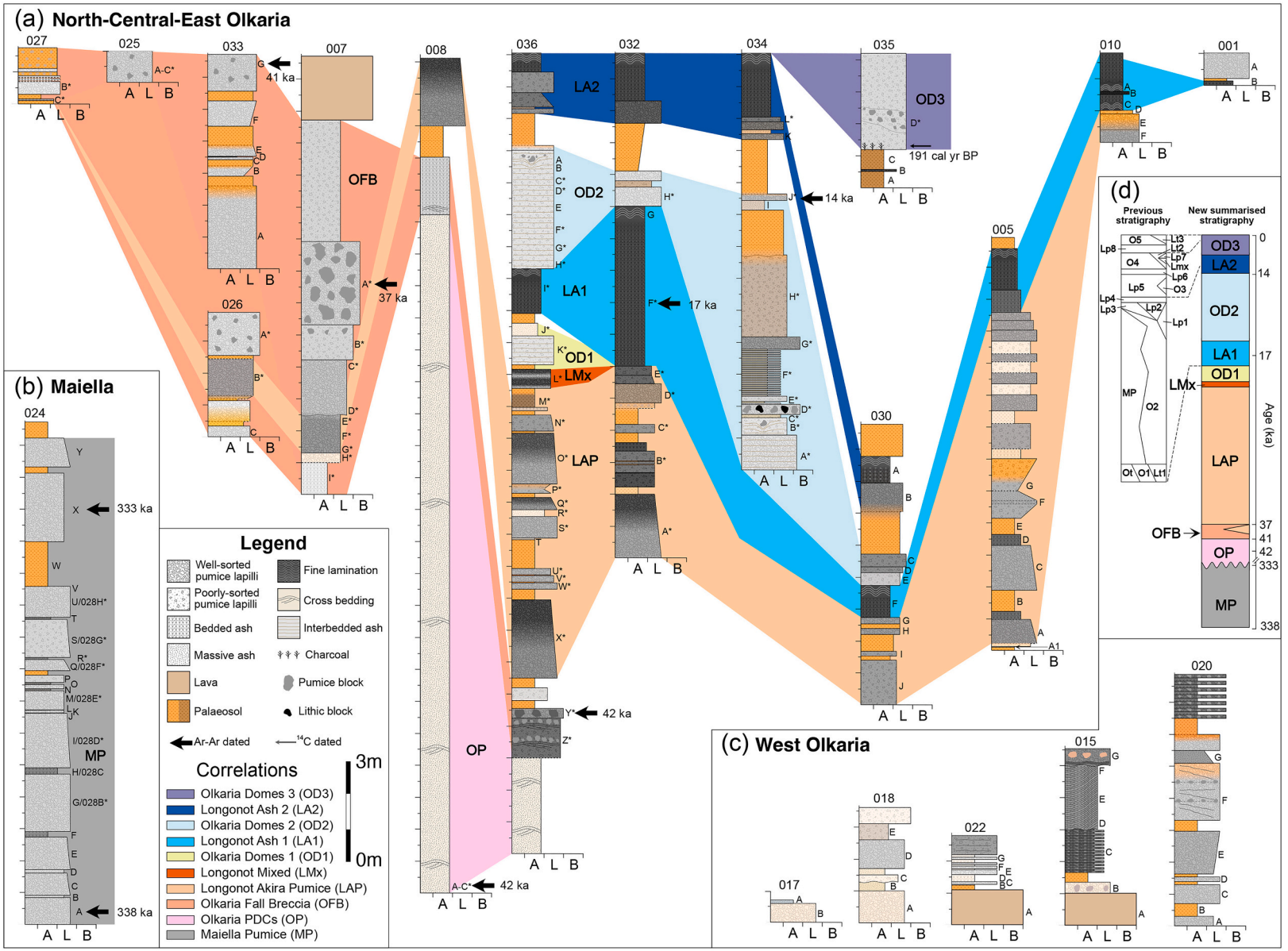

Fig. 2. Tephrostratigraphic framework of the Olkaria Volcanic Complex. (a) Correlation of tephra sections from the northern, central, and eastern regions of Olkaria. Correlations between sections are based on stratigraphic position, physical characteristics (e.g., deposit features, pumice colour, componentry), and pumice glass composition. Polygon colours used for correlations correspond to those used in the geochemical plots in Fig. 8–10. The bulk grain size of tephra deposits is indicated at the base of each logged section (A = ash; L = lapilli; B = blocks and bombs). A "*" next to the sample name denotes if glass chemistry has been measured. (b) Tephra section located on the western rift shoulder (Mau Escarpment) near Maiella town. The Maiella Pumice deposits represent a widespread sequence covering the entire Mau Escarpment in this portion of the rift. (c) Tephra sections from the western part of Olkaria, which remain uncorrelated with other deposits in the area. (d) Summarised chronostratigraphy of the 10 eruptive phases identified in the Olkaria Volcanic Complex. The ages are constrained from $^{40}Ar/^{39}Ar$ dating of feldspar crystals performed in this study. For comparison, the previously defined stratigraphic column of the Olkaria is displayed, modified after Clarke et al. (1990). (For interpretation of the references to colour in this figure legend, the reader is referred to the web version of this article.)

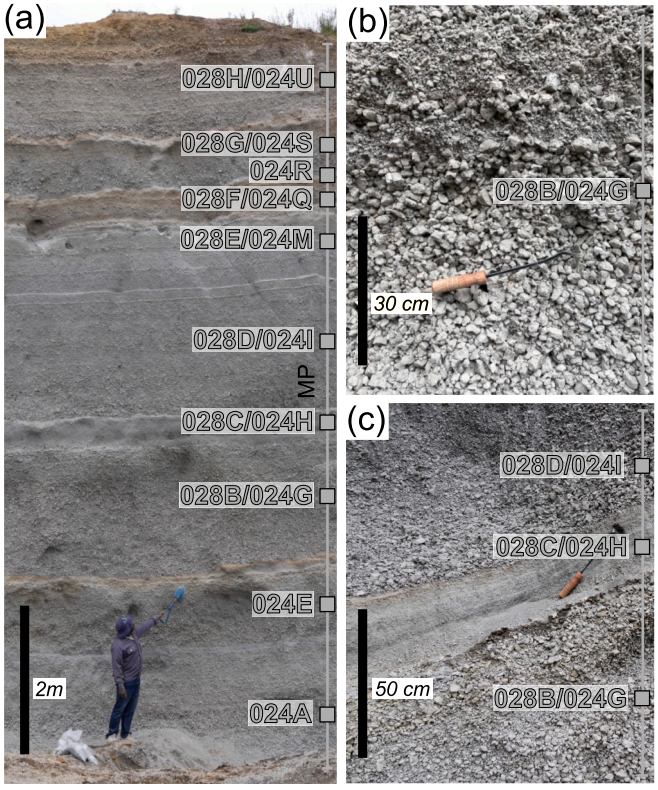

Fig. 3. Field photographs of tephrostratigraphic sections representing the Maiella Pumice (MP) at location 024. Samples collected from another section located ~600 m to the south are also labelled (location 028), which contained the same deposit sequence as 024. (a) A 10-m-high cliff face at location 024, displaying more than nine pumice fall deposits interbedded with finer ash layers. (b-c) Close-up views of MP pumice lapilli fall units at locations 024 and 028. Labelled symbols and colours correspond to those used in the geochemical plots in Fig. 8–10.

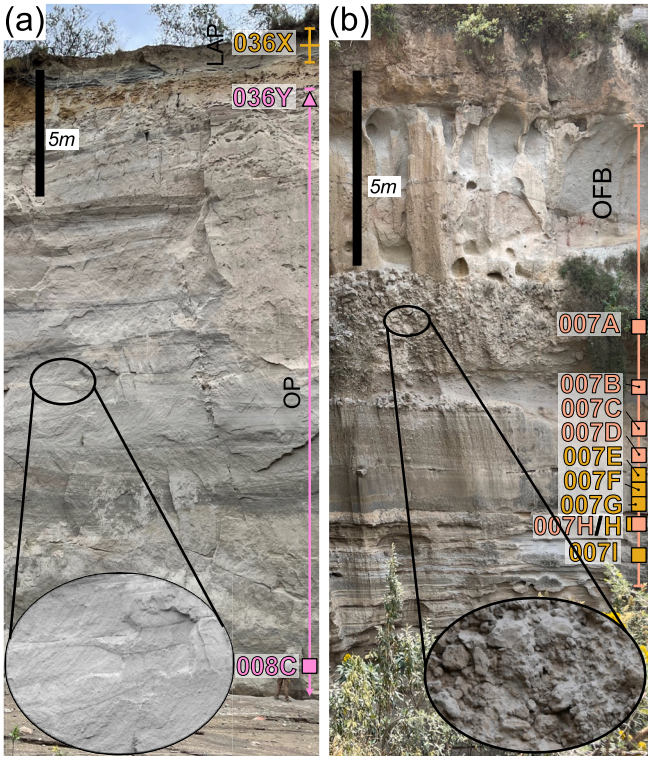

Fig. 4. Field photographs of tephrostratigraphic sections representing the Olkaria PDC unit (OP) and Olkaria Fallout Breccia unit (OFB), with corresponding sample locations. (a) A 22-m-high cliff face comprising multiple, massive PDC deposits exhibiting metre-scale cross-stratification. The inset highlights the cross-beds, indicative of PDC deposits. (b) A sequence of pumice-rich breccias and fall deposits situated stratigraphically above the OP unit shown in (a). The inset showcases the smooth, inflated textures of the pumice blocks within the OFB unit. Labelled symbols and colours correspond to those used in the geochemical plots in Fig. 8–10.

mm at the top. Glass composition is comenditic rhyolite with high Cl contents (>0.49 wt%), similar to pumice within the OP unit (Fig. 8b, Fig. 9a and Fig. 10). Componentry reveals these fallout deposits are dominated by light grey pumice (59–87%; Fig. 7), with less abundant lithic lava fragments (<16%), hydrothermally altered clasts (<13%), and very few obsidian shards (<5%) and tube pumice (<2%). A fine rhyolitic ash layer found ~13 km south (005A1 at location 005, outside the present day Olkaria complex) at the base of a series of LAP beds matches stratigraphically to the OFB unit (Fig. 1c and Fig. 2a).

Below the OFB fall deposits at location 007, an erosional contact separates them from a dark grey, very well-sorted, normally graded pumice lapilli unit that records a componentry and glass composition similar to the LAP (see section 4.1.4). Here, no soil horizon occurs between the two units but at other locations palaeosols were found (Fig. 2a). Based on componentry and glass composition, these LAP beds can also be found within other OFB deposits (location 026 and 027). Beneath this LAP bed at location 007 sits a >2-m-thick series of alternating rhyolitic ash and lapilli beds with abundant accretionary lapilli up to 10 mm in diameter (007H–I).

$^{40}Ar/^{39}Ar$ dating of two OFB deposits (033G and 007A) constrain the age of the OFB unit between 40.6 ± 0.5 ka and 36.6 ± 1.2 ka, respectively. The OFB sequence represents a series of fall deposits related to explosive eruptions at Olkaria, with early phases suggesting a phreatomagmatic component. Based on stratigraphic relationships and comparable glass composition to the OP unit, it suggests the OFB unit was sourced from a vent within the Gorge Farm centre. The presence of an LAP bed within this unit demonstrates both Olkaria and Longonot had overlapping eruptive periods.

4.1.4. *Longonot Akira Pumice (LAP – ca. 37–17 ka)*

The Longonot Akira Pumice (LAP) consists of a sequence of at least 11 stratified pumice lapilli fall beds associated with explosive volcanism at Longonot, extending to and beyond Olkaria (Fig. 1c, Fig. 2a and Fig. 5a). These fall beds overlap with the upper deposits of the OFB unit and continue well after. Type exposures occur between the Olkaria domes and the western caldera rim at Longonot (032), as well as in river valleys draining into the Ol Njorowa gorge (036).

Individual pumice lapilli beds are very well sorted and normally graded (Fig. 5b-c), ranging from several metres thick within Longonot's caldera rim to <2 m at more distal Olkaria sites. Each bed is separated by a pronounced palaeosol, with both fall units and soil horizons generally decreasing in thickness up section. At one Olkaria location (032), the maximum pumice sizes at the base of a bed are up to 50 mm. For most beds, a maximum pumice size varies from 33 mm at the base to 17 mm at the top (Fig. 5c). Very little fine ash matrix is present, with altered lithic clasts sporadically occurring towards the top of some beds. Angular obsidian clasts constitute a few percent of the deposits. Glass compositions of the pumice range from comenditic to pantelleritic trachytes (Fig. 8a-b and Fig. 9b). LAP deposits show a range in componentry for the 0.5 mm size fraction, notably the variable abundance of dark grey pumice lapilli (2–79%; Fig. 7) with abundant lithic lava (10–93%) and hydrothermally altered clasts (up to 14%), with only few free crystals (<2%) and obsidian (<4%). The main sequence of LAP beds act as a useful gauge for separating the earlier OP and OFB units from the younger Olkaria dome units.

Although not directly dated, from stratigraphic relationships with OFB and Longonot Ash 1, it is possible to bracket the LAP deposits

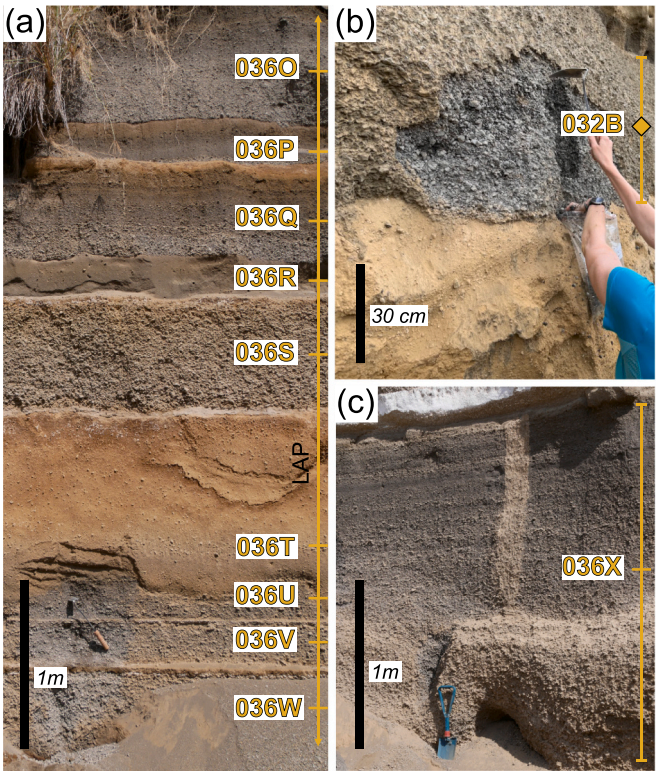

Fig. 5. Field photographs of tephrostratigraphic sections representing the Longonot Akira Pumice (LAP) deposits and corresponding sample locations. (a) A sequence of nine repetitive dark grey pumice lapilli deposits, each separated by a distinct palaeosol. (b) Close-up view of a typical LAP deposit overlying a pumice-rich palaeosol. (c) A normally graded pumice lapilli fall deposit displaying notable laminations towards the top of the sequence. Labelled symbols and colours correspond to those used in the geochemical plots in Fig. 8–10.

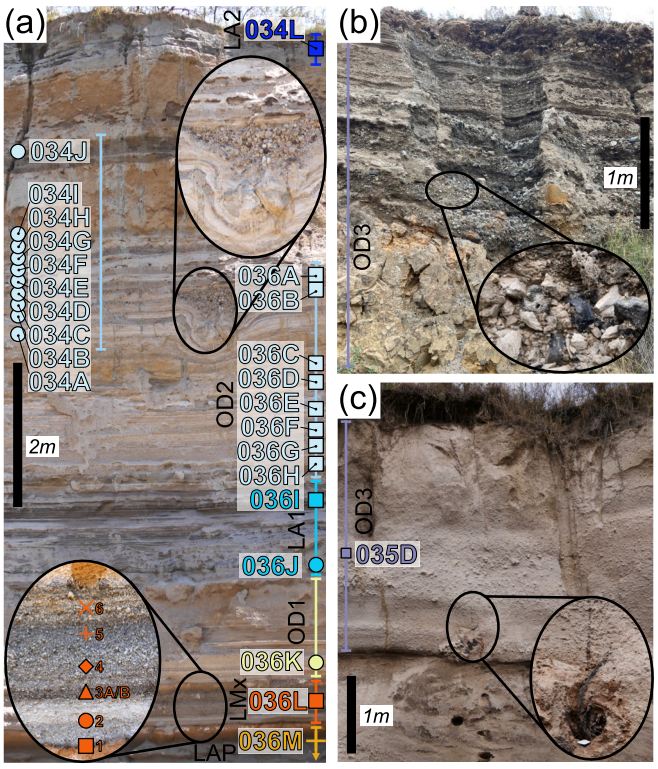

Fig. 6. Field photographs of tephrostratigraphic sections representing the Olkaria Domes and Longonot deposits, along with corresponding sample locations. (a) Type section displaying the Longonot Akira Pumice (LAP), Longonot Mixed Pumice (LMx), Olkaria Domes 1 (OD1), Longonot Ash 1 (LA1), Olkaria Domes 2 (OD2), and Longonot Ash 2 (LA2) deposits. The bottom inset highlights the colour variation throughout the LMx deposit, while the top inset showcases a bomb and sag feature characteristic of the OD2 deposits. (b) Photograph of the most recent Olkaria Dome 3 (OD3) deposits, located approximately 500 m east of the recently active Ololbutot vent. (c) A young PDC deposit associated with the ~190 cal yr BP explosive event at Ololbutot. The inset reveals charcoal fragments resulting from the incineration of branches and roots at the base of the PDC. Labelled symbols and colours correspond to those used in the geochemical plots in Fig. 8–10.

between 37 ka and 17 ka. This pumice sequence records multiple repetitive energetic eruption plumes and widespread fallout from a medial Longonot vent (now covered by more recent Longonot ash deposits) that dispersed widely to the west across the Olkaria complex. The well-sorted, normally graded beds record fallout from sustained Plinian eruption columns. The general decrease in thickness of individual beds and palaeosols upwards indicates waning explosive intensity with possibly an increased frequency with time. The consistently high lithic lava components in the finer ash fraction suggest these pumice beds were interspersed by lava effusion, likely constituting the construction of a central cone as previously suggested by Scott (1980) and Clarke et al. (1990), previously dated at 9.1 ± 0.1 ka (see section 5.1 for discussion on eruption timing).

4.1.5. *Longonot Mixed Pumice (LMx – ca. >17 ka)*

The Longonot Mixed Pumice (LMx) deposit is a pyroclastic fall unit found stratigraphically above the LAP, separated by a ~30 cm palaeosol, and below the Olkaria Domes 1 unit, separated by a 20 cm palaeosol (Fig. 6a). LMx is only observed in one location (036; Fig. 2a), a river valley feeding the Ol Njorowa gorge from the east. The unit can be divided into six subunits based on variations in pumice colour and composition (036L in Fig. 6a). Overall, the deposit is well sorted with no grading. The base is marked by a 1.5 cm layer of vesicular black scoria up to 10 mm in size with bimodal basaltic trachyandesite to trachyandesite glass compositions. Above this sits a 15 cm layer of dark grey trachytic pumice, with the central portion of this layer grading into a light grey pumice (L2). A 5 cm layer of dark grey–black vesicular clasts composed of a trachyandesite glass (L3) overlies L2. L3 is followed by a 21 cm layer of well sorted and normally graded dark grey trachyte pumice with clasts up to 15 mm at the base (L4) and 8 mm at the top (L5). The uppermost subunit (L6) is a 17 cm layer of mixed light and dark grey pumice.

The LMx deposit records an explosive eruption that likely tapped multiple magma reservoirs beneath Longonot volcano, first ejecting mafic material followed by trachyandesite compositions before typical Longonot trachyte, as evidenced by variations in glass composition between subunits (Fig. 8a and Fig. S2 in supplementary material (SM-6)). The deposit records a complex, multistage eruption event prior to the 16.9 ka Longonot Ash 1 deposit (see section 4.1.7) based on its stratigraphic position. This LMx unit correlates well with the Longonot mixed lavas previously described (Scott, 1980; Clarke et al., 1990; Scott and Bailey, 1984). However, these previous studies showed deconvolving the relationship between the different magma batches was challenging; the explosive products reported here decode this relationship more clearly.

4.1.6. *Olkaria Domes 1 (OD1 – ca. 17 ka)*

The Olkaria Domes 1 (OD1) deposit is a pyroclastic fall unit found between the LMx and Longonot Ash 1 deposits in a river valley feeding the Ol Njorowa gorge (036J–K in Fig. 1c, Fig. 2a and Fig. 6a). It is separated from the adjacent units by ~10 cm palaeosols. The deposit consists of alternating coarse ash layers (<2 cm thick) and light grey pumice lapilli beds (up to 5 cm thick). Some of the lapilli layers contain large angular pumice clasts taking up the entire thickness of the bed (i.e.,

Table 1
Synoptic overview of the main characteristics of the described units.

Unit	Previous nomenclature by Clarke et al. (1990)	Source	Stratigraphic position	Lithology & depositional features	Characteristic componentry	Glass composition	Emplacement mechanism	Magnitude
Maiella Pumice (MP)	Maiella Pumice Fmn (Mp)	Unknown	Above: N/A Below: All Olkaria and Longonot units	>13 major pumice lapilli beds Massive Individual fall bed thickness: 0.2–1.8 m	Light grey pumice (65–90%) Obsidian (<23%) Felsic crystals (<10%) Lithic lavas (<2%) Hydrothermally altered (<3%)	Pantelleritic rhyolite	Fallout	>5?
Olkaria Pyroclastic Surges (OP)	Olkaria Comendite Fmn: Lower-Middle Comendite Member (Op2–3)	Olkaria	Above: MP and Ol Njorowa gorge volcanics Below: OFB	Massive, poorly sorted unit Total thickness: 22 m Cross-bedded (m-scale)	Light grey pumice (37%) Felsic crystals (25%) Lithic lava (20%) Hydrothermally altered (14%) Obsidian (1%)	Comenditic rhyolite	PDCs	
Olkaria Fall Breccia (OFB)	Olkaria Comendite Fmn: Lower-Middle Comendite Member (Op2–3)	Olkaria	Above: OP Below: LAP	Pumice lapilli beds with pumice blocks (up 30 cm) Reverse grading Accretionary lapilli Individual fall bed thickness: 0.7–2.5 m	Light grey pumice (59–87%) Lithic lava (<11%) Hydrothermally altered (<14%) Obsidian (<2%)	Comenditic rhyolite	Fallout	4
Longonot Akira Pumice (LAP)	Akira Pumice Fmn: Lower Pumice (Lp5)	Longonot	Above: OP and OFB Below: LMx and OD1	>11 pumice lapilli beds Normal grading Individual fall bed thickness at Olkaria: 0.2–2.0 m	Dark grey pumice (2–79%) Lithic lavas (20–93%) Hydrothermally altered (5–14%) Obsidian (<4%)	Comenditic trachyte to pantelleritic trachyte	Fallout	4.5–4.9
Longonot Mixed Pumice (LMx)	Longonot Mixed Lava (Lmx1)	Longonot	Above: LAP Below: OD1	Chemically mixed pumice lapilli bed Light grey to dark grey layers (L1-L6) Basaltic vesicular clasts at base (L1)	Dark grey pumice (<63%) Lithic lavas (20–80%) Hydrothermally altered (<23%) Obsidian <4%) Felsic/mafic crystals (<3%)	Basaltic trachyandesites Trachyandesites Comenditic trachyte	Fallout	
Olkaria Domes 1 (OD1)	Olkaria Comendite Fmn: Upper Comendite Member (Op4)	Olkaria	Above: LMx Below: LA1	Alternating layers of coarse ash (<2 cm) and coarse lapilli pumice beds (<5 cm)	Light grey pumice (55–66%) Obsidian (6–10%) Lithic lava (15%) Hydrothermally altered (11–19%)	Comenditic rhyolite	Fallout	
Longonot Ash 1 (LA1)	Akira Pumice Formation: Bedded Ash (Lp6)	Longonot	Above: OD1 Below: OD2	Bedded coarse ash Finely laminated Sub-centimetre-scale cross-bedding Maximum total thickness observed: 5 m	Lithic lavas (86%) Dark grey pumice (2%) Obsidian (9%) Hydrothermally altered (3%) Felsic/mafic crystals (<1%)	Comenditic trachyte	PDCs and fallout	<4?
Olkaria Domes 2 (OD2)	Olkaria Comendite Fmn: Upper Comendite Member (Op4)	Olkaria	Above: LA1 Below: LA2	Pumice boulders (up to 40 cm) within pumice lapilli beds (<50 cm) Breadcrust bombs Sag structures with lithic blocks up to 43 cm Pumice and obsidian boulders Alternating coarse ash and fine lapilli layers (2–5 cm thick)	Light grey pumice (51–60%) Lithic lava (12–23%) Hydrothermally altered (<3%) Obsidian (1–6%)	Comenditic rhyolite	BAFs and fallout	<3?
Longonot Ash 2 (LA2)	Longonot Ash Fmn (Lp8)	Longonot	Above: OD2 Below: OD3	Bedded coarse ash Finely laminated Sub-centimetre-scale cross-bedding Pumice lapilli beds (<50 cm) marks the	Dark grey pumice (50%) Tube pumice (5%) Obsidian (20%) Lithic lava (23%)	Pantelleritic trachyte	PDCs and fallout	<4?

(*continued on next page*)

Table 1 (*continued*)

Unit	Previous nomenclature by Clarke et al. (1990)	Source	Stratigraphic position	Lithology & depositional features	Characteristic componentry	Glass composition	Emplacement mechanism	Magnitude
				base. Maximum total thickness observed: >2 m (top not observed)	Felsic/mafic crystals (<2%)			
Olkaria Domes 3 (OD3)	Olkaria Comendite Fmn: Ololbutot Comendite Member (Op5)	Olkaria	Above: All Below: LA2	BAFs: Pumice and obsidian boulders Angular obsidian blocks Inflated pumice PDCs: Poorly sorted, matrix supported. Massive with pumice lens towards middle Charcoal at base	–	Comenditic rhyolite	PDCs and BAFs	<2?

Table 2
Compilation of new and existing Olkaria and Longonot age constraints. The $^{40}Ar/^{39}Ar$ ages are given based on a 2σ standard error. Radiocarbon dates were calibrated in OxCal v.4.4 (Bronk Ramsey, 2009) using the SHCal20 calibration curve (Hogg et al., 2020).

Volcano	Sample	Location	Lithology	Unit	Method	Age[b]	Notes
Unknown[a]	OLK21-024A	0°50′29.42″S / 36°11′46.49″E	Pumice	MP	$^{40}Ar/^{39}Ar$	338.3 ± 2.1 ka	This study
Unknown[a]	OLK21-024X	0°50′29.42″S / 36°11′46.49″E	Pumice	MP	$^{40}Ar/^{39}Ar$	332.8 ± 2.0 ka	This study
Olkaria	OLK21-008C	0°53′52.50″S / 36°19′37.48″E	Pumice	OP	$^{40}Ar/^{39}Ar$	42.4 ± 0.6 ka	This study
Olkaria	OLK21-036Y	0°54′18.38″S / 36°20′45.83″E	Pumice	OFB	$^{40}Ar/^{39}Ar$	42.5 ± 0.6 ka	This study
Olkaria	OLK21-033G	0°51′2.16″S / 36°16′19.85″E	Pumice	OFB	$^{40}Ar/^{39}Ar$	40.6 ± 0.5 ka	This study
Olkaria	OLK21-007A	0°53′20.10″S / 36°19′16.22″E	Pumice	OFB	$^{40}Ar/^{39}Ar$	36.6 ± 1.2 ka	This study
Longonot	OLK21-032F	0°55′51.28″S / 36°22′16.29″E	Pumice	LA1	$^{40}Ar/^{39}Ar$	16.9 ± 0.5 ka	This study
Olkaria	OLK21-034J1	0°54′20.66″S / 36°21′26.43″E	Pumice	OD2	$^{40}Ar/^{39}Ar$	13.8 ± 1.0 ka	This study
Longonot	LP[5]	Unknown	Palaeosol	LAP	^{14}C	9150 ± 110 yr BP	Clarke et al. (1990)
Longonot	LP[8]	Unknown	Palaeosol	LA2	^{14}C	3280 ± 120 yr BP	Clarke et al. (1990)
Olkaria	OLK21-035D	0°54′18.49″S / 36°19′0.27″E	Charcoal	OD3	^{14}C	191 ± 23 cal yr BP[c]	This study

[a] Now inferred as Ololeri/Lake Naivasha based on this study.
[b] 95 % confidence.
[c] Based on an average of three uncalibrated ages of different charcoal samples within the same deposit: 224 ± 25 yr BP, 205 ± 25 yr BP, 235 ± 25 yr BP.

50 mm), but the majority of the beds contain lapilli up to 28 mm. Overall, the individual layers are well sorted, with abundant obsidian and lava lithic fragments present throughout. Componentry of the 0.5 mm fraction reveals a dominance of light grey pumice (66%; Fig. 7). Obsidian constitutes a notable proportion (10%), along with lithic lava (15%) and hydrothermally altered clasts (<19%), while free crystals are rare (<1%). Glass compositions of the light grey pumice are comenditic rhyolites that are compositionally distinct from the OP and OFB pumices (Fig. 8a-b and Fig. 9a; see section 4.2). The low percentage of dark grey pumices within the deposits are pantelleritic trachytes comparable to the composition obtained for the immediately overlying Longonot Ash 1 deposits (Fig. 8a). The Longonot Ash 1 unit has been dated at 16.9 ka, and although separated by a 10 cm palaeosol, the presence of Longonot pumice clasts within OD1 fall deposits suggest that Longonot and Olkaria domes could have erupted simultaneously. The nature of the alternating ash and lapilli beds together with high lithic contents reflect explosive medial fall deposits from dome eruptions with fluctuations in intensity. The deposits likely record periods of lava dome growth interrupted by intermittent small–moderate explosions, characteristic of an active rhyolitic lava dome field.

4.1.7. Longonot Ash 1 (LA1 – ca. 17 ka)

The Longonot Ash 1 (LA1) deposit represents a widespread pyroclastic unit found both within Olkaria and in surrounding areas of Longonot. It stratigraphically overlies the Olkaria Domes 1OD1 deposits in the Olkaria region (036 in Fig. 1c, Fig. 2a and Fig. 6a) and the LAP near Longonot (005 and 032). Total deposit thickness varies from ~5 m at more proximal locations to Longonot (032), to <1.3 m at more medial sites within Olkaria (005, 030, 036), with no palaeosol dividing the unit. The deposit is moderately well sorted and displays fine laminations with cross-bedding indicative of both fallout and PDC processes. It consists of dark grey beds alternating on the mm- to cm-scale between fine and coarse ash grain sizes, with rare pumice lapilli layers reaching up to 3 cm thick. Componentry shows a dominance of lithic lava fragments (86%; Fig. 7) along with minor amounts of dark grey pumice (2%), obsidian shards (9%), hydrothermally altered clasts (3%) and felsic free crystals (<1%). The glass composition is comenditic trachyte that falls within the range of the LAP deposits (Fig. 8a-b and Fig. 9b), but can be differentiated from the Longonot Ash 2 unit.

$^{40}Ar/^{39}Ar$ dates from sanidine crystals within LA1 (032F) constrain the age of the deposit to 16.9 ± 0.5 ka. Its unique position between the OD1 and OD2 units makes LA1 a useful marker bed across the area for both the onset of localised dome activity and a change in eruption style from the LAP unit at Longonot. The interbedding of fine and coarse ash indicates fluctuations in eruption intensity and columns, producing pulses of widespread tephra fallout interspersed with low-concentration/dilute PDCs.

4.1.8. Olkaria Domes 2 (OD2 – ca. 17–14 ka)

The Olkaria Domes 2 (OD2) deposit represents a series of very proximal pyroclastic deposits associated with dome formation within Olkaria. Thick successions of these deposits are found surrounding vents in central Olkaria (036 in Fig. 1c, Fig. 2a and Fig. 6a) and on the western flank of the Olkaria arcuate domes (034). The deposits are predominantly alternating ash and fine lapilli layers 2–5 cm thick, along with some poorly-sorted ash layers with pumice clasts up to 4 cm across.

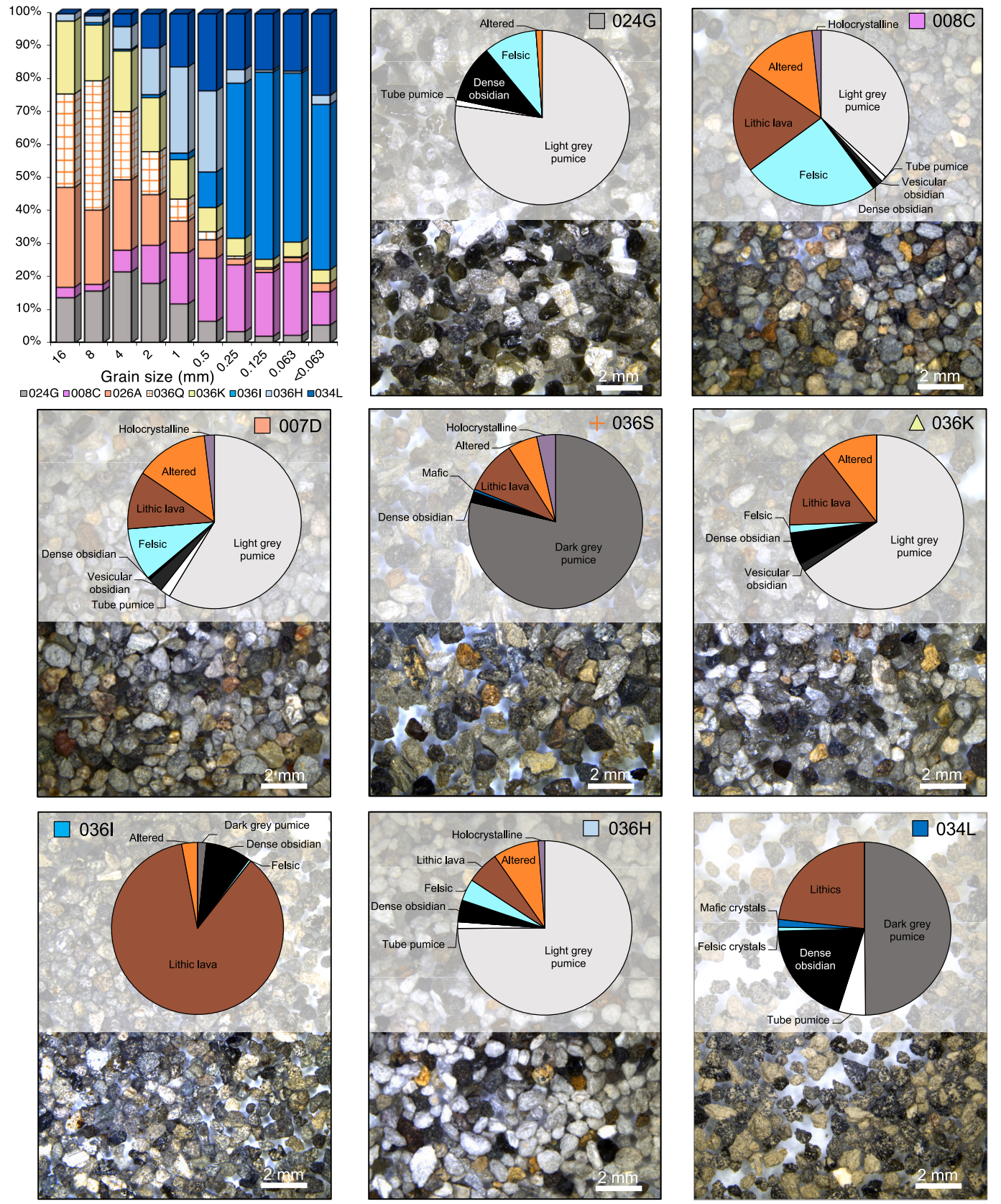

Fig. 7. Histogram displaying examples of the grain size distribution for typical deposits from each unit. Pie charts present the corresponding componentry for the 0.5–1 mm size fraction, accompanied by stereomicroscopic images of the respective components. The variability in light grey and dark grey pumice grains, as well as the lithic contents, serves to differentiate between Olkaria and Longonot tephra deposits.

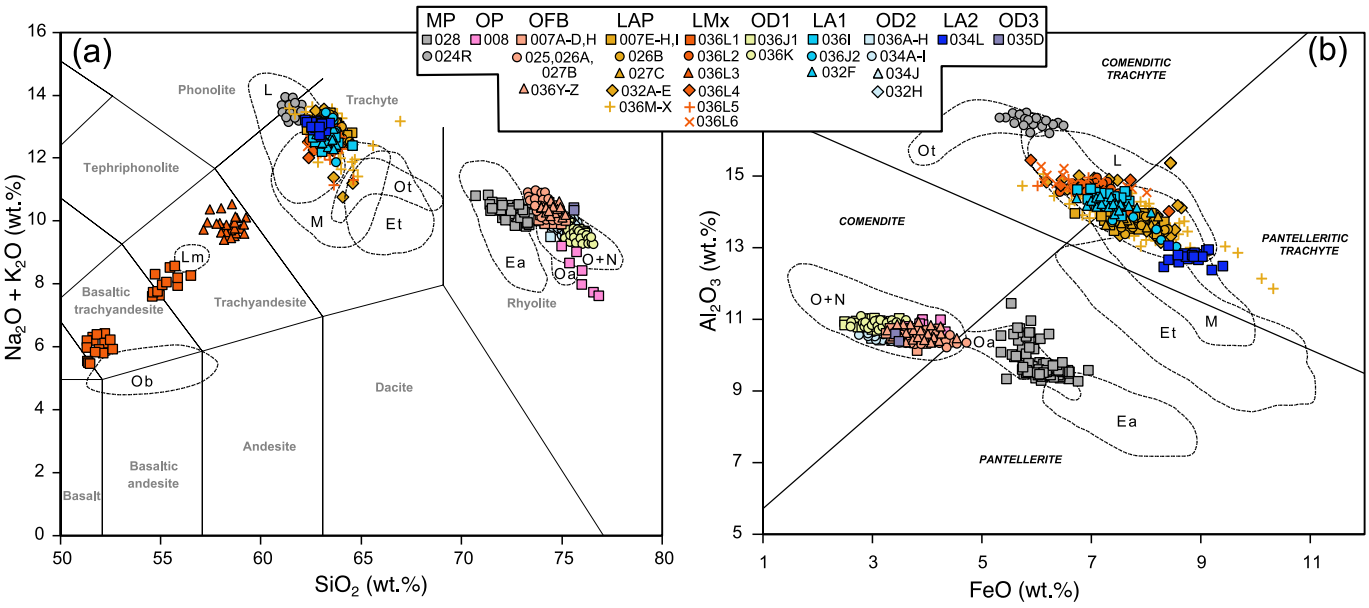

Fig. 8. Geochemical classification and comparison of Olkaria and Longonot pumice glasses. (a) Total Alkali versus Silica (TAS) plot (after Bas et al., 1986) comparing interstitial glass compositions of pumice from Olkaria and Longonot. Symbols and colours correspond to the different units identified in the tephrostratigraphy (Fig. 2). (b) Alkali classification plot based on major element chemistry (after MacDonald, 1974). Areas marked by dashed lines represent previously published whole-rock lava compositions (Clarke et al., 1990; Leat, 1984), including Olkaria (O) and Ndabibi (N) comendites, Olkaria and Ndabibi pantellerites (Oa), Olkaria trachytes (Ot), Olkaria basalts (Ob), Longonot trachytes (L), Longonot mixed lavas (Lm), Menengai trachytes (M), Eburru pantellerites (Ea), and Eburru trachytes (Et). (For interpretation of the references to colour in this figure legend, the reader is referred to the web version of this article.)

Several pumice lapilli layers up to 3 cm thick with several percent of lithic lava and obsidian fragments were also observed. Separating these lapilli layers are pronounced block-and-ash flow (BAF) deposits containing pumice boulders up to 40 cm. Some lithic-rich BAFs contain lava and obsidian blocks with only minor pumice clasts. In several locations along the different outcrops, sag structures containing breadcrust bombs up to 43 cm in diameter are present. Componentry is similar to the OFB unit, dominated by light grey pumice (50–80%; Fig. 7) with minor tube pumice (5%), along with less abundant lithic lava fragments (<20%), hydrothermally altered clasts (<20%) and obsidian (<6%). The glass composition is also comenditic rhyolite but more evolved compared to OFB pumice (Fig. 8a-b and Fig. 9a). The very proximal nature of these deposits makes correlating with other deposits further afield a challenge, as their deposition appears to be laterally restricted to the central and western area of Olkaria.

A fall deposit at the top of the succession was $^{40}Ar/^{39}Ar$ dated at 13.8 ± 1.0 ka, constraining the OD2 unit at 17–14 ka. Overall, these deposits represent a series of very proximal dome-forming products within Olkaria. Pumice-rich BAF deposits reflect explosive ejection and destruction of the lava domes, while lithic-rich BAFs indicate direct remobilisation of the dome material following its collapse. The poorly-sorted fine ash beds reflect unsteady eruption columns, with some pumice lapilli beds with increased lithic contents likely representing transitional fallout–BAF deposits.

4.1.9. Longonot Ash 2 (LA2 – ca. <14 ka)

The Longonot Ash 2 (LA2) deposit overlies the proximal OD2 unit separated by a ~1-m-thick palaeosol, notably above the Olkaria arcuate dome outcrops (034 and 036 in Fig. 1c, Fig. 2a and Fig. 6a). Within Longonot caldera itself, LA2 forms several metres thick successions of stratified ash layers. In terms of depositional features, LA2 is similar to the older LA1 deposits. However, componentry for LA2 reveals a significant abundance of dark grey pumice (50%) and obsidian (20%) with less lithic lava clasts (23%). It exhibits fine laminations and cross-bedding reflective of interbedded fallout and PDCs. It contains dark grey beds on the mm- to cm-scale that alternate between fine and coarse ash layers, with rare pumice lapilli beds (<3 cm thick). Sorting is comparably moderate to LA1 but has a more distributed grain size towards coarse ash–fine lapilli (Fig. 7). Importantly, the glass composition of the pumice is pantelleritic trachyte (Fig. 8a-b and Fig. 9b), unlike the comenditic trachyte composition of LA1, making the distinction during correlation possible.

As LA2 is separated from the underlying 13.8 ka Olkaria Domes 2 by a palaeosol, the stratigraphic context suggests the onset of this eruptive phase likely took place <13–14 ka. The upper contact was not observed and blankets the entirety of Longonot, suggesting ash eruptions have been a persistent feature at Longonot since 13 ka, and that Longonot may still remain in a phase of explosive ash venting tapping a pantelleritic trachyte magma reservoir. LA2 correlates with Longonot's upper bedded ash deposits described by Scott (1980) and Clarke et al. (1990) and believed to represent products from the excavation of the current summit crater previously dated at <3.5 ± 0.1 ka.

4.1.10. Olkaria Domes 3 (OD3 – ca. 191 cal yr BP)

The Olkaria Domes 3 (OD3) unit represents the youngest eruption phase at Olkaria, located within and around the Ololbutot centre. The most recently active vent is clearly defined by a young, 2.5 km long obsidian flow from a vent located at the southern tip of a N–S trending fissure which continues to intensely degas (Cappelli et al., 2023). Associated deposits include this obsidian lava flow marking the most recent effusive activity. Beneath the flow, excavations along the flanks of the southern Ololbutot vent reveal repetitive and localised BAF deposits composed of obsidian blocks (Fig. 6b; up to 50 cm) and inflated pumice clasts (up to 40 cm). These proximal deposits are notably fresh (i.e., no surface alteration) and sit above an older, altered flow unit. Approximately 2 km east at the base of the Ol Njorowa gorge, a 3-m-thick poorly-sorted PDC deposit containing a central blocky pumice lens (clasts up to 60 mm) was also identified (035 in Fig. 1c, Fig. 2a and Fig. 6c). Glass composition is comenditic rhyolitic, consistent with the Ololbutot obsidian flow (Fig. 8a-b and Fig. 9a). At the base of the PDC, thick charcoal fragments and carbonised wood were observed at several locations. Underlying the PDC is a 70 cm thick brown soil with elongated

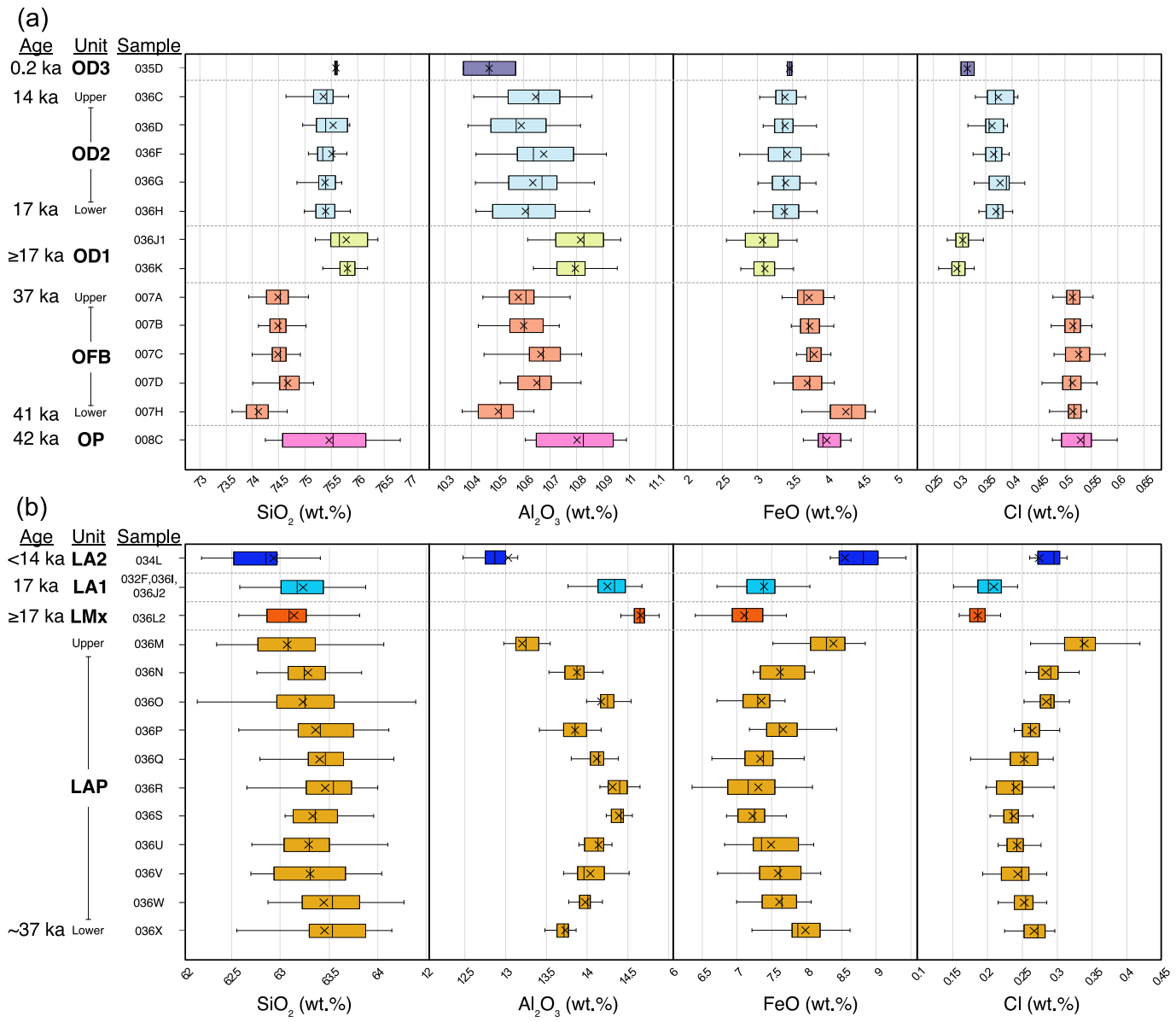

Fig. 9. Box plots of the temporal evolution in pumice glass composition for the Olkaria Volcanic Complex (a) and Longonot (b). The box highlights the 25th and 75th percentiles (the left and right of the boxes, respectively) and the whiskers show the data range. The vertical line in the box marks the median value and the cross represents the mean for that sample.

fine (30 × 1 mm) charcoal flakes tracing the contact with the overlying PDC. Three ^{14}C dates of the inner and outer section of the carbonised wood and the charcoal flakes report a consistent calibrated age of 191 ± 23 cal yr BP. Given the pristine morphology of the vent and lava flow, eruptive activity at the Ololbutot centre likely has persisted over the past few thousand years in the form of dome-building eruptions characterised by thick obsidian extrusion accompanied by proximal PDCs and BAFs. The ongoing degassing at the Ololbutot vent suggests magmatic processes continue at depth and could be the future source of renewed dome-building eruptions and associated hazards at Olkaria.

4.1.11. Additional deposits

In addition to the defined pyroclastic units described above (MP, OP, OFB, LAP, LMx, OD1, LA1, OD2, LA2, OD3), five uncorrelated sections west of the Ol Njorowa gorge around Olkaria Hill and Ololbutot were found in single outcrops (017, 015, 018, 020 and 022; Fig. 1c and Fig. 2b). The poor, intermittent exposure and high vegetation in these areas makes tracing these individual deposits a challenge, thus estimating the timing of deposition relative to the other well-defined units was not possible. These sections include a single ~60 cm thick well-sorted cream-coloured pumice lapilli breccia with a 10 cm light grey fine ash horizon containing abundant obsidian fragments (20%; 017); a 3.6 m section comprising three poorly-sorted lithic-rich PDC deposits containing abundant hydrothermally altered cream-coloured pumice clasts (>38%; 018); a highly altered and orange stained sequence of alternating pumice breccia and ash layers that are rich in light grey pumice (>66%) overlying a 3-m-thick dark grey granular and poorly-sorted PDC deposit and lava flow at the base (015); a 7.8 m thick sequence consisting of at least six well-sorted light grey pumice breccia fall beds containing abundant felsic free crystals (>25%), each separated by a 20–50 cm thick palaeosol, and overlain by a 90 cm thick sequence of poorly-sorted dark grey to black alternating fine ash and pumice lapilli breccia layers (020); and a 1.6 m sequence of alternating light grey pumice lapilli-rich and ash layers, with minor lithic (<15%) and obsidian clasts (<7%), with some layers containing abundant hydrothermal clasts (up to 70%), sitting above a lava flow unit (022).

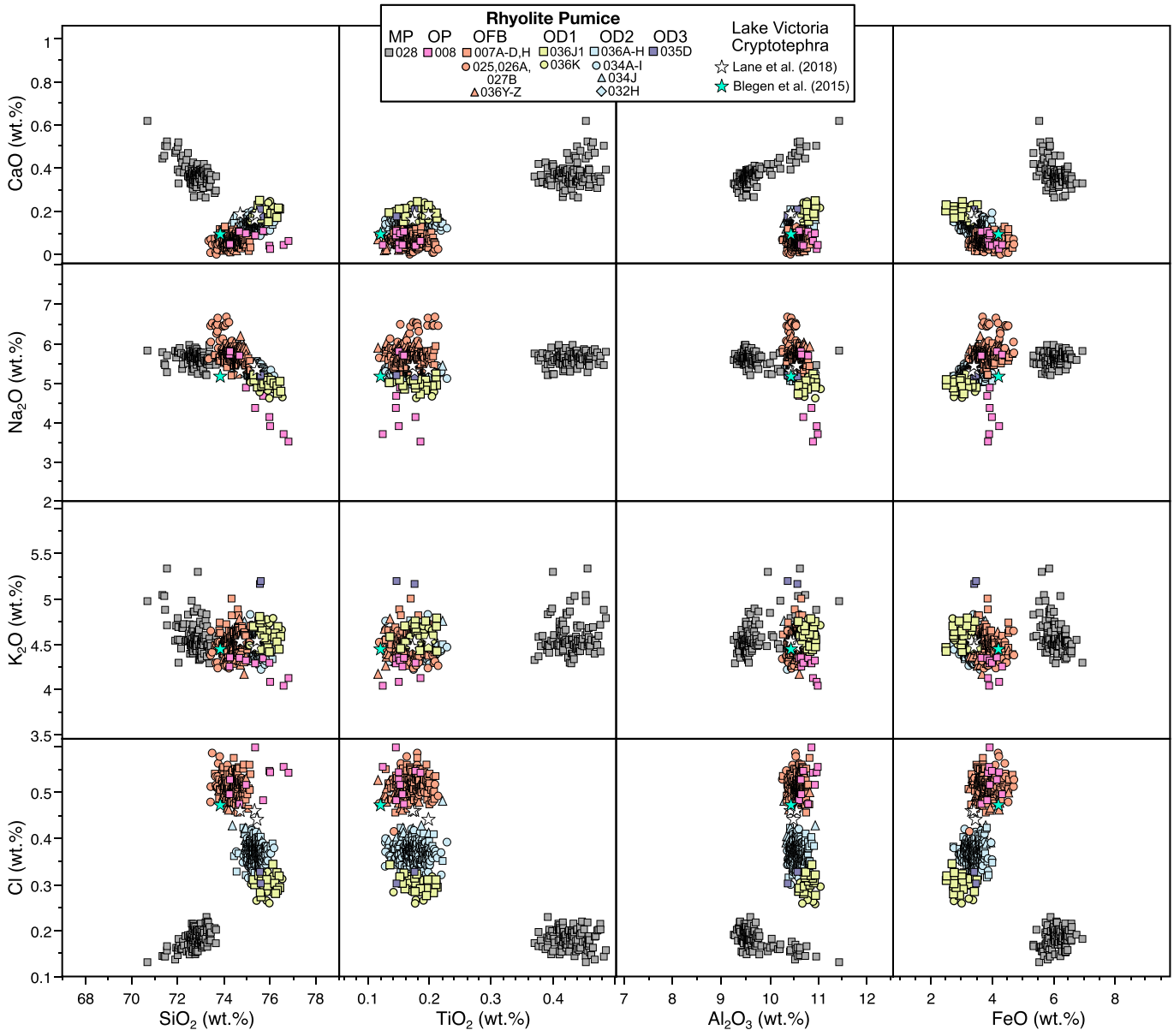

Fig. 10. Matrix of binary plots displaying the glass major element compositions of Olkaria rhyolite pumice from the different eruptive units. The data highlights several of the eruptive units plotting in unique clusters (MP, OP/OFB, OD1 and OD2–3). Glass composition of cryptotephras retrieved from Lake Victoria (Blegen et al., 2015; Lane et al., 2018) are also shown for comparison. (For interpretation of the references to colour in this figure legend, the reader is referred to the web version of this article.)

Although these sections were not easily correlated to one of the main units above, it is likely they represent localised fall and PDC units from the nearby Olkaria Hill and Ololbutot centres possibly being deposited <14 ka when these vents were active.

4.2. Glass chemistry

4.2.1. Major element composition

Major element glass compositions of pumice collected within the Olkaria and Longonot region are all peralkaline and either rhyolitic or trachytic. The average major element compositions of all the selected pumice deposits are presented in Table 3, with the full dataset in the supplementary material (SM-3 and SM-6). Pumice from Olkaria, Longonot and Maiella each form separate geochemical groups (Fig. 8 and Fig. S3 in SM-6). Comenditic rhyolites are characteristic of Olkaria deposits, with some straddling the comendite–pantellerite boundary. Longonot pumice represents a continuum from comenditic trachytes to pantelleritic trachytes, except for one deposit (LMx) containing pumice clasts with more mafic glass compositions. The Maiella Pumice form a single unique composition of pantelleritic rhyolites. All major element glass compositions from Olkaria and Longonot are consistent with previous analyses of lavas (Fig. 8; Clarke et al., 1990; Davies and Macdonald, 1987; Macdonald et al., 2008; Marshall et al., 2009), but distinct from other nearby large volcanic centres (e.g., Eburru, Leat, 1984; Ren et al., 2006).

Each Olkaria unit identified in the field and described in section 4.1 (OP, OFB, OD1, OD2, OD3; some of which represent multiple eruptions) forms a tight homogenous composition within the larger comenditic rhyolite group. However, from binary plots alone some units have a compositional overlap making correlation between many Olkaria deposits using major element glass composition complicated (Fig. 8, Fig. 9 and Fig. 10). The OP and OFB deposits share overlapping glass compositions for all major elements. Collectively, they have the lowest SiO_2 (73.8–74.7 wt%) and CaO (0.03–0.08 wt%), and highest FeO (3.7–4.3

Table 3
Glass major element compositions (wt%) of the described Olkaria and Longonot units. Presented data are average pumice glass compositions (2 σ deviation in brackets) of single deposits from the different units. The full dataset is provided in the supplementary material. N indicates the number of analyses per sample.

Sample	Unit	Deposit	N	SiO_2	TiO_2	Al_2O_3	FeO	MnO	MgO	CaO	Na_2O	K_2O	P_2O_5	Cl	Total
OLK21-				74.49	0.17	10.58	3.73	0.16	0.02	0.06	5.71	4.55	0.02	0.51	
007A	OFB	Pumice	19	(0.54)	(0.02)	(0.08)	(0.23)	(0.28)	(0.01)	(0.02)	(0.13)	(0.07)	(0.02)	(0.02)	95.59
OLK21-				74.49	0.18	10.6	3.75	0.1	0.01	0.07	5.72	4.55	0.01	0.52	
007B	OFB	Pumice	25	(0.4)	(0.02)	(0.09)	(0.14)	(0.1)	(0.01)	(0.02)	(0.13)	(0.1)	(0.02)	(0.02)	95.30
OLK21-				74.49	0.18	10.67	3.81	0.12	0.02	0.07	5.57	4.54	0.02	0.53	
007C	OFB	Pumice	25	(0.39)	(0.01)	(0.09)	(0.16)	(0.22)	(0.01)	(0.02)	(0.12)	(0.06)	(0.03)	(0.02)	93.88
OLK21-				74.66	0.16	10.65	3.71	0.14	0.01	0.06	5.46	4.61	0.01	0.51	
007D	OFB	Pumice	24	(0.39)	(0.02)	(0.08)	(0.25)	(0.17)	(0.01)	(0.02)	(0.12)	(0.14)	(0.02)	(0.02)	93.09
OLK21-				63.48	0.49	13.71	7.66	0.34	0.08	0.94	8.08	4.89	0.06	0.27	
007E	LAP	Pumice	25	(0.92)	(0.02)	(0.19)	(0.31)	(0.17)	(0.03)	(0.03)	(0.27)	(0.14)	(0.05)	(0.02)	95.83
OLK21-				63.33	0.49	13.81	7.71	0.48	0.09	0.95	7.99	4.85	0.05	0.27	
007F	LAP	Pumice	25	(0.51)	(0.02)	(0.14)	(0.37)	(0.32)	(0.02)	(0.04)	(0.21)	(0.09)	(0.04)	(0.02)	94.70
OLK21-				63.47	0.47	13.75	7.78	0.34	0.08	0.93	8.01	4.87	0.04	0.28	
007G	LAP	Pumice	20	(0.66)	(0.02)	(0.12)	(0.28)	(0.13)	(0.02)	(0.06)	(0.22)	(0.08)	(0.04)	(0.02)	94.56
OLK21-				74.11	0.17	10.5	4.26	0.1	0.01	0.08	5.7	4.53	0.02	0.52	
007H	OFB	Pumice	17	(0.42)	(0.01)	(0.08)	(0.29)	(0.11)	(0.01)	(0.02)	(0.1)	(0.1)	(0.02)	(0.02)	92.88
OLK21-				61.94	0.44	14.64	7.51	0.47	0.1	0.95	8.82	4.71	0.05	0.36	
007H	LAP	Pumice	10	(0.8)	(0.05)	(1.11)	(0.49)	(0.38)	(0.04)	(0.07)	(1.22)	(0.12)	(0.04)	(0.12)	96.26
OLK21-				63.16	0.48	14.2	7.57	0.3	0.08	0.97	8.06	4.83	0.04	0.3	
007I	LAP	Pumice	14	(0.9)	(0.04)	(0.64)	(0.39)	(0.19)	(0.04)	(0.09)	(0.42)	(0.15)	(0.03)	(0.06)	94.07
OLK21-				75.46	0.15	10.8	3.99	0.08	0.01	0.07	4.65	4.25	0.03	0.53	
008C	OP	Pumice	10	(0.59)	(0.01)	(0.08)	(0.19)	(0.08)	(0.01)	(0.03)	(0.78)	(0.12)	(0.04)	(0.03)	92.04
OLK21-				61.55	0.5	16.53	5.89	0.32	0.23	1	8.28	5.32	0.06	0.32	
024R	MP	Pumice	21	(0.51)	(0.02)	(0.13)	(0.33)	(0.11)	(0.02)	(0.05)	(0.16)	(0.14)	(0.04)	(0.02)	98.71
OLK21-				73.83	0.19	10.45	4.07	0.06	0.01	0.03	6.48	4.36	0.01	0.52	
025C	OFB	Pumice	14	(0.59)	(0.02)	(0.08)	(0.29)	(0.06)	(0.01)	(0.01)	(0.11)	(0.08)	(0.02)	(0.02)	92.74
OLK21-				73.97	0.16	10.43	4.33	0.08		0.06	5.95	4.45	0.02	0.54	
026A	OFB	Pumice	9	(0.32)	(0.01)	(0.09)	(0.24)	(0.09)	0 (0.01)	(0.02)	(0.13)	(0.1)	(0.02)	(0.02)	94.08
OLK21-				63.64	0.48	13.61	7.87	0.24	0.06	0.86	8.13	4.77	0.05	0.29	
026B1	LAP	Pumice	12	(1.26)	(0.02)	(0.27)	(0.35)	(0.11)	(0.01)	(0.05)	(0.42)	(0.08)	(0.03)	(0.02)	96.35
OLK21-				74.45	0.17	10.75	3.72	0.09	0.01	0.07	5.66	4.57	0.02	0.5	
027B	OFB	Pumice	10	(0.46)	(0.02)	(0.3)	(0.27)	(0.08)	(0.01)	(0.01)	(0.07)	(0.25)	(0.03)	(0.03)	94.27
OLK21-				63.53	0.48	13.71	7.81	0.27	0.07	0.92	8.11	4.81	0.04	0.27	
027C	LAP	Pumice	12	(0.88)	(0.02)	(0.18)	(0.32)	(0.13)	(0.02)	(0.05)	(0.14)	(0.07)	(0.03)	(0.02)	97.29
OLK21-				72.8	0.42	9.57	6.36	0.09	0.01	0.33	5.76	4.45	0.01	0.19	
028B2	MP	Pumice	11	(0.31)	(0.02)	(0.07)	(0.34)	(0.12)	(0.01)	(0.04)	(0.09)	(0.08)	(0.02)	(0.02)	94.21
OLK21-				73.06	0.44	9.37	6.18	0.25	0.01	0.34	5.67	4.46	0.03	0.2	
028B3	MP	Pumice	9	(0.5)	(0.02)	(0.1)	(0.35)	(0.16)	(0.02)	(0.03)	(0.13)	(0.07)	(0.05)	(0.01)	94.00
OLK21-				73.04	0.42	9.55	6.09	0.2	0.01	0.35	5.57	4.56	0.01	0.19	
028B4	MP	Pumice	15	(0.49)	(0.02)	(0.07)	(0.2)	(0.12)	(0.01)	(0.03)	(0.13)	(0.14)	(0.02)	(0.01)	93.74
OLK21-				72.95	0.43	9.49	6.23	0.13	0.01	0.36	5.68	4.51	0.03	0.19	
028D	MP	Pumice	9	(0.46)	(0.02)	(0.09)	(0.24)	(0.07)	(0.01)	(0.01)	(0.11)	(0.06)	(0.03)	(0.02)	93.55
OLK21-				72.77	0.45	9.7	6.13	0.19		0.37	5.6	4.59	0.03	0.18	
028E	MP	Pumice	12	(0.59)	(0.02)	(0.33)	(0.23)	(0.12)	0 (0.01)	(0.05)	(0.15)	(0.11)	(0.04)	(0.02)	93.74
OLK21-				72.67	0.42	9.63	6.14	0.21	0.01	0.38	5.71	4.64	0.03	0.18	
028F	MP	Pumice	10	(0.68)	(0.02)	(0.11)	(0.21)	(0.15)	(0.01)	(0.02)	(0.16)	(0.11)	(0.02)	(0.02)	93.85
OLK21-				72.7	0.44	9.71	6.21	0.14	0.01	0.37	5.63	4.6	0.02	0.18	
028G	MP	Pumice	18	(0.55)	(0.02)	(0.33)	(0.24)	(0.09)	(0.01)	(0.03)	(0.17)	(0.15)	(0.03)	(0.01)	94.04
OLK21-				72.93	0.41	9.8	5.97	0.21	0.01	0.38	5.58	4.51	0.02	0.18	
028H	MP	Pumice	14	(0.4)	(0.02)	(0.31)	(0.26)	(0.13)	(0.01)	(0.04)	(0.14)	(0.07)	(0.03)	(0.01)	93.87
OLK21-				72.05	0.44	10.53	5.7	0.22	0.01	0.47	5.56	4.83	0.03	0.15	
028J	MP	Pumice	14	(0.59)	(0.02)	(0.39)	(0.2)	(0.12)	(0.01)	(0.06)	(0.19)	(0.23)	(0.02)	(0.01)	93.77
OLK21-				63.33	0.5	14.07	7.61	0.4	0.13	0.9	7.77	4.96	0.05	0.28	
032A	LAP	Pumice	18	(0.82)	(0.03)	(0.25)	(0.35)	(0.19)	(0.03)	(0.05)	(0.85)	(0.15)	(0.03)	(0.02)	95.20
OLK21-				63.14	0.5	13.38	8.16	0.38	0.08	0.79	8.51	4.7	0.03	0.32	
032B2	LAP	Pumice	14	(0.75)	(0.03)	(0.17)	(0.28)	(0.3)	(0.02)	(0.05)	(0.28)	(0.13)	(0.04)	(0.01)	97.89
OLK21-				62.93	0.59	14.88	7.15	0.28	0.21	1.12	7.32	5.2	0.13	0.19	
032C	LAP	Pumice	6	(0.79)	(0.02)	(0.23)	(0.28)	(0.3)	(0.01)	(0.03)	(0.23)	(0.15)	(0.11)	(0.01)	96.81
OLK21-				63.35	0.56	14.62	6.9	0.24	0.17	1.09	7.61	5.23	0.06	0.17	
032D	LAP	Pumice	20	(1.04)	(0.02)	(0.22)	(0.34)	(0.19)	(0.03)	(0.05)	(0.24)	(0.16)	(0.05)	(0.01)	97.01
OLK21-				63.4	0.54	14.45	6.99	0.33	0.15	1.04	7.74	5.11	0.08	0.19	
032E	LAP	Pumice	18	(0.84)	(0.02)	(0.23)	(0.33)	(0.15)	(0.02)	(0.05)	(0.16)	(0.14)	(0.06)	(0.02)	97.07
OLK21-				63.29	0.57	14.22	7.29	0.35	0.17	1.12	7.65	5.07	0.07	0.19	
032F	LAP	Pumice	18	(0.98)	(0.03)	(0.24)	(0.32)	(0.14)	(0.01)	(0.04)	(0.29)	(0.14)	(0.06)	(0.01)	96.28
OLK21-				75.45	0.17	10.6	3.36	0.1	0.02	0.14	5.29	4.49	0.02	0.36	
032H	OD1	Pumice	20	(0.52)	(0.02)	(0.07)	(0.21)	(0.08)	(0.01)	(0.02)	(0.13)	(0.08)	(0.04)	(0.02)	93.81
OLK21-				75.39	0.18	10.53	3.47	0.08	0.01	0.15	5.29	4.53	0.01	0.36	
034A	OD2	Pumice	20	(0.41)	(0.02)	(0.08)	(0.21)	(0.07)	(0.01)	(0.02)	(0.1)	(0.09)	(0.02)	(0.02)	94.60
OLK21-				75.45	0.17	10.52	3.39	0.1	0.01	0.14	5.37	4.47	0.02	0.36	
034B	OD2	Pumice	20	(0.9)	(0.02)	(0.16)	(0.17)	(0.1)	(0.01)	(0.02)	(0.13)	(0.09)	(0.02)	(0.02)	96.36
OLK21-				75.44	0.17	10.52	3.45	0.11	0.01	0.14	5.28	4.5	0.02	0.37	
034C	OD2	Pumice	19	(0.4)	(0.02)	(0.09)	(0.21)	(0.12)	(0.01)	(0.02)	(0.08)	(0.1)	(0.02)	(0.02)	94.12

(*continued on next page*)

Table 3 (*continued*)

Sample	Unit	Deposit	N	SiO_2	TiO_2	Al_2O_3	FeO	MnO	MgO	CaO	Na_2O	K_2O	P_2O_5	Cl	Total
OLK21-034D	OD2	Pumice	20	75.44 (0.63)	0.17 (0.02)	10.53 (0.1)	3.42 (0.2)	0.09 (0.1)	0.01 (0.01)	0.14 (0.02)	5.36 (0.11)	4.45 (0.09)	0.01 (0.03)	0.37 (0.02)	94.92
OLK21-034E	OD2	Pumice	19	75.35 (0.72)	0.17 (0.01)	10.57 (0.08)	3.41 (0.23)	0.09 (0.1)	0.01 (0.01)	0.19 (0.18)	5.33 (0.13)	4.51 (0.09)	0.01 (0.02)	0.36 (0.02)	94.22
OLK21-034F	OD2	Pumice	10	75.34 (0.6)	0.18 (0.02)	10.56 (0.04)	3.4 (0.15)	0.05 (0.08)	0.01 (0.01)	0.14 (0.02)	5.3 (0.18)	4.63 (0.08)	0.01 (0.02)	0.37 (0.02)	94.55
OLK21-034G	OD2	Pumice	20	75.49 (0.53)	0.18 (0.02)	10.56 (0.09)	3.37 (0.25)	0.12 (0.14)	0.01 (0.01)	0.15 (0.02)	5.28 (0.09)	4.46 (0.1)	0.02 (0.03)	0.38 (0.02)	94.43
OLK21-034H	OD2	Pumice	19	75.56 (0.46)	0.18 (0.02)	10.61 (0.08)	3.43 (0.25)	0.09 (0.1)	0.01 (0.01)	0.14 (0.02)	5.12 (0.51)	4.47 (0.12)	0.03 (0.03)	0.36 (0.01)	93.99
OLK21-034J	OD2	Pumice	20	75.12 (0.86)	0.17 (0.02)	10.48 (0.18)	3.59 (0.2)	0.13 (0.15)	0.01 (0.02)	0.12 (0.02)	5.4 (0.11)	4.56 (0.09)	0.01 (0.02)	0.4 (0.02)	94.09
OLK21-034L	LA2	Pumice	20	62.9 (0.75)	0.58 (0.08)	13.03 (0.68)	8.53 (1.01)	0.37 (0.14)	0.14 (0.02)	1 (0.07)	8.38 (0.28)	4.74 (0.18)	0.06 (0.05)	0.28 (0.05)	98.55
OLK21-035D	OD3	Pumice	2	75.58 (0.35)	0.16 (0.02)	10.47 (0.15)	3.46 (0.01)	0 (0)	0.02 (0.01)	0.19 (0.02)	5.18 (0.01)	5.18 (0.01)	0 (0)	0.32 (0.01)	97.65
OLK21-036C	OD2	Pumice	19	75.35 (0.43)	0.18 (0.02)	10.65 (0.1)	3.4 (0.2)	0.17 (0.21)	0.01 (0.01)	0.15 (0.02)	5.22 (0.13)	4.5 (0.09)	0.01 (0.02)	0.37 (0.02)	94.66
OLK21-036D	OD2	Pumice	19	75.53 (0.56)	0.17 (0.02)	10.59 (0.07)	3.39 (0.23)	0.14 (0.2)	0.01 (0.01)	0.16 (0.02)	5.14 (0.48)	4.48 (0.09)	0.02 (0.04)	0.36 (0.02)	94.66
OLK21-036F	OD2	Pumice	19	75.51 (0.61)	0.18 (0.01)	10.68 (0.1)	3.42 (0.3)	0.15 (0.22)	0.01 (0.01)	0.15 (0.02)	5.01 (0.64)	4.51 (0.08)	0.02 (0.02)	0.36 (0.02)	94.60
OLK21-036G	OD2	Pumice	11	75.38 (0.81)	0.17 (0.01)	10.63 (0.14)	3.4 (0.22)	0.18 (0.26)	0.01 (0.01)	0.15 (0.01)	5.19 (0.12)	4.49 (0.07)	0.03 (0.04)	0.38 (0.02)	94.84
OLK21-036H	OD2	Pumice	21	75.39 (0.44)	0.17 (0.01)	10.61 (0.11)	3.39 (0.23)	0.1 (0.12)	0.01 (0.01)	0.14 (0.02)	5.31 (0.14)	4.51 (0.07)	0.01 (0.01)	0.37 (0.02)	94.28
OLK21-036I	LA1	Pumice	29	63.17 (0.46)	0.56 (0.03)	14.48 (0.23)	7.25 (0.41)	0.3 (0.17)	0.17 (0.02)	1.16 (0.06)	7.75 (0.16)	4.89 (0.11)	0.07 (0.04)	0.2 (0.02)	98.55
OLK21-036J1	OD1	Pumice	22	75.78 (0.56)	0.18 (0.02)	10.81 (0.12)	3.08 (0.27)	0.08 (0.21)	0.02 (0.01)	0.18 (0.02)	4.94 (0.11)	4.59 (0.12)	0.02 (0.03)	0.31 (0.01)	95.11
OLK21-036J2	LA1	Pumice	13	63.32 (0.73)	0.51 (0.03)	13.76 (0.44)	7.71 (0.55)	0.35 (0.17)	0.12 (0.02)	0.97 (0.16)	8.25 (0.37)	4.7 (0.14)	0.05 (0.04)	0.26 (0.04)	96.72
OLK21-036K	OD1	Pumice	30	75.8 (0.4)	0.18 (0.01)	10.8 (0.08)	3.11 (0.21)	0.08 (0.14)	0.02 (0.01)	0.19 (0.02)	4.89 (0.12)	4.62 (0.08)	0.02 (0.02)	0.3 (0.02)	94.95
OLK21-036L1	LMx	Pumice	18	51.87 (0.53)	2.82 (0.04)	15.02 (0.12)	11.33 (0.36)	0.29 (0.17)	3.96 (0.15)	7.7 (0.21)	3.95 (0.2)	2.08 (0.11)	0.9 (0.1)	0.07 (0.01)	98.05
OLK21-036L1	LMx	Pumice	12	55.29 (0.63)	2.1 (0.11)	15.32 (0.15)	9.81 (0.37)	0.25 (0.26)	2.78 (0.15)	5.71 (0.31)	5.15 (0.2)	2.9 (0.12)	0.61 (0.07)	0.09 (0.01)	98.59
OLK21-036L2	LMx	Pumice	18	63.1 (0.82)	0.56 (0.02)	14.66 (0.2)	7.08 (0.39)	0.35 (0.23)	0.17 (0.02)	1.13 (0.05)	7.69 (0.21)	5.01 (0.13)	0.07 (0.04)	0.19 (0.02)	97.64
OLK21-036L3 (A)	LMx	Pumice	30	58.35 (0.47)	1.65 (0.05)	16.15 (0.11)	7.62 (0.31)	0.28 (0.26)	1.78 (0.1)	3.81 (0.18)	5.8 (0.18)	4.01 (0.15)	0.51 (0.09)	0.05 (0.01)	98.58
OLK21-036L3 (B)	LMx	Pumice	11	63.24 (0.89)	0.55 (0.02)	14.74 (0.26)	7 (0.25)	0.34 (0.15)	0.16 (0.02)	1.08 (0.02)	7.59 (0.13)	5.04 (0.12)	0.07 (0.04)	0.19 (0.01)	96.50
OLK21-036L4	LMx	Pumice	7	63.11 (1.01)	0.58 (0.07)	14.59 (0.44)	7.26 (0.82)	0.29 (0.16)	0.25 (0.09)	1.24 (0.39)	7.44 (0.26)	4.96 (0.16)	0.1 (0.07)	0.19 (0.03)	97.52
OLK21-036L5	LMx	Pumice	13	63.47 (0.98)	0.59 (0.03)	14.73 (0.25)	6.92 (0.47)	0.31 (0.19)	0.23 (0.05)	1.23 (0.2)	7.23 (0.5)	5.02 (0.12)	0.09 (0.06)	0.18 (0.02)	96.98
OLK21-036L6	LMx	Pumice	23	63.09 (0.79)	0.59 (0.04)	14.8 (0.28)	6.93 (0.5)	0.46 (0.34)	0.22 (0.05)	1.13 (0.08)	7.52 (0.21)	5.01 (0.11)	0.09 (0.05)	0.18 (0.02)	97.69
OLK21-036M	LAP	Pumice	25	63 (0.62)	0.51 (0.05)	13.2 (0.4)	8.36 (0.74)	0.35 (0.25)	0.09 (0.02)	0.83 (0.07)	8.66 (0.24)	4.6 (0.13)	0.05 (0.03)	0.34 (0.04)	98.47
OLK21-036N	LAP	Pumice	28	63.3 (0.62)	0.49 (0.03)	13.87 (0.24)	7.59 (0.47)	0.34 (0.21)	0.1 (0.02)	0.87 (0.04)	8.34 (0.24)	4.77 (0.07)	0.04 (0.04)	0.29 (0.03)	98.49
OLK21-036O1	LAP	Pumice	28	63.15 (0.54)	0.49 (0.03)	13.85 (0.23)	7.68 (0.45)	0.4 (0.34)	0.1 (0.02)	0.84 (0.04)	8.39 (0.29)	4.74 (0.08)	0.07 (0.06)	0.29 (0.02)	98.33
OLK21-036O2	LAP	Pumice	15	63.4 (0.81)	0.49 (0.03)	13.85 (0.15)	7.58 (0.29)	0.35 (0.26)	0.11 (0.01)	0.86 (0.05)	8.3 (0.22)	4.71 (0.1)	0.06 (0.05)	0.29 (0.02)	96.95
OLK21-036P	LAP	Pumice	19	63.41 (0.99)	0.51 (0.03)	14.17 (0.32)	7.32 (0.44)	0.33 (0.24)	0.12 (0.02)	0.95 (0.04)	8.03 (0.28)	4.85 (0.12)	0.04 (0.04)	0.26 (0.02)	96.89
OLK21-036Q1	LAP	Pumice	30	63.45 (0.63)	0.52 (0.03)	14.14 (0.22)	7.3 (0.33)	0.34 (0.19)	0.13 (0.02)	0.94 (0.06)	7.99 (0.28)	4.9 (0.13)	0.06 (0.05)	0.25 (0.03)	98.11
OLK21-036Q2	LAP	Pumice	21	63.52 (0.77)	0.52 (0.04)	14.1 (0.38)	7.32 (0.5)	0.32 (0.28)	0.12 (0.02)	0.93 (0.07)	8.05 (0.21)	4.83 (0.11)	0.05 (0.06)	0.25 (0.02)	98.01
OLK21-036R	LAP	Pumice	19	63.56 (1.1)	0.54 (0.04)	14.31 (0.42)	7.28 (0.63)	0.27 (0.13)	0.13 (0.02)	0.97 (0.07)	7.67 (0.53)	4.98 (0.17)	0.05 (0.06)	0.24 (0.02)	96.34
OLK21-036S	LAP	Pumice	18	63.37 (0.78)	0.51 (0.02)	14.39 (0.19)	7.2 (0.28)	0.31 (0.21)	0.12 (0.02)	0.96 (0.04)	7.94 (0.24)	4.91 (0.13)	0.05 (0.05)	0.23 (0.02)	96.88
OLK21-036U	LAP	Pumice	21	63.31 (0.91)	0.5 (0.04)	14.14 (0.33)	7.46 (0.37)	0.34 (0.18)	0.13 (0.03)	1.02 (0.05)	7.89 (0.24)	4.9 (0.14)	0.06 (0.05)	0.24 (0.02)	97.20
OLK21-036V	LAP	Pumice	19	63.34 (0.81)	0.49 (0.02)	14.04 (0.28)	7.56 (0.37)	0.38 (0.15)	0.12 (0.02)	0.99 (0.04)	7.85 (0.3)	4.92 (0.14)	0.07 (0.04)	0.24 (0.02)	97.63
OLK21-036W	LAP	Pumice	22	63.54 (0.8)	0.49 (0.02)	13.98 (0.18)	7.58 (0.29)	0.26 (0.16)	0.11 (0.02)	0.98 (0.04)	7.99 (0.26)	4.76 (0.16)	0.06 (0.06)	0.25 (0.02)	97.26

(*continued on next page*)

Table 3 (*continued*)

Sample	Unit	Deposit	N	SiO_2	TiO_2	Al_2O_3	FeO	MnO	MgO	CaO	Na_2O	K_2O	P_2O_5	Cl	Total
OLK21-036X	LAP	Pumice	19	63.55 (0.96)	0.48 (0.02)	13.68 (0.23)	7.96 (0.38)	0.3 (0.24)	0.07 (0.02)	0.89 (0.08)	7.97 (0.36)	4.78 (0.1)	0.05 (0.04)	0.27 (0.02)	97.95
OLK21-036Y	OFB	Pumice	19	74.47 (0.33)	0.15 (0.02)	10.6 (0.07)	3.79 (0.29)	0.16 (0.2)	0.01 (0.01)	0.05 (0.02)	5.93 (0.1)	4.34 (0.07)	0 (0.01)	0.49 (0.02)	93.77
OLK21-036Z	OFB	Pumice	14	74.38 (0.46)	0.15 (0.02)	10.61 (0.08)	3.83 (0.3)	0.1 (0.08)	0 (0.01)	0.05 (0.02)	5.82 (0.14)	4.52 (0.1)	0.02 (0.03)	0.51 (0.02)	93.41
OLK21-014	Ololbutot S	Obsidian	11	75.15 (0.46)	0.18 (0.02)	10.53 (0.08)	3.55 (0.16)	0.16 (0.26)	0.01 (0.01)	0.16 (0.13)	5.25 (0.06)	4.66 (0.19)	0 (0.01)	0.33 (0.01)	99.01
OLK21-037	Ololbutot N	Obsidian	8	76.14 (0.36)	0.12 (0.03)	11.43 (0.1)	2.22 (0.21)	0.08 (0.08)	0.01 (0.02)	0.12 (0.04)	4.42 (0.28)	5.14 (0.49)	0.03 (0.03)	0.29 (0.02)	95.77
OLK21-039	Ololbutot W	Obsidian	10	74.91 (0.88)	0.18 (0.02)	10.54 (0.08)	4.06 (0.28)	0.1 (0.14)	0.01 (0.01)	0.11 (0.02)	5.27 (0.19)	4.4 (0.16)	0.03 (0.05)	0.4 (0.01)	96.20
OLK21-040	Ololbutot N	Obsidian	10	75.33 (0.39)	0.17 (0.03)	10.65 (0.08)	3.54 (0.38)	0.15 (0.13)	0.01 (0.01)	0.14 (0.04)	5.09 (0.17)	4.56 (0.09)	0.02 (0.04)	0.34 (0.02)	99.12
OLK21-041	Gorge Farm	Obsidian	10	74.57 (0.54)	0.16 (0.02)	10.87 (0.11)	3.84 (0.3)	0.11 (0.15)	0.02 (0.01)	0.04 (0.02)	5.3 (0.14)	4.56 (0.12)	0.02 (0.04)	0.5 (0.02)	95.63
OLK21-044	Broad Acres	Obsidian	10	75.1 (0.61)	0.17 (0.02)	10.71 (0.13)	3.38 (0.32)	0.09 (0.15)	0.02 (0.02)	0.35 (0.29)	5.28 (0.14)	4.51 (0.09)	0.02 (0.04)	0.37 (0.02)	98.82

wt%) and Cl (0.49–0.53 wt%) contents. The Olkaria dome deposits (OD1, OD2 and OD3) are compositionally distinct from OP and OFB deposits. Specifically, the dome units display the highest SiO_2 (75.1–75.8 wt%) and CaO (0.12–0.19 wt%), and lowest FeO (3.1–3.6 wt %) and Cl (0.30–0.40 wt%) contents. All glass major elements show a transition in composition between the different units. Despite the large compositional overlap between OD1, OD2 and OD3, OD1 can be distinguished from the other dome units by having the highest Al_2O_3 (>10.6 wt%) and lowest Cl (<0.36 wt%) contents. Temporal changes in glass composition between the different Olkaria units are displayed in Fig. 9a, which highlights the clear distinction between early Olkaria (OP and OFB) and younger dome deposits (OD1–3).

The Maiella Pumice (MP) deposit (samples 028 in Fig. 8a-b) forms a separate rhyolitic group distinguishable from the comendite Olkaria pumice deposits. The MP glass is a pantellerite with an SiO_2 ranging 72.1–73.1 wt%. The MP could be not chemically correlated with any other tephra deposit within Olkaria, Longonot or another nearby pantelleritic centre (i.e., Eburru). The thin ash layer located within the MP beds (sample 024R in Fig. 8) falls on the comenditic trachyte–phonolite boundary (61.6 wt% SiO_2, 16.5 wt% Al_2O_3, 5.9 wt% FeO) and is offset from the compositional group of the Longonot trachytes.

The Longonot pumice deposits fall within four distinct groups. The main group, making up 98% of all Longonot tephra analysed, falls within a single cluster that extends across the comenditic trachyte and pantelleritic trachyte boundary (Fig. 8a). Within this larger group, the depositional units of the LAP, LA1 and LA2 show distinct chemical differences. The LAP covers the entire range of trachytes, but each fall deposit shows a suitable yet notable temporal evolution through the stratigraphy (Fig. 9b). From the basal LAP fallout deposit (036X) towards the upper–middle LAP deposit (036R), the glass becomes gradually depleted in FeO (from 8.0 to 7.3 wt%) and enriched in Al_2O_3 (from 13.7 to 14.4 wt%), yet the upper layers (036P–M) show a gradual increase in FeO (from 7.3 to 8.4 wt%) and depletion in Al_2O_3 (from 14.1 to 13.2 wt%) towards a pantelleritic trachyte. LA1 and LA2 are compositionally distinct from each other and form individual clusters at each end of the larger LAP trachyte group (Fig. 8b, Fig. 9b and Fig. 10b). LA1 is a comenditic trachyte with lower FeO (~7.5 wt%), whereas LA2 is a pantelleritic trachyte with higher FeO (~8.5 wt%). The single Longonot mixed deposit (LMx) that precedes LA1 and LA2 contains pumice clasts with compositionally different glasses extending from basaltic trachyandesite towards the main Longonot trachyte cluster (Fig. 8a and Fig. S2). Each sublayer (L1–6) has a distinct major element glass composition. The base (L1) contains two separate glass populations, a basaltic trachyandesite (51.9 wt% SiO_2) and a low-silica trachyandesite (55.3 wt% SiO_2). Pumice glass SiO_2 contents for L2 are similar to all other Longonot comenditic trachyte deposits, yet other major elements are distinct from the preceding upper LAP unit (e.g., higher Al_2O_3, lower FeO and Cl; Fig. 9b). Pumice clasts from L3 show high-silica trachyandesite glass composition between L1 and L2 (58.4 wt% SiO_2). Despite the TAS plot (Fig. 8a) showing L3 falling within a simple mixing trend between L1 and L2, other elements suggest this is not the case (Fig. S2). All pumice from L4–6 has a glass composition comparable to a typical Longonot comenditic trachyte from LAP and LA1.

4.2.2. PCA and k-means clustering of rhyolites

A principal component analysis (PCA) was performed on major element glass compositions for all rhyolitic pumice (i.e., Olkaria and Maiella Pumice deposits), using all EPMA data points to capture any heterogeneity within a single pumice sample (1329 data points), together with 171 different obsidian compositions from 12 different regions (Fig. 1c): 11 regions around Olkaria (Olkaria Hill, Ololbutot, Oserian, Broad Acres, Arcuate Domes, Kibikoni, Hell's Gate, Gorge Farm, Olenguruoni, Ndabibi, Ololerai) and several obsidians from the Eburru region (compiled from Marshall et al., 2009 and Brown et al., 2013). For the analysis, SiO_2, TiO_2, Al_2O_3, FeO, CaO, Na_2O, K_2O and Cl were all used, while MnO, MgO and P_2O_5 were omitted due to their low abundance and thus risk of overemphasising these elements during the cluster iteration (Fig. 11a).

Eigenvalues generated from the PCA, which represent the amount of total variance from the original dataset that is encapsulated within each principal component, show how the spread of the data can be fit into eight principal components (Fig. 11b). However, the majority of the variance in the glass compositions can be captured in the first three principal components: PC1 (56.8%), PC2 (22.3%) and PC3 (10.3%). Taking the main two principal components which encapsulate 79.1% of the entire dataset, PC1 can be described mostly by variations in SiO_2, TiO_2, Al_2O_3 and FeO, whereas PC2 is best described by variations in Cl, Na_2O, K_2O and CaO (Fig. 11a).

Cubic clustering criterion (CCC) for k-means clustering of the glass data reveals that 10 clusters are statistically optimal to separate the data. A spatial comparison of each cluster as a function of PC1, PC2 and PC3 demonstrates the compositional differences that can be made for the eruptive products (Fig. 11b). Mean compositional differences between each cluster is displayed in Fig. 11c, and the cluster assigned pumice and obsidians are given in Table 4. By identifying which pumice deposits and obsidian are assigned to the same cluster (Fig. 11d-g), it is possible to make a connection between pumice deposit and source vent location (Fig. 12). The only obsidian in the region to fall within the same compositional cluster as the Maiella Pumice is Ololerai (clusters 5 and 8), a region located outside the Olkaria complex on the western edge of Lake Naivasha. OP and OFB consistently fall within clusters populated by Gorge Farm obsidian (cluster 10). Owing to the larger compositional

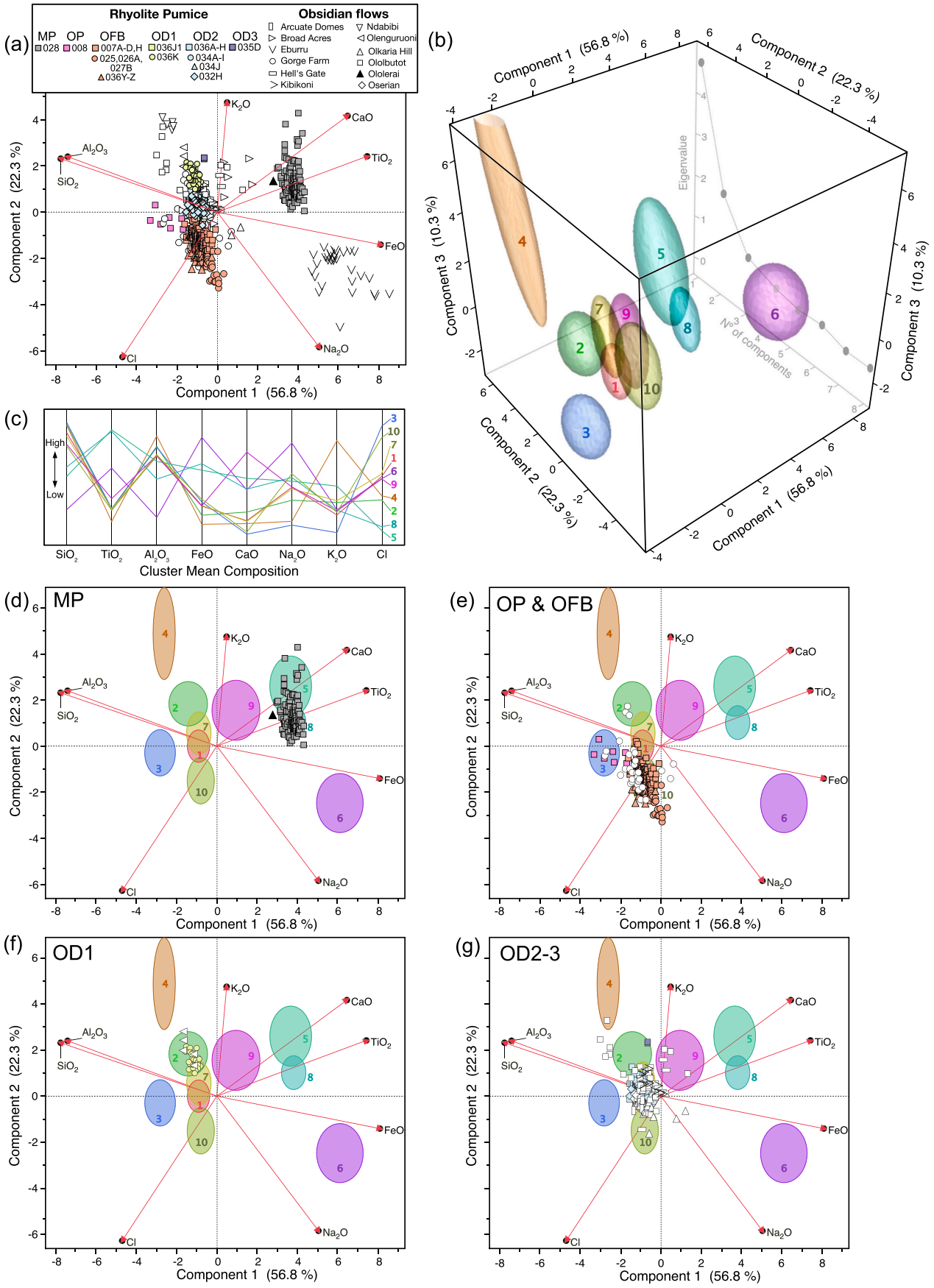

(caption on next page)

Fig. 11. Geochemical variability and clustering of Olkaria rhyolite pumice and obsidian lavas from Olkaria and Eburru. (a) Biplot derived from principal component analysis (PCA) of Olkaria rhyolite pumice and obsidian (data compiled from Marshall et al., 2009 and Brown et al., 2013). The biplot highlights the geochemical variability amongst the samples, with the spread in SiO_2, Al_2O_3, FeO and TiO_2 contributing mostly to the spread in principle component 1 (PC1) and Cl, K_2O, Na_2O and CaO contributing to the spread in principle component 2 (PC2). (b) 3D spatial visualisation of 10 distinct statistical clusters obtained by k-means clustering analysis, plotted as a function of the first three principal components (PC1, PC2 and PC3) obtained from the PCA, along with their corresponding eigenvalues. (c) Parallel coordinate plot providing a visualisation of the mean composition of the different clusters assigned to pumice and obsidian samples. The y-axis represents different scales for each specific compositional component, with each vertical scale normalised for each component to allow comparison across the different clusters. Biplots in (d-f) show the relationship between the eruptive units of Olkaria (MP (d), OP/OFB (e), OD1 (f) and OD2–3 (g)), obsidians and the k-means defined clusters, with each eruptive unit correlating to obsidians from a known vent source (e.g., Ololerai, Gorge Farm, Ololbutot) and each falling within unique cluster(s). (For interpretation of the references to colour in this figure legend, the reader is referred to the web version of this article.)

Table 4
Mean glass major element compositions (wt%) for the different rhyolite clusters obtained from k-means clustering (1σ deviation in brackets). Each described unit and associated deposits have been assigned to a cluster, along with obsidian from the different centres around Olkaria. N indicates the number of glass compositions that fall into that specific cluster.

Cluster	SiO_2	TiO_2	Al_2O_3	FeO	CaO	Na_2O	K_2O	Cl	N	Pumice Deposits	Unit	Obsidian
1	75.39 (0.4)	0.18 (0)	10.55 (0.1)	3.41 (0.3)	0.14 (0)	5.33 (0.2)	4.44 (0.1)	0.37 (0)	240	032H, 034A–H,J, 036C,D,F,G,H	OD2	Ololbutot, Olkaria Hill, Broad Acres, Oserian, Arcuate Domes, Kibikoni
2	75.97 (0.4)	0.17 (0)	10.96 (0.4)	2.82 (0.6)	0.2 (0.1)	4.89 (0.2)	4.63 (0.1)	0.28 (0)	65	036J1, 036K	OD1	Olenguruoni, Ndabibi, Gorge Farm
3	76.13 (0.4)	0.18 (0)	10.91 (0.1)	3.68 (0.5)	0.05 (0)	4.06 (0.3)	4.17 (0.1)	0.55 (0)	7	008C	OP	Gorge Farm
4	75.93 (0.2)	0.13 (0)	11.39 (0.1)	2.22 (0.2)	0.12 (0)	4.18 (0.3)	5.57 (0.3)	0.3 (0)	4	None	–	Ololbutot
5	72.2 (0.7)	0.43 (0)	10.34 (0.5)	5.75 (0.2)	0.43 (0.1)	5.53 (0.2)	4.88 (0.2)	0.17 (0)	21	028B,E,F,G,J	MP	Ololerai
6	69.78 (0.5)	0.31 (0)	8.03 (0.5)	7.88 (0.7)	0.35 (0.1)	6.81 (0.3)	4.52 (0.1)	0.36 (0.1)	32	None	–	Eburru
7	75.13 (0.4)	0.18 (0)	10.62 (0.1)	3.46 (0.3)	0.14 (0)	5.27 (0.1)	4.66 (0.1)	0.38 (0)	121	007D, 034A–H,J, 035D, 036C,D,F,G,H, 036J1	OFB, OD2 & OD3	Ololbutot, Olkaria Hill, Gorge Farm, Broad Acres, Hell's Gate, Kibikoni
8	72.88 (0.4)	0.43 (0)	9.61 (0.2)	6.17 (0.3)	0.36 (0)	5.66 (0.1)	4.52 (0.1)	0.18 (0)	92	028B,D,E,F,G,H,J	MP	None
9	74.54 (0.6)	0.21 (0.1)	10.58 (0.1)	3.42 (0.2)	0.62 (0.1)	5.34 (0.2)	4.5 (0.1)	0.36 (0)	7	None	–	Ololbutot, Broad Acres
10	74.42 (0.5)	0.17 (0)	10.6 (0.1)	3.86 (0.4)	0.06 (0)	5.78 (0.3)	4.48 (0.1)	0.51 (0)	195	007A,C,D,H, 008C, 25C, 026A, 027B, 036Y–Z	OP & OFB	Gorge Farm

overlap of the Olkaria domes units and Olkaria obsidians, it makes correlating pumice and obsidian more challenging. However, the only pumice linked to cluster 2 was OD1, which also contains obsidian from Olenguruoni and Ndabibi, suggesting the NW of Olkaria was volcanically active during OD1. OD2 deposits are found in both cluster 2 and 7. Both these clusters also contain obsidian from the Arcuate domes, Ololbutot, Olkaria Hill and Broad Acres, which is consistent with these deposits being very proximal to the vents. The OD3 PDC deposit (035D) falls within the same cluster as obsidians from Ololbutot, specifically the young Ololbutot obsidian flow (191 ± 23 cal yr BP), suggesting Ololbutot has been the site of recent volcanic activity at Olkaria with evidence of both effusive and explosive eruption styles.

4.3. Eruptive volumes and magnitude

Eruption volumes for three major fall deposits were estimated by manually constructing isopach maps. Owing to the Olkaria dome deposits (OD1–3) only being exposed in proximal locations within the centre of Olkaria, an accurate estimation of their volume was not possible. The fall deposits that were selected were identified in multiple locations around the Olkaria and Longonot field area, although insufficient exposures outside this area meant inferences on isopach positions were required. Based on this, an elliptical isopach geometry was assumed to provide the best volume approximation. Minimum bulk deposit volumes were calculated from two LAP deposits, one from the bottom of the sequence and one from the top, and an OFB deposit (Fig. 13a-c). The vent location for LAP deposits was assigned as Longonot summit crater, although this was unlikely the true vent as it was later infilled by more recent lavas and pyroclastics (LA1 and LA2), and for OFB a vent in the centre of Gorge Farm.

Using these isopach maps, the exponential thinning method of Pyle (1989) was applied to obtain the minimum deposit volume. The bulk volume estimation of the basal LAP deposit is 1.63 km^3, for the upper LAP deposit 0.59 km^3, and for the OBF deposit 0.20 km^3. Although the componentry of these deposits showed the presence of lithics and hydrothermally altered clasts in the 0.5 mm size fraction, the mean grain size of both LAP deposits is ~5 mm, and for OFB pumice ~4 mm, of which pumice was the only clast type above these grain sizes. As a result, we only considered the pumice when converting the bulk deposit volume to a dense rock equivalent (DRE) volume, by assuming 2300 kg/m^3 rhyolite melt density (Fierstein and Hildreth, 1992) and 500 kg/m^3 average bulk density typical for peralkaline rhyolite pumice fall deposits (e.g., Tadesse et al., 2022). The DRE volume for the basal LAP deposit is estimated at 0.35 km^3, upper LAP deposit at 0.13 km^3, and OFB deposit at 0.04 km^3. These estimates were then used to calculate a minimum magnitude for each eruption as per Pyle (2015). The earlier LAP eruption had a minimum estimated magnitude of 4.9, while the later LAP eruption had an estimated magnitude of 4.5, and the OFB eruption is estimated to have a minimum magnitude of 4.0.

5. Discussion

5.1. Eruptive history, correlation and timing

Both Olkaria and Longonot have a long, interspersed eruptive history spanning 0.45 Ma. The earliest volcanic activity is recorded by primitive

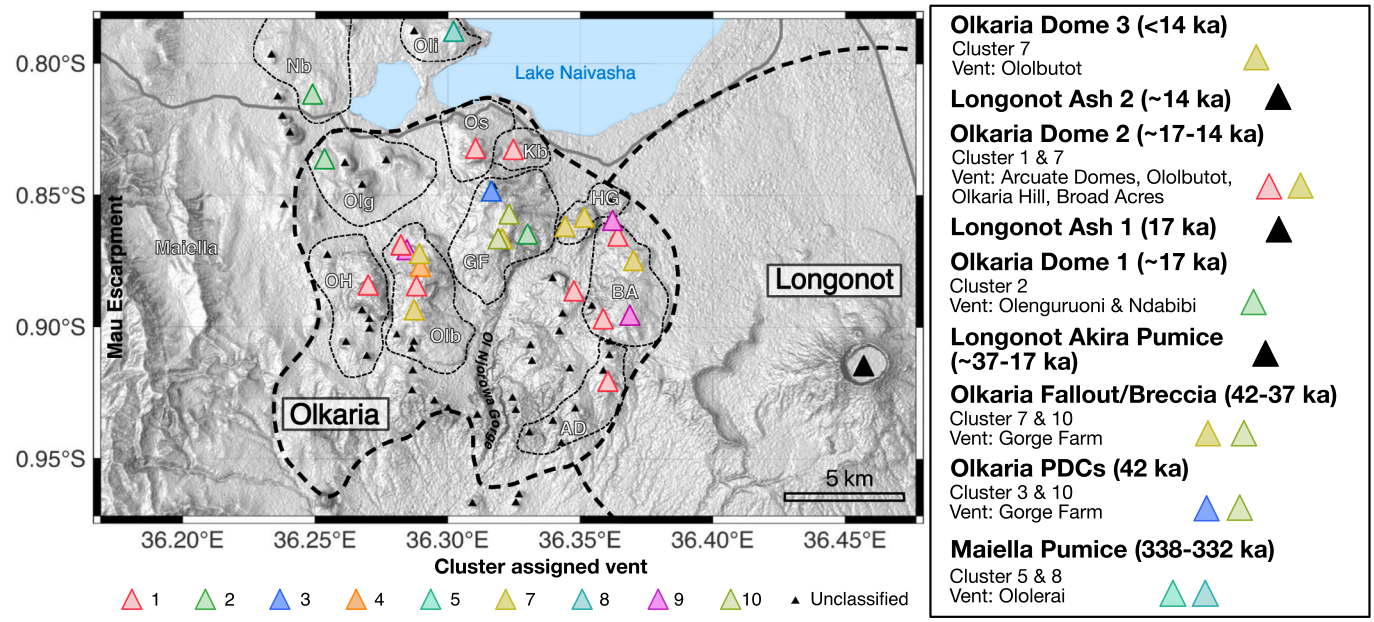

Fig. 12. Spatial distribution of compositionally distinct clusters within the Olkaria Volcanic Complex and their implications for pumice provenance. The map displays the vents of the Olkaria Volcanic Complex, colour-coded according to the clusters identified through k-means clustering analysis of glass major element compositions. The spatial distribution of these compositionally distinct clusters enables the inference of pumice source location based on the geochemical similarities between the pumice and obsidian from specific locations within the Olkaria region. (For interpretation of the references to colour in this figure legend, the reader is referred to the web version of this article.)

basalt lavas of the Ndabibi Basalt Formation exposed north of Olkaria, which have been faulted and dissected, indicating eruption during early rifting prior to more evolved central volcano development (Fig. 14a; Clarke et al., 1990). Shortly after, more alkaline basalt magmas similar to modern rift floor lavas were being erupted, marked by less dissected cones of the Akira Basalt Formation (Clarke et al., 1990). Crustal contamination revealed by multiple isotopic signatures in these mafic lavas indicate interaction with ancient enriched lithospheric mantle as well as lower crustal amphibolite material during ascent (Davies and Macdonald, 1987).

Development of the peralkaline silicic central volcanoes initiated with the first known explosive eruptions in the region associated with the widespread Maiella Pumice deposits erupted between 338 ka and 333 ka (Fig. 14b). These large rhyolitic eruptive events predate all other exposed deposits at Olkaria and Longonot and likely represent inception of pantelleritic magmatism. The vent location was previously assumed to be somewhere within Olkaria (Clarke et al., 1990), but k-means clustering analysis shows it correlates strongly to a region outside the present-day complex on the western edge of present-day Lake Naivasha (Fig. 11d and Fig. 12). These obsidians were previously mapped by Clarke et al. (1990), termed the Ndabibi Pantellerite Formation, and suggested they underly both the Longonot Akira Pumice and the oldest Olkaria deposits (welded pantelleritic ignimbrite, O1) found only at the base of the Ol Njorowa gorge, supporting their correlation with the Maiella Pumice. This area was likely the first manifestation of one of the central volcanoes in the region. The comenditic trachyte ash layers separating some of the Maiella Pumice deposits show a distinct glass composition relative to the <40 ka Longonot trachytes (lower SiO_2 and FeO, higher Al_2O_3), suggesting these distal ash layers reflect early explosive phases at Longonot (pre-caldera collapse) during the growth of the trachytic shield volcano (Scott, 1980).

The oldest deposits studied within Olkaria are associated with explosive comenditic volcanism at 42 ka, generating extensive lithic-rich PDCs that deposited the >20-m-thick OP unit proximal to the Gorge Farm vents (Fig. 14c). This marks the earliest confirmed activity within the present day Olkaria complex, which likely excavated precursor domes and remobilised older lavas, contributing to the comenditic rhyolites that proceeded. This included a series of pyroclastic fall beds interbedded with volcanic ash layers recording explosive dome collapse events and unsteady ash plumes associated with a new dome building phase, producing the OFB deposits from Gorge Farm between 41 ka and 37 ka. Layers of accretionary lapilli at the base of the OFB deposits suggest phreatomagmatic activity was a precursor to the more explosive phases, estimated at magnitude ~4 (Fig. 13c). Recently analysed lake cores from Lake Victoria contained tephra layers originating from Olkaria ~300 km away, revealing four >15 ka layers matching Olkaria comendites (Lane et al., 2018). These cryptotephras correlate compositionally with early Gorge Farm eruptive products, while a >49 ka rhyolitic ash tuff on the east shore of Lake Victoria also matches the timing and chemistry of OP and OFB Gorge Farm deposits (Blegen et al., 2015), demonstrating early Olkaria explosions can be traced to even greater distal locations.

Concurrent with early development of Olkaria Gorge Farm activity, the main Longonot cone initiated its growth between 37 ka and 17 ka (Fig. 14c). A sequence of thick, widespread pumice lapilli beds (LAP) represents a major explosive phase (eruption magnitudes between 4 and 5; Fig. 13a-b), that dispersed pumice across Olkaria. Multiple fall units bounded by palaeosols indicate separate eruptive episodes from the same vent source over a ~20 ka period. The subtle change in glass composition to less evolved trachyte (Fig. 9b) suggests a zoned and gradually depleting magma source beneath Longonot through time. Longonot Akira Pumice was previously dated at 9.1 ka from ^{14}C of palaeosol horizons (within unit Lp5 in Clarke et al., 1990). However, previous findings of ^{14}C dating of soils have revealed they can produce inaccurate dates, with reported discrepancies of more than several thousand years (Orlova and Panychev, 1993). It is suggested that if deposits accumulated relatively slowly and/or the soil system remained open for a long period, it could permit continuous fresh carbon contamination, consequently changing the ^{14}C content of the organic soil matter causing a significant age underestimation (Wang et al., 1996). Thus, it is common that measured ^{14}C ages of soil organic matter are significantly younger than the true age of the soil (e.g., Hass and Dalbey, 1991; Tornqvist et al., 1991; Orlova and Panychev, 1993; Martin and Johnson, 1995). The LAP eruptions were immediately

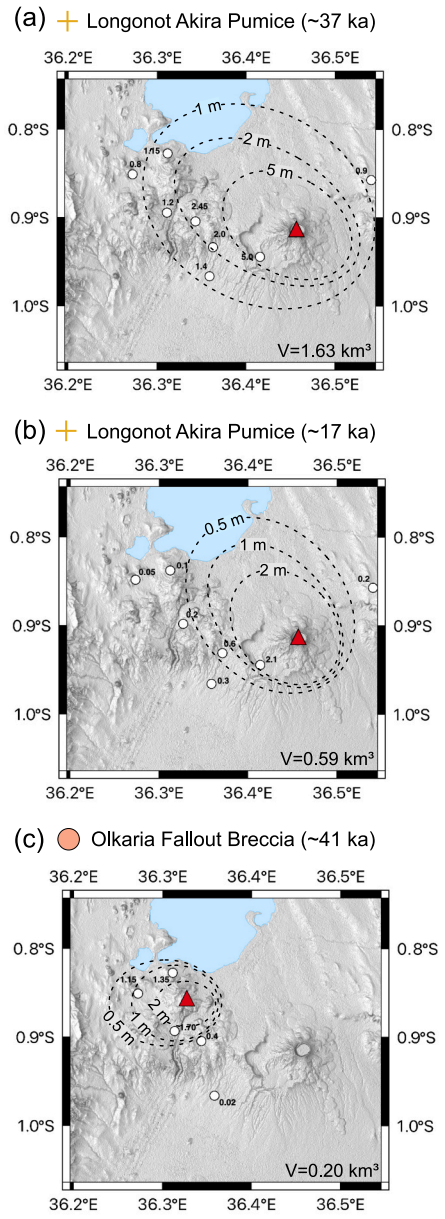

Fig. 13. Isopach maps (contours in metres) and volume estimates for three major fall deposits in the Olkaria and Longonot region. (a) ~37 ka Longonot Akira Pumice; (b) ~17 ka Longonot Akira Pumice; (c) Olkaria Fallout Breccia deposit from Gorge Farm. Minimum bulk deposit volume, calculated using the method of Pyle (1989), is indicated on the figure. In each map, the source vent is marked by a red triangle. For the Olkaria fall deposits (c), the source vent (i.e., Gorge Farm) was identified using k-means clustering of glass major element compositions. The use of dashed isopach lines is used to highlight the uncertainty in the shape of the contours, which arises from limited exposure of the deposits.

followed by the eruption of chemically mixed pumice (LMx) at ~17 ka (Fig. 14d). Detailed sampling of the deposit suggests an intrusion of a basaltic trachyandesite led to its eruption. The observation of basaltic trachyandesite pumice erupting first followed by trachyte and then a trachyandesite composition suggests the basaltic trachyandesite initially ascended and erupted without interaction with Longonot's trachyte magmatic reservoir, but destabilised the latter reservoir (left over from the LAP eruptions) causing trachyte to erupt independently. Further intrusion of basaltic magma from beneath likely mixed with the erupting trachyte resulting in the trachyandesite composition. The basaltic trachyandesite was likely low volume as only trachyte pumice erupted at the end of the LMx phase. Evidence of this basaltic input was previously only observed in the mixed hawaiite–trachyte lavas (Scott and Bailey, 1984), but the LMx pumice unit reveals clearer depiction of this process erupting after the LAP.

From 17 ka, the focus of activity at Olkaria shifted to renewed explosive volcanism erupting the OD1 deposits from vents in the NW of the complex (Olenguruoni and Ndabibi), characterised by interbedded fine ash and coarse pumice lapilli beds (Fig. 14d). Significant proportions of obsidian and lava lithics record ongoing dome growth interrupted by small–moderate vulcanian-style explosions related to episodic dome destruction events. Shortly after, ash eruptions from Longonot generated thick widespread ash layers represented by the LA1 deposit dated at 16.9 ka. The glass composition of LA1 pumice matches the trachyte pumice from the upper LMx unit. From 17 ka to 14 ka, Olkaria volcanism transitioned back to dome building concentrated at the arcuate ring fracture, marking the southern boundary of Olkaria (Fig. 14e), and other central vents such as Ololbutot and Olkaria Hill (OD2). This emplaced a sequence of lithic-rich BAF deposits interspersed with ash beds recording multiple dome collapse events and unsteady ash plumes. Despite previous studies correlating the presence of the domes along the ring fracture to a caldera-forming event at Olkaria (e.g., Clarke et al., 1990), no conclusive field evidence (such as ignimbrite sequences or thick lag breccias) was found across Olkaria or even while traversing the Ol Njorowa gorge. If a caldera-forming eruption did take place (pre-OFB and OP phase), it has likely been buried by the thick post-caldera deposits of Olkaria domes and Longonot over the past ~42 ka.

After 14 ka, more explosive ash eruptions persisted at Longonot to generate LA2 beds, reflecting ongoing ash venting and crater excavation (Fig. 14f). Similarly to previous age constraints on the LAP beds, the ^{14}C date from a palaeosol horizon has largely underestimated the timing of LA2 (<3.5 ka; unit L8 in Clarke et al., 1990). The most recent eruptions at Olkaria occurred in the Ololbutot centre associated with a N–S fissure, marked by extrusion of the young obsidian lava flow ~191 cal yr BP which was accompanied by BAFs from collapse of active domes and PDCs from intermittent explosive activity (Fig. 14f). Ongoing intense fumarolic degassing at Ololbutot suggests renewed explosions or future dome growth remains likely, representing continued hazards (e.g., Cappelli et al., 2023).

The concept of distinct eruptive centres within Olkaria (Black et al., 1997; Heumann and Davies, 2002; Macdonald et al., 2008; Marshall et al., 2009) is confirmed here and clarifies the spatial and temporal relationships between different eruptive units. The previous eruptive framework from Clarke et al. (1990) provided a general context, but did not fully capture the timing of the earlier explosive pre-Olkaria history that included the Maiella Pumice eruptions and initial explosive phases at Olkaria (OP and OFB). Additionally, the ages previously assigned to the Lower (O2; ~20 ka), Middle (O3; ~8 ka) and Upper (O4; ~6 ka) Comendite Members do not correlate with OP (42 ka), OFB (41–37 ka), and OD1–3 (<17 ka) units described here. Comparing the preliminary work on the pyroclastic deposits by Clarke et al. (1990) we can correlate OP and OFB units to the Lower–Middle Comendite Formation (O2–O3), and OD1–2 to the Upper Comendite Formation (O4). A discrepancy in these ages has implications on subsequent work on timescales of magma storage in the crust (Black et al., 1997; Heumann and Davies, 2002; Rogers et al., 2004). Estimates of the longevity of the Olkaria magmatic system from isotopic disequilibria data align well with our $^{40}Ar/^{39}Ar$ eruption ages used to define the different eruptive phases. U–Th isochrons from a Gorge Farm lava indicate a fractionation event at 24 ±1 ka, consistent with a Rb–Sr defined fractionation age of 22 ± 4 ka, although one sample using fayalite-glass suggested an earlier fractionation age of 47 ± 0.2 ka (Heumann and Davies, 2002). This is further supported by the U–Th ages of Gorge Farm lavas obtained by Black et al. (1997) of between 14.6 ± 2 ka and 36.2 ± 2 ka, which match the eruption ages of the OP and OFB units at Gorge Farm. For lavas from the Ololbutot centre, Rb–Sr isochron ages suggest fractionations events at 50 ± 15 ka and ~ 12 ± 5 ka, the latter falling within the eruption age

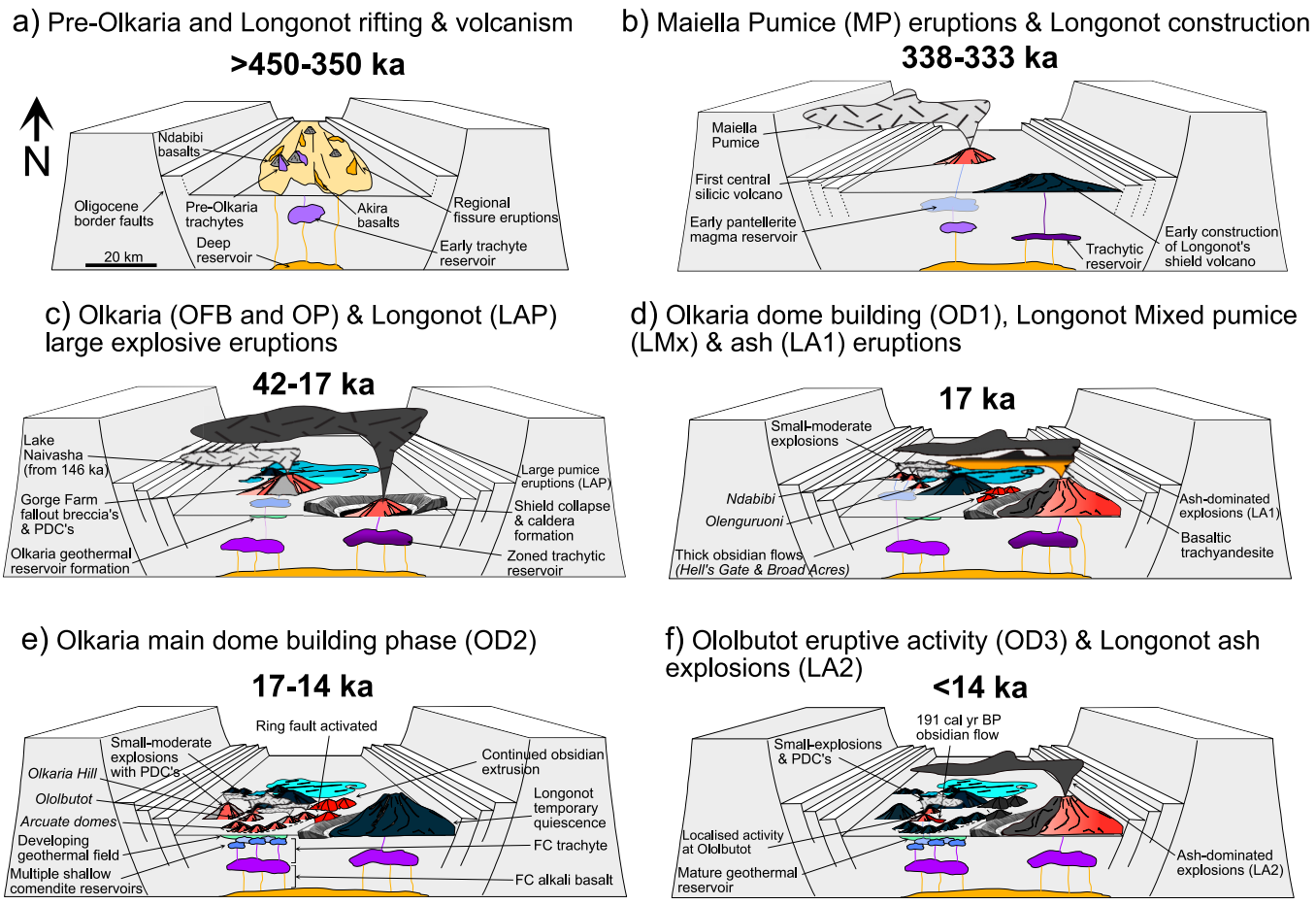

Fig. 14. Schematic diagrams depicting the temporal and spatial evolution of the Olkaria Volcanic Complex and Longonot in the Southern Kenya Rift based on the tephrostratigraphy and explosive phases identified in this study and as described in the text.

range of the OD2 unit. From these ages, it is suggested the earliest magmatic fractionation event took place ~50 ka, which fits reasonably well with the onset of the oldest Olkaria eruptions at Gorge Farm (41–37 ka), followed by another major fractionation event at ~24 ka corresponding to renewed dome activity at ~17 ka. Thus, Olkaria magmas likely experienced protracted residence times (7–10 kyrs) prior to eruption, contrasting to the previous estimate of 22 kyrs based on the ^{14}C palaeosol ages. The timescale of the Longonot magmatic system has also been investigated (Rogers et al., 2004), which reveals a Th–Ra fractionation event at >8 ka (Rogers et al., 2004), consistent with the eruption age for the LA2 deposits (<14 ka), implying magma storage timescales are significantly shorter than at Olkaria.

The integrated eruptive histories of the two systems reveal cycles of intermittent explosive eruptions at Longonot punctuated by periods of active Olkaria lava dome construction and destruction, reflecting an alternation in activity between the two developing peralkaline centres (Fig. 14). Several lines of evidence suggest both Olkaria and Longonot may have experienced interlinked eruptive activity over time, such as Longonot pumice clasts from LA1 found within fall deposits of Olkaria's OD1 unit and the lack of palaeosols separating the LAP and OFB pumice fall beds. This field-based evidence is consistent with the work of Scott and Skilling (1999) who suggest synchronous eruptive activity between Longonot and Suswa owing to tectonic stresses facilitating magma movement along regional faults. It is thus likely the volcanic activity of these systems are regulated by a combination of volcanic (local) and tectonic (regional) perturbations. Furthermore, petrological and geophysical evidence indicate the longevity of the systems has been maintained by continuous inputs of heat and material from hotter, more mafic alkaline magmas at depth (e.g., Scott and Bailey, 1984; Marshall et al., 2009; Biggs et al., 2009). Structural analyses reveal alignments of volcanic vents and fractures parallel to regional rift faults, supporting a strong structural control (Wamalwa et al., 2016; Shi et al., 2021; Omollo et al., 2022). Early work by McConnell (1972) described N–S and NE–SW fault swarms meeting near Olkaria, and later Scott (1980) mapped NW and NNE fractures controlling zones of weakness for younger Longonot activity. Geophysical modelling and volatile flux measurements show that dilational zones at fault intersections control magmatic fluid pathways (Omenda, 1998; Robertson et al., 2016; Omollo et al., 2022; Cappelli et al., 2023). Thus, the evidence indicates regional tectonics have a significant influence on volcanism by providing pathways for magma transport from mantle sources to crustal reservoirs and eruption centres at the surface.

5.2. *Eruptive frequency*

Providing an estimate of the explosive eruptive frequency and thus repose timescales for Quaternary volcanic centres in the EARS has proved a challenge owing to the paucity of well constrained ages of many systems (Biggs et al., 2021). Using the established tephrostratigraphic framework (Fig. 2) it is possible to estimate an average eruptive frequency for three of the units described in section 4.1 (MP, LAP and OD2). The Maiella Pumice unit consists of at least 13 pronounced pumice fall beds that were emplaced between 338 ka and 333 ka. The lack of exposure of the MP in the central portion of the rift, owing to coverage by younger pyroclastic deposits from Olkaria and Longonot, means smaller explosive eruptions that were not detected on the western rift margins (i.e., locations 024 and 028) cannot be ruled out. However, a minimum average of at least one large explosive eruption occurred per

400 years. If the Ololerai centre on the edge of present-day Lake Naivasha is assumed to be the source, then the medial distances (~13 km west) exposing pumice beds up to 1.5 m thick suggests a similar volume and magnitude, or possibly larger, to an early eruption of Longonot Akira Pumice (i.e., magnitude ~5).

For the LAP, at least 11 pumice fall deposits erupted between 37 ka and 17 ka. These eruptions were high magnitude (>4.5), dispersing pumice across Olkaria, on an average of one eruption per 2000 years. The general reduction in both deposit and palaeosol thickness towards the top of the LAP unit, suggests these explosive eruptions became more frequent but of lower magnitude with time. The OD2 deposits have a well-constrained eruptive age of between 17 ka and 14 ka. More than 40 individual events can be counted within this phase in the form of fallouts and PDCs including BAFs. A minimum average frequency of this dome-building phase is at least one small–moderate explosion (magnitude <3) or collapse event per 100 years (likely interspersed by many smaller events), an estimate consistent with the repetitive nature of a system hosting an active dome (e.g., Luhr and Carmichael, 1980). The lack of preservation of many of the deposits, particularly smaller eruptions (Brown et al., 2013), and likely alternating dispersal patterns mean these eruptive frequency-magnitude estimates are a minimum (e.g., Bonadonna and Houghton, 2005). It is also important to note that these estimates of eruptive frequency do not include the many individual rhyolitic and trachytic lavas erupted across the area, which constitute a significant volume of the eruptive products for both Olkaria (~13 km^3; Clarke et al., 1990) and Longonot (~156 km^3; Scott, 1980). Unfortunately, few studies exist on eruption frequency-magnitude relationships on other volcanoes in the EARS, but those that do exist come primarily from the MER. Eruptive frequencies of the peralkaline rhyolitic complex Bora-Baricha-Tullu Moye based on field stratigraphy estimated one moderate–large (magnitude 4–5) explosive eruption per 3000–4000 years (Tadesse et al., 2022). At Corbetti volcano, combined terrestrial and lacustrine records provide an estimate of one large explosive eruption (magnitude >4) every 300–400 years (Colby et al., 2022), while at Aluto one moderate eruption (magnitude 3–4) every ~300–400 years since 10 ka (Fontijn et al., 2018; McNamara et al., 2018). In the trachytic Rungwe Volcanic Province, located in Tanzania at the north of the Malawi Rift, several explosive eruptions since 4 ka were recorded in the stratigraphic record for the most recently active Rungwe volcano providing an estimated frequency of one eruption every 500 years (Fontijn et al., 2010). Thus, the eruptive frequencies of Olkaria and Longonot are consistent with other systems located to the north in Ethiopia and south in Tanzania (i.e., one every 500–1000 years).

5.3. Geochemical variability

Olkaria hosts rhyolitic lava domes, flows and pyroclastics displaying a wide range of glass compositions despite its relatively small geographic footprint (Fig. 10). Various studies have identified distinct compositional groups amongst the comendites found across different eruptive phases (Davies and Macdonald, 1987; Macdonald et al., 2008; Marshall et al., 2009), which is demonstrated in section 4.2.2 by using statistical clustering of major elements. Tracing units back to common parental magmas and unravelling Olkaria's subsurface plumbing system remains an ongoing challenge (e.g., Macdonald et al., 2008; Marshall et al., 2009). However, several lines of evidence suggest variable crustal source contributions from partial melts, fractional crystallisation and magma mixing processes have likely all operated to generate discrete batches of compositionally diverse rhyolitic magmas stored in small, isolated reservoirs beneath the complex ~50 ka (e.g., Heumann and Davies, 2002; Macdonald et al., 2008; Marshall et al., 2009).

Major element glass compositions reveal seven compositional clusters (clusters 1, 2, 3, 4, 7, 9 and 10; Fig. 11d-g) for the Olkaria comendites that cluster into groups predominantly erupting from different geographic centres across the complex through time, such as the ~42 ka Gorge Farm and more recent Ololbutot centre in agreement with Marshall et al. (2009). This suggests physical separation of small magma batches into isolated storage regions rather than a single large reservoir. Previous geochemical studies on the rhyolitic lavas suggest several processes are likely responsible for the formation of Olkaria comendites. Early petrological experiments revealed that closed-system fractional crystallisation of observed phenocryst assemblages cannot adequately explain major element trends observed (Macdonald et al., 1987) and that crustal assimilation signatures in early basalts also require open-system processes during differentiation (Davies and Macdonald, 1987). Radiogenic isotopes confirm the rhyolites predominantly represent crustal melts rather than pure fractionation products of the basalts (Davies and Macdonald, 1987; Marshall et al., 2009). It was suggested that remelting of basement lithologies (e.g., syenites), which are identified as xenoliths in the rhyolites, could generate the evolved melts while explaining unusual trace element signatures (Macdonald et al., 1987). However, generating the comendites would require additional processes since partial melting of crustal material does not easily explain the generally low CaO and high FeO, alkalis, and incompatible elements such as Zr and Nb (Bailey and Macdonald, 1987; Macdonald et al., 1987; Marshall et al., 2009). Extensive evidence suggests fluxing of the lower crust by exsolved magmatic volatiles including halogens could promote partial melting by lowering the solidus (Wilding et al., 1993; Black et al., 1997; Marshall et al., 1998; Macdonald et al., 2008). Abundant exsolved magmatic volatiles are evidenced by extensive fumarolic alteration zones proximal to eruptive centres (e.g., Ololbutot; Clarke et al., 1990; Cappelli et al., 2023). This could contribute to the variable Cl contents measured in glasses from the different eruptive units (Fig. 9a). The earlier OP and associated OFB deposits have uniformly high Cl contents, while the younger dome-forming units show a bifurcation into high and low Cl groups. This also shows that the larger explosive eruptions from the Gorge Farm centre consistently produce Cl-rich glasses relative to the smaller dome eruptions. However, the specific mechanism controlling Cl variability across Olkaria remains uncertain.

Magma mixing adds a further complexity, as evidenced by disequilibrium textures and mineral compositions plus quenched mafic inclusions in Olkaria comenditic lavas suggesting extensive mingling prior to eruption (Macdonald et al., 2008; Marshall et al., 2009). Such mixing is typically attributed to recharge events, which would sustain the longevity of the Olkaria magmatic reservoirs. Physical separation of these isolated magma pockets would permit subtle differences in fractionation paths and also crustal melt contributions, but the estimated short residence times (<8 kyr) may limit homogenisation (e.g., Heumann and Davies, 2002). Consequently, the chemical diversity of the different magma clusters at Olkaria likely reflects structure of the underlying reservoirs which would impact the accessible crustal sources (halogen fluxing) along with minor mixing events.

At Longonot, variations in the trachyte lava compositions over time was previously reported by Scott and Bailey (1984). Similar chemical trends were identified in the pumice glass compositions (Fig. 8b). The compositional range from comenditic trachyte to pantelleritic trachyte is consistent with extended fractional crystallisation dominated by alkali feldspar removal (Scott and Bailey, 1984; Rogers et al., 2004). Despite the apparent closed-system fractional crystallisation trends of the trachytes, it is proposed that at least two separate reservoirs beneath Longonot exist, based on evidence that some lavas do not sit on the same fractional crystallisation trend. This is supported by the LMx unit which erupted basaltic trachyandesites, trachyandesites and comenditic trachytes, with the trachytes not falling along a single mixing line with the basaltic trachyandesites and trachyandesites. These two mafic compositions recorded in the LMx pumice thus likely represent a separate batch of magma, unconnected to the main trachyte reservoir. As suggested by the chemical diversity observed in the lavas (Scott and Bailey, 1984), small, isolated trachyte magma batches may also exist beneath Longonot. Yet despite proximity to Olkaria, isotopic data suggests Longonot derived trachytes come from a separate source experiencing different fractional crystallisation timescales (Rogers et al., 2004).

5.4. Hazard implications

Central rift volcanoes in the SKR, like Olkaria and Longonot, have been active throughout the Quaternary and have the potential to pose significant volcanic hazards in the future based on their eruptive histories. Major rhyolitic explosive eruptions initiated in the region around 340 ka, with further explosive activity from Olkaria and Longonot since 40 ka, and more recent lava extrusion and dome growth throughout the Holocene (Clarke et al., 1990; Marshall et al., 2009). The most recent eruptions of both volcanoes occurred less than 250 years ago. The variety of past eruption styles at both Olkaria and Longonot create substantial risk of future hazardous volcanic events. Monitoring of unrest and contingency plans for different eruption scenarios are vital for mitigating regional impacts on infrastructure, agriculture, wildlife tourism and the significant geothermal development at Olkaria (Omenda, 1998). Although ground deformation (Biggs et al., 2009; Albino and Biggs, 2021) and CO_2 degassing surveys (Robertson et al., 2016; Cappelli et al., 2023) show these systems are still active, they typically experience long repose periods on the order of several hundred to thousands of years. This hampers eruption forecasting and hazard awareness, despite the close proximity of major urban centres such as Nakuru, Naivasha and Nairobi, all located within 60 km (Fig. 1b). The populations most vulnerable to direct hazards reside within 30 km of Olkaria and Longonot, >200,000 people based on current demographic estimates (Global Volcanism Program, 2023), with locally dense rural farming settlements around Naivasha Town (10–15 km to the north) and Maasai communities residing around Olkaria being amongst the most exposed.

For many of the volcanoes in the EARS, significant knowledge gaps exist regarding the timing and frequencies of volcanic eruptions. Most existing dates rely on limited radiocarbon analyses with large uncertainties, thus better constraints on eruption timing and magnitudes are needed to forecast future activity. The early eruptive episodes at Olkaria and Longonot included large explosive phases of activity (OP, OFB and LAP) which formed thick, widespread pyroclastic deposits. Such activity today would pose considerable threats to developments in the area. The dominant hazard posed by probable future activity at Olkaria would likely be related to disruption and collapse of active lava domes and flows (e.g., Ololbutot). Based on the distribution of recent BAF deposits, these hazards would mostly threaten geothermal facilities and agricultural lands immediately adjacent to the domes, although ash fall could impact wider areas depending on plume heights and wind patterns. Even a small volume event like the ~191 cal yr BP Ololbutot eruptions would have localised impacts on terrain, vegetation and sediment loading into lakes. With the extensive development of the geothermal power stations at Olkaria, a similar eruption today would cause significant economic damage. In particular, ongoing degassing behaviour at Ololbutot suggests the subsurface magmatic system remains active and could lead to renewed dome activity. Additionally, with Olkaria hosting a large, active hydrothermal reservoir, hydrothermal explosions are possible owing to the rapid release of pressurised fluids held within subsurface fractures (occurring with little to no precursory warning). Hazard footprints would depend on explosion magnitudes but could generate PDCs across several kilometres, produce ballistic blocks and induce secondary hazards like landslides or wildfires across broader sectors of the complex. The results from this study could serve as a foundation for additional research aimed at developing more comprehensive volcanic hazard assessments, perhaps even including probability estimates (e.g., Clarke et al., 2020; Tierz et al., 2020), or volcanic monitoring efforts in light of possible future hazards.

6. Conclusion

Construction of a detailed tephrostratigraphic framework has provided new insights into the timing, magnitude and evolution of the Olkaria and Longonot volcanic complexes in a poorly known sector of the EARS through detailed field investigations, geochemistry and geochronology of preserved pyroclastic deposits. The results reveal a long history of peralkaline rhyolitic and trachytic volcanism initiated in the region at least ~340 ka. Stratigraphic reconstructions identified 10 discrete pyroclastic units recording major explosive phases related to separate vents. The earliest preserved deposits are pantelleritic rhyolitic pumice fall beds of the regional Maiella Pumice (1), $^{40}Ar/^{39}Ar$ dated ~338–333 ka, representing the onset of peralkaline silicic volcanism in the SKR. This preceded more proximal deposits associated with Gorge Farm PDC (2) and fall deposits (3) dated at ~42–37 ka. Overlapping with Olkaria's Gorge Farm activity, Longonot experienced at least 13 large explosive eruptions recorded by the comenditic trachyte to pantelleritic trachyte fall deposits from ~37 ka to 17 ka (4), which culminated with compositionally mixed magma eruptions (5). Longonot ash eruptions (7) persisted from ~17 ka marking a change to less explosive eruptive behaviour. Contemporaneously, dome-building eruptions at Olkaria and subsequent collapse events dominated from 17 ka to 14 ka based on repetitive proximal BAF and fall deposits (6 and 8). Younger trachytic ash deposits at Longonot (<14 ka) proceeded and likely continued throughout the Holocene (9), while Olkaria activity concentrated towards the centre of the complex (10) in the form of lava extrusion and small interspersed explosions at Ololbutot (191 ± 23 cal yr BP).

Compositional variations in pumice glass revealed distinct geochemical clusters for Olkaria rhyolites, Longonot trachytes and older Maiella Pumice pantellerites. PCA statistical analysis correlated Olkaria deposits to specific dome regions using obsidian flows, which allowed vent locations of different eruptive units to be determined allowing us to track the migration of active regions of the complex and shifts in eruptive style over time. Eruption magnitudes estimated from isopach mapping of widespread fall units range from 4 to 5, producing individual eruption volumes up to 1.6 km^3. These represent significant regional hazards, with dispersed pumice fallout accompanied by PDCs extending >20 km from source vents. Ongoing CO_2 emissions and evidence for recent explosive activity indicates future eruptions remain a threat at both Olkaria and Longonot. The juxtaposition of the two active systems indicates that while Olkaria and Longonot may have substantial separate subsurface plumbing systems, they likely share common basaltic roots and a broader regional magmatic connection facilitated by crustal fluid migration along structural weaknesses related to active rifting.

CRediT authorship contribution statement

P.A. Wallace: Writing – review & editing, Writing – original draft, Visualization, Supervision, Project administration, Methodology, Investigation, Funding acquisition, Formal analysis, Data curation, Conceptualization. **V. Otieno:** Writing – review & editing, Resources, Project administration, Investigation. **P. Godec:** Writing – review & editing, Investigation, Formal analysis. **R.W. Njoroge:** Writing – review & editing, Investigation. **M.S. Tubula:** Writing – review & editing, Investigation. **L. Cappelli:** Writing – review & editing, Investigation, Funding acquisition. **P.M. Kamau:** Writing – review & editing, Investigation. **S. Nomade:** Writing – review & editing, Visualization, Resources, Methodology, Investigation, Formal analysis, Data curation. **N. O. Mariita:** Writing – review & editing, Project administration, Investigation, Conceptualization. **K. Fontijn:** Writing – review & editing, Supervision, Resources, Project administration, Investigation, Funding acquisition, Conceptualization.

Declaration of competing interest

The authors declare that they have no known competing financial interests or personal relationships that could have appeared to influence the work reported in this paper.

Acknowledgements

This study was funded by an F.R.S.-FNRS postdoctoral research fellowship awarded to PW, an F.R.S.-FNRS MIS grant ("VolKenya" - F.4515.20) awarded to KF, and an F.R.S.-FNRS Aspirant PhD studentship to LC. PW acknowledges support from LMUexcellent fund, funded by the Federal Ministry of Education and Research (BMBF) and the Free State of Bavaria under the Excellence Strategy of the Federal Government and the Länder. KF also acknowledges support from the Wiener-Anspach Foundation. We thank Jean-Luc Devidal (Université Clermont Auvergne, Laboratoire Magmas et Volcans) for his assistance during EPMA data collection, and Mathieu Boudin (KIK-IRPA, Institut Royal du Patrimoine Artistique) for handling the radiocarbon dating. We would like to thank Simon Kisotu and Robert Tanui from KenGen, NACOSTI and the Kenyan Wildlife Service (KWS) for relevant research permits, our drivers Sammy Nderitu and Edwin Muchemi, and all the local guides who helped and assisted us during the field campaigns. We wish to thank the editor, José Luis Macías, and two reviewers (Benjamin J. Andrews and an anonymous reviewer), for their detailed and constructive reviews.

Appendix A. Supplementary data

Supplementary data to this article can be found online at https://doi.org/10.1016/j.jvolgeores.2025.108275.

Data availability

Data will be made available on request.

References

Albino, F., Biggs, J., 2021. Magmatic processes in the east African rift system: Insights from a 2015–2020 sentinel-1 InSAR survey. Geochem. Geophys. Geosyst. 22. https://doi.org/10.1029/2020gc009488.

Albino, F., Biggs, J., Lazecký, M., Maghsoudi, Y., 2022. Routine processing and automatic detection of volcanic ground deformation using Sentinel-1 InSAR data: Insights from African volcanoes. Remote Sens. 14, 5703.

Alexander, K.B., Ussher, G., 2011. Geothermal resource assessment for Mt Longonot, Central Rift Valley, Kenya. In: Proceedings of the GRC Annual Meeting, San Diego, CA, USA, pp. 23–26.

Axelsson, G., Gudmundsdóttir, V., Arnaldsson, A., Ármannsson, H., Knútur Árnason, G., Einarsson, H., 2017. Revision of the Conceptual Model for the Olkaria Geothermal System, Kenya. In: Proceedings Stanford Geothermal Workshop, pp. 1–9.

Bailey, D.K., Macdonald, R., 1987. Dry Peralkaline Felsic Liquids and Carbon Dioxide Flux through the Kenya Rift Zone. Magmatic Processes: Physicochemical Principles.

Baker, B.H., Mitchell, J.G., 1976. Volcanic stratigraphy and geochronology of the Kedong–Olorgesailie area and the evolution of the South Kenya rift valley. J. Geol. Soc. Lond. 132, 467–484.

Bas, M.J.L.E., Maitre, R.W.L.E., Streckeisen, A., Zanettin, B., Subcommission, I.U.G.S., on the Systematics of Igneous Rocks, 1986. A Chemical Classification of Volcanic Rocks based on the Total Alkali-Silica Diagram. J. Petrol. 27, 745–750.

Biggs, J., Anthony, E.Y., Ebinger, C.J., 2009. Multiple inflation and deflation events at Kenyan volcanoes, East African Rift. Geology 37, 979–982.

Biggs, J., Bastow, I.D., Keir, D., Lewi, E., 2011. Pulses of deformation reveal frequently recurring shallow magmatic activity beneath the Main Ethiopian Rift. Geochem. Geophys. Geosyst. 12. https://doi.org/10.1029/2011gc003662.

Biggs, J., Ayele, A., Fischer, T.P., Fontijn, K., Hutchison, W., Kazimoto, E., Whaler, K., Wright, T.J., 2021. Volcanic activity and hazard in the East African Rift Zone. Nat. Commun. 12, 6881.

Black, S., Macdonald, R., Kelly, M.R., 1997. Crustal origin for peralkaline rhyolites from Kenya: evidence from U-series disequilibria and Th-isotopes. J. Petrol. 38, 277–297.

Blegen, N., Tryon, C.A., Faith, J.T., Peppe, D.J., Beverly, E.J., Li, B., Jacobs, Z., 2015. Distal tephras of the eastern Lake Victoria basin, equatorial East Africa: Correlations, chronology and a context for early modern humans. Quat. Sci. Rev. 122, 89–111.

Blegen, N., Brown, F.H., Jicha, B.R., Binetti, K.M., Faith, J.T., Ferraro, J.V., Gathogo, P. N., Richardson, J.L., Tryon, C.A., 2016. The Menengai Tuff: a 36 ka widespread tephra and its chronological relevance to late Pleistocene human evolution in East Africa. Quat. Sci. Rev. 152, 152–168.

Bonadonna, C., Houghton, B.F., 2005. Total grain-size distribution and volume of tephra-fall deposits. Bull. Volcanol. 67, 441–456.

Boudoire, G., Calabrese, S., Colacicco, A., Sordini, P., Habakaramo Macumu, P., Rafflin, V., Valade, S., Mweze, T., Kazadi Mwepu, J.-C., Safari Habari, F., Amani Kahamire, T., Mumbere Mutima, Y., Ngaruye, J.-C., Tuyishime, A., Tumaini Sadiki, A., Mavonga Tuluka, G., Mapendano Yalire, M., Kets, E.-D., Grassa, F., D'Alessandro, W., Caliro, S., Rufino, F., Tedesco, D., 2022. Scientific response to the 2021 eruption of Nyiragongo based on the implementation of a participatory monitoring system. Sci. Rep. 12, 7488.

Bronk Ramsey, C., 2009. Bayesian analysis of radiocarbon dates. Radiocarbon 51, 337–360.

Brown, F.H., Nash, B.P., Fernandez, D.P., Merrick, H.V., Thomas, R.J., 2013. Geochemical composition of source obsidians from Kenya. J. Archaeol. Sci. 40, 3233–3251.

Cappelli, L., Wallace, P.A., Randazzo, A., Kamau, P.M., Njoroge, R.W., Otieno, V., Tubula, M.S., Mariita, N.O., Mangi, P., Fontijn, K., 2023. Diffuse soil CO2 emissions at rift volcanoes: Structural controls and total budget of the Olkaria Volcanic complex (Kenya) case study. J. Volcanol. Geotherm. Res. 443, 107929.

Clarke, M.C.G., Woodhall, D.G., Allen, D., Darling, G., 1990. Geological, Volcanological and Hydrogeological Controls on the Occurrence of Geothermal Activity in the Area Surrounding Lake Naivasha, Kenya. Ministry of Energy. Kenya and British Geological Survey, Nairobi, p. 138.

Clarke, B., Tierz, P., Calder, E., Yirgu, G., 2020. Probabilistic volcanic hazard assessment for pyroclastic density currents from pumice cone eruptions at aluto volcano, Ethiopia. Front. Earth Sci. 8. https://doi.org/10.3389/feart.2020.00348.

Colby, D.J., Pyle, D.M., Fontijn, K., Mather, T.A., Melaku, A.A., Mengesha, M.A., Yirgu, G., 2022. Stratigraphy and eruptive history of Corbetti Caldera in the Main Ethiopian Rift. J. Volcanol. Geotherm. Res. 428, 107580.

Davies, G.R., Macdonald, R., 1987. Crustal influences in the petrogenesis of the Naivasha basalt - comendite complex: combined trace element and Sr-Nd-Pb isotope constraints. J. Petrol. 28, 1009–1031.

Di Genova, D., Romano, C., Hess, K.U., Vona, A., Poe, B.T., Giordano, D., Dingwell, D.B., Behrens, H., 2013. The rheology of peralkaline rhyolites from Pantelleria Island. J. Volcanol. Geotherm. Res. 249, 201–216.

Ebinger, C., 2005. Continental break-up: the East African perspective. Astron. Geophys. 46, 2.16-2.21.

Ebinger, C.J., Yemane, T., Harding, D.J., Tesfaye, S., Kelley, S., Rex, D.C., 2000. Rift deflection, migration, and propagation: Linkage of the Ethiopian and Eastern rifts, Africa. Geol. Soc. Am. Bull. 112, 163–176.

Ebinger, C.J., Keir, D., Bastow, I.D., Whaler, K., Hammond, J.O.S., Ayele, A., Miller, M.S., Tiberi, C., Hautot, S., 2017. Crustal structure of active deformation zones in Africa: Implications for global crustal processes. Tectonics 36, 3298–3332.

Fierstein, J., Hildreth, W., 1992. The plinian eruptions of 1912 at Novarupta, Katmai National Park, Alaska. Bull Volcanol 54, 646–684.

Fontijn, K., Ernst, G.G.J., Elburg, M.A., Williamson, D., Abdallah, E., Kwelwa, S., Mbede, E., Jacobs, P., 2010. Holocene explosive eruptions in the Rungwe Volcanic Province, Tanzania. J. Volcanol. Geotherm. Res. 196, 91–110.

Fontijn, K., McNamara, K., Zafu Tadesse, A., Pyle, D.M., Dessalegn, F., Hutchison, W., Mather, T.A., Yirgu, G., 2018. Contrasting styles of post-caldera volcanism along the Main Ethiopian Rift: Implications for contemporary volcanic hazards. J. Volcanol. Geotherm. Res. 356, 90–113.

Froggatt, P.C., 1983. Toward a comprehensive upper Quaternary tephra and ignimbrite stratigraphy in New Zealand using electron microprobe analysis of glass shards. Quat. Res. 19, 188–200.

Global Volcanism Program, 2023. Olkaria (222090) [WWW Document]. Volcanoes of the World (v. 5.1.5). Distributed by Smithsonian Institution, compiled by Venzke, E. URL. https://volcano.si.edu/volcano.cfm?vn=222090 (accessed 9.21.23).

Goitom, B., Oppenheimer, C., Hammond, J.O.S., Grandin, R., Barnie, T., Donovan, A., Ogubazghi, G., Yohannes, E., Kibrom, G., Kendall, J.-M., Carn, S.A., Fee, D., Sealing, C., Keir, D., Ayele, A., Blundy, J., Hamlyn, J., Wright, T., Berhe, S., 2015. First recorded eruption of Nabro volcano, Eritrea, 2011. Bull. Volcanol. 77, 85.

Halldórsson, S.A., Hilton, D.R., Scarsi, P., Abebe, T., Hopp, J., 2014. A common mantle plume source beneath the entire East African Rift System revealed by coupled helium-neon systematics. Geophys. Res. Lett. 41, 2304–2311.

Hass, H., Dalbey, T.S., 1991. Absolute radiocarbon chronology of the Aubrey Clovis site, Texas, based on soil humate stratigraphy. Radiocarbon 33, 204–205.

Heumann, A., Davies, G.R., 2002. U–Th Disequilibrium and Rb–Sr Age Constraints on the Magmatic Evolution of Peralkaline Rhyolites from Kenya. J. Petrol. 43, 557–577.

Hogg, A.G., Heaton, T.J., Hua, Q., Palmer, J.G., Turney, C.S.M., Southon, J., Bayliss, A., Blackwell, P.G., Boswijk, G., Bronk Ramsey, C., Pearson, C., Petchey, F., Reimer, P., Reimer, R., Wacker, L., 2020. SHCal20 Southern Hemisphere Calibration, 0–55,000 years cal BP. Radiocarbon 62, 759–778.

Hutchison, W., Pyle, D.M., Mather, T.A., Yirgu, G., Biggs, J., Cohen, B.E., Barfod, D.N., Lewi, E., 2016. The eruptive history and magmatic evolution of Aluto volcano: new insights into silicic peralkaline volcanism in the Ethiopian rift. J. Volcanol. Geotherm. Res. 328, 9–33.

Iddon, F., Edmonds, M., 2020. Volatile-Rich Magmas distributed through the Upper Crust in the Main Ethiopian Rift. Geochem. Geophys. Geosyst. 21. https://doi.org/10.1029/2019GC008904.

Jochum, K.P., Stoll, B., Herwig, K., Willbold, M., Hofmann, A.W., Amini, M., Aarburg, S., Abouchami, W., Hellebrand, E., Mocek, B., Raczek, I., Stracke, A., Alard, O., Bouman, C., Becker, S., Dücking, M., Brätz, H., Klemd, R., de Bruin, D., Canil, D., Cornell, D., de Hoog, C.-J., Dalpé, C., Danyushevsky, L., Eisenhauer, A., Gao, Y., Snow, J.E., Groschopf, N., Günther, D., Latkoczy, C., Guillong, M., Hauri, E.H., Höfer, H.E., Lahaye, Y., Horz, K., Jacob, D.E., Kasemann, S.A., Kent, A.J.R., Ludwig, T., Zack, T., Mason, P.R.D., Meixner, A., Rosner, M., Misawa, K., Nash, B.P., Pfänder, J., Premo, W.R., Sun, W.D., Tiepolo, M., Vannucci, R., Vennemann, T., Wayne, D., Woodhead, J.D., 2006. MPI-DING reference glasses for in situ microanalysis: New reference values for element concentrations and isotope ratios. Geochem. Geophys. Geosyst. 7. https://doi.org/10.1029/2005gc001060.

Keranen, K., Klemperer, S.L., Gloaguen, R., EAGLE Working Group, 2004. Three-dimensional seismic imaging of a protoridge axis in the Main Ethiopian rift. Geology 32, 949.

Komorowski, J.-C., Karume, K., 2015. Nyiragongo (Democratic Republic of Congo), January 2002: A major eruption in the midst of a complex humanitarian emergency. In: Loughlin, S.C., Sparks, S., Brown, S.K., Jenkins, S.F., Vye-Brown, C. (Eds.), Global Volcanic Hazards and Risk. Cambridge University Press, Cambridge, pp. 273–280.
Koppers, A.A.P., 2002. ArArCALC—software for 40Ar/39Ar age calculations. Comput. Geosci. 28, 605–619.
Lagat, J., 2003. Geology and the geothermal systems of the southern segment of the Kenya Rift. In: International Geothermal Conference. Reykjavik, Iceland, pp. 40–47.
Lane, C.S., Martin-Jones, C.M., Johnson, T.C., 2018. A cryptotephra record from the Lake Victoria sediment core record of Holocene palaeoenvironmental change. Holocene 28, 1909–1917.
Leat, P.T., 1984. Geological evolution of the trachytic caldera volcano Menengai, Kenya Rift Valley. J. Geol. Soc. Lond. 141, 1057–1069.
Lee, J.-Y., Marti, K., Severinghaus, J.P., Kawamura, K., Yoo, H.-S., Lee, J.B., Kim, J.S., 2006. A redetermination of the isotopic abundances of atmospheric Ar. Geochim. Cosmochim. Acta 70, 4507–4512.
Lowe, D.J., 2011. Tephrochronology and its application: a review. Quat. Geochronol. 6, 107–153.
Ludwig, K.R., 2003. Isoplot 3.00: A Geochronological Toolkit for Microsoft Excel. Berkeley Geochronology Center.
Luhr, J.F., Carmichael, I.S.E., 1980. The Colima Volcanic complex, Mexico. Contributions to mineralogy and petrology. Beitrage zur Mineral. Petrol. 71, 343–372.
MacDonald, R., 1974. Nomenclature and petrochemistry of the peralkaline oversaturated extrusive rocks. Bull. Volcanol. 38, 498–516.
Macdonald, R., 2002. Magmatism of the Kenya Rift Valley: a review. Trans. Royal Soci. Edinburgh Earth Sciences 93, 239–253.
Macdonald, R., Scaillet, B., 2006. The Central Kenya peralkaline province: Insights into the evolution of peralkaline salic magmas. Lithos 91, 59–73.
Macdonald, R., Davies, G.R., Bliss, C.M., Leat, P.T., Bailey, D.K., Smith, R.L., 1987. Geochemistry of high-silica peralkaline rhyolites, Naivasha, Kenya rift valley. J. Petrol. 28, 979–1008.
Macdonald, R., Williams, L.A.J., Gass, I.G., 1994. Tectonomagmatic evolution of the Kenya rift valley: some geological perspectives. J. Geol. Soc. Lond. 151, 879–888.
Macdonald, R., Rogers, N.W., Fitton, J.G., Black, S., Smith, M., 2001. Plume–Lithosphere Interactions in the Generation of the Basalts of the Kenya Rift, East Africa. J. Petrol. 42, 877–900.
Macdonald, R., Belkin, H.E., Fitton, J.G., Rogers, N.W., Nejbert, K., Tindle, A.G., Marshall, A.S., 2008. The roles of fractional crystallization, magma mixing, crystal mush remobilization and volatile-melt interactions in the genesis of a young basalt-peralkaline rhyolite suite, the greater Olkaria volcanic complex, Kenya Rift valley. J. Petrol. 49, 1515–1547.
Macdonald, R., White, J.C., Belkin, H.E., 2022. Peralkaline silicic extrusive rocks: magma genesis, evolution, plumbing systems and eruption. Compt. Rendus Geosci. 353, 7–59.
Marshall, A.S., Hinton, R.W., Macdonald, R., 1998. Phenocrystic fluorite in peralkaline rhyolites, Olkaria, Kenya Rift Valley. Mineral. Mag. 62, 477–486.
Marshall, A.S., Macdonald, R., Rogers, N.W., Fitton, J.G., Tindle, A.G., Nejbert, K., Hinton, R.W., 2009. Fractionation of peralkaline silicic magmas: the greater olkaria volcanic complex, Kenya Rift Valley. J. Petrol. 50, 323–359.
Martin, C.W., Johnson, W.C., 1995. Variation in radiocarbon ages of soil organic matter fractions from late Quaternary buried soils. Quat. Res. 43, 232–237.
Martin-Jones, C.M., Lane, C.S., Pearce, N.J.G., Smith, V.C., Lamb, H.F., Schaebitz, F., Viehberg, F., Brown, M.C., Frank, U., Asrat, A., 2017. Recurrent explosive eruptions from a high-risk Main Ethiopian Rift volcano throughout the Holocene. Geology 45, 1127–1130.
McConnell, R.B., 1972. Geological Development of the Rift System of Eastern Africa. GSA Bull. 83, 2549–2572.
McNamara, K., Cashman, K.V., Rust, A.C., Fontijn, K., Chalié, F., Tomlinson, E.L., Yirgu, G., 2018. Using Lake Sediment Cores to Improve Records of Volcanism at Aluto Volcano in the Main Ethiopian Rift. Geochem. Geophys. Geosyst. 19, 3164–3188.
Mibei, G., Harðarson, B.S., Franzson, H., Bali, E., Geirsson, H., Guðfinnsson, G.H., 2021. Eruptive history and volcano-tectonic evolution of Paka volcanic complex in the northern Kenya rift: Insights into the geothermal heat source. J. African Earth Sci. (Oxford, England: 1994) 173, 103951.
Mohr, P., Mitchell, J.G., Raynolds, R.G.H., 1980. Quaternary volcanism and faulting at O'A caldera, central ethiopian rift. Bull. Volcanol. 43, 173–189.
Muirhead, J.D., Kattenhorn, S.A., 2018. Activation of preexisting transverse structures in an evolving magmatic rift in East Africa. J. Struct. Geol. 106, 1–18.
Muirhead, J.D., Kattenhorn, S.A., Lee, H., Mana, S., Turrin, B.D., Fischer, T.P., Kianji, G., Dindi, E., Stamps, D.S., 2016. Evolution of upper crustal faulting assisted by magmatic volatile release during early-stage continental rift development in the East African Rift. Geosphere 12, 1670–1700.
Naylor, W.I., 1972. The Geology of the Eburru and Olkaria Geothermal Prospects. WI Naylor.
Niespolo, E.M., Rutte, D., Deino, A.L., Renne, P.R., 2017. Intercalibration and age of the Alder Creek sanidine 40Ar/39Ar standard. Quat. Geochronol. 39, 205–213.
Omenda, P.A., 1998. The geology and structural controls of the Olkaria geothermal system, Kenya. Geothermics 27, 55–74.
Omenda, P.A., 2010. Geothermal Exploration in Kenya. "Short Course VI on Exploration for Geothermal Resources", Organized by UNU-GTP, GDC and KenGen, Lake Naivasha, Kenya.
Omollo, P., Nishijima, J., 2023. Analysis and Interpretation of the gravity data to delineate subsurface structural geometry of the Olkaria geothermal reservoir, Kenya. Geothermics 110, 102663.
Omollo, P., Nishijima, J., Fujimitsu, Y., Sawayama, K., 2022. Resistivity structural imaging of the Olkaria Domes geothermal field in Kenya using 2D and 3D MT Data inversion. Geothermics 103, 102414.
Orlova, L.A., Panychev, V.A., 1993. The reliability of radiocarbon dating buried soils. Radiocarbon 35, 369–377.
Otieno, V.O., 2016. Borehole geology and sub-surface petrochemistry of the Domes area, Olkaria geothermal field, Kenya. In: In Relation to Well OW-922. University of Iceland.
Pyle, D.M., 1989. The thickness, volume and grainsize of tephra fall deposits. Bull. Volcanol. 51, 1–15.
Pyle, D.M., 2015. Chapter 13 - Sizes of Volcanic Eruptions. In: Sigurdsson, H. (Ed.), The Encyclopedia of Volcanoes, Second edition. Academic Press, Amsterdam, pp. 257–264.
Ren, M., Omenda, P.A., Anthony, E.Y., White, J.C., Macdonald, R., Bailey, D.K., 2006. Application of the QUILF thermobarometer to the peralkaline trachytes and pantellerites of the Eburru volcanic complex, East African Rift, Kenya. Lithos 91, 109–124.
Renne, P.R., Balco, G., Ludwig, K.R., Mundil, R., Min, K., 2011. Response to the comment by W.H. Schwarz et al. on "Joint determination of 40K decay constants and 40Ar*/40K for the fish Canyon sanidine standard, and improved accuracy for 40Ar/39Ar geochronology" by P.R. Renne et al. (2010). Geochim. Cosmochim. Acta 75, 5097–5100.
Robertson, E., Biggs, J., Edmonds, M., Clor, L., Fischer, T.P., Vye-Brown, C., Kianji, G., Koros, W., Kandie, R., 2016. Diffuse degassing at Longonot volcano, Kenya: Implications for CO2 flux in continental rifts. J. Volcanol. Geotherm. Res. 327, 208–222.
Rogers, N.W., Evans, P.J., Blake, S., Scott, S.C., Hawkesworth, C.J., 2004. Rates and timescales of fractional crystallization from 238U-230Th-226Ra disequilibria in trachyte lavas from Longonot volcano, Kenya. J. Petrol. 45, 1747–1776.
Rogers, N.W., Thomas, L.E., Macdonald, R., Hawkesworth, C.J., Mokadem, F., 2006. 238U–230Th disequilibrium in recent basalts and dynamic melting beneath the Kenya rift. Chem. Geol. 234, 148–168.
Rooney, T.O., 2020. The Cenozoic magmatism of East Africa: Part V – Magma sources and processes in the East African Rift. Lithos 360–361, 105296.
Scott, S.C., 1980. The geology of Longonot volcano, Central Kenya: a question of volumes. Philos. Trans. R. Soc. Lond. 296, 437–465.
Scott, S.C., Bailey, D.K., 1984. Coeruption of contrasting magmas and temporal variations in magma chemistry at Longonot volcano, Central Kenya. Bull. Volcanol. 47, 849–873.
Scott, S.C., Skilling, I.P., 1999. The role of tephrachronology in recognizing synchronous caldera-forming events at the Quaternary volcanoes Longonot and Suswa, South Kenya Rift. Geol. Soc. Spec. Publ. 161, 47–67.
Shi, Y., Rop, E., Wang, Z., Jiang, G., Wang, S., Hu, S., 2021. Characteristics and formation mechanism of the Olkaria geothermal system, Kenya revealed by well temperature data. Geothermics 97, 102243.
Simiyu, S., 2008. Status of geothermal exploration in Kenya and future plans for its development. In: Proceedings world Geothermal Congress.
Simiyu, S.M., Keller, G.R., 2000. Seismic monitoring of the Olkaria Geothermal area, Kenya Rift valley. J. Volcanol. Geotherm. Res. 95, 197–208.
Smith, M., 1994. Stratigraphic and structural constraints on mechanisms of active rifting in the Gregory Rift, Kenya. Tectonophysics 236, 3–22.
Smith, M., Mosley, P., 1993. Crustal heterogeneity and basement influence on the development of the Kenya Rift, East Africa. Tectonics 12, 591–606.
Sparks, R.S., Aspinall, W.P., Crosweller, H.S., Hincks, T.K., 2011. In: Rougier, J., Sparks, R.S.J., Hill, L. (Eds.), Risk and Uncertainty Assessment of Volcanic Hazards. Risk and Uncertainty Assessment for Natural Hazards, pp. 364–397.
Tadesse, A.Z., Fontijn, K., Melaku, A.A., Gebru, E.F., Smith, V.C., Tomlinson, E., Barfod, D., Gopon, P., Bégué, F., Caricchi, L., Laha, P., Terryn, H., Gudbrandsson, S., Yirgu, G., Ayalew, D., 2022. Eruption frequency and magnitude in a geothermally active continental rift: the Bora-Baricha-Tullu Moye volcanic complex, Main Ethiopian Rift. J. Volcanol. Geotherm. Res. 423, 107471.
Tazieff, H., 1977. An exceptional eruption: Mt. Niragongo, Jan. 10th, 1977. Bull. Volcanol. 40, 189–200.
Theys, N., Campion, R., Clarisse, L., Brenot, H., Gent, J. van, Dils, B., Corradini, S., Merucci, L., Coheur, P.-F., Van Roozendael, M., Hurtmans, D., Clerbaux, C., Tait, S., Ferrucci, F., 2013. Volcanic SO_2 fluxes derived from satellite data: a survey using OMI, GOME-2, IASI and MODIS. Atmos. Chem. Phys. 13, 5945–5968.
Tierz, P., Clarke, B., Calder, E.S., Dessalegn, F., Lewi, E., Yirgu, G., Fontijn, K., Crummy, J.M., Bekele, Y., Loughlin, S.C., 2020. Event trees and epistemic uncertainty in long-term volcanic hazard assessment of rift volcanoes: the example of aluto (Central Ethiopia). Geochem. Geophys. Geosyst. 21. https://doi.org/10.1029/2020gc009219.
Tornqvist, T.E., De Jong, A., Osterbaan, W.A., Van der Borg, K., 1991. New perspectives for radiocarbon dating organic deposits by accelerator mass spectrometry. Radiocarbon 33, 251–252.
Wadge, G., Biggs, J., Lloyd, R., Kendall, J.M., 2016. Historical volcanism and the state of stress in the east African rift system. Front. Earth Sci. China 4. https://doi.org/10.3389/feart.2016.00086.
Wamalwa, R.N., Nyamai, C.M., Ambusso, W.J., Mulwa, J., Waswa, A.K., 2016. Structural controls on the geochemistry and output of the wells in the olkaria geothermal field of the Kenyan rift valley. Int. J. Geosci. 07, 1299–1309.

Wang, Y., Amundson, R., Trumbore, S., 1996. Radiocarbon dating of soil organic matter. Quat. Res. 45, 282–288.
Wiart, P., Oppenheimer, C., 2000. Largest known historical eruption in Africa: Dubbi volcano, Eritrea, 1861. Geology 28, 291–294.
Wilding, M.C., Macdonald, R., Davies, J.E., Fallick, A.E., 1993. Volatile characteristics of peralkaline rhyolites from Kenya: an ion microprobe, infrared spectroscopic and hydrogen isotope study. Contributions to mineralogy and petrology. Beitrage zur Mineral. Petrol. 114, 264–275.